Indoor channel modeling and high data-rate Transmission for visible-light communication systems

Shihe Long

ÉCOLE CENTRALE MARSEILLE

N° attribué par la bibliothèque
XXXX

TITRE:

MODÉLISTATION DU CANAL INTRA-BÂTIMENT ET TRANSMISSION HAUT-DÉBIT POUR LES COMMUNICATIONS OPTIQUES DANS LE SPECTRE VISIBLE

THÈSE
pour obtenir le grade de DOCTEUR

École Doctorale : Physique et Sciences de la Matière
Mention : Optique, Photonique et Traitement des Images

Effectuée à l'INSTITUT FRESNEL
Présentée et soutenue publiquement par:

Shihe LONG
le 21 Septembre 2016

Directeur de thèse: M. Salah BOURENNANE
Co-Directeur de thèse: M. Mohammad-Ali KHALIGHI

JURY :

Rapporteurs:	Mme Anne JULIEN-VERGONJANNE	ENSIL, Limoges
	M. Eric Pierre SIMON	Université de Lille 1
Examinateurs:	M. Zabih GHASSEMLOOY	Université Northumbria, Royaume-Uni
	M. Pierre LEON	IFREMER
Directeurs de thèse:	M. Salah BOURENNANE	École Centrale Marseille
	M. Mohammad-Ali KHALIGHI	École Centrale Marseille

ANNEE : 2016

ÉCOLE CENTRALE MARSEILLE

N° assigned by library
XXXX

TITLE:

INDOOR CHANNEL MODELING AND HIGH DATA-RATE TRANSMISSION FOR VISIBLE-LIGHT COMMUNICATION SYSTEMS

THESIS
to obtain the degree of Doctor of Philosophy

issued by ÉCOLE CENTRALE MARSEILLE

Doctoral school : Physics and Material Sciences
Discipline : Optics, Photonics and Image Processing

Carried out at FRESNEL INSTITUTE
Presented and defended publicly by:

Shihe LONG
on September 21st 2016

Thesis advisor: Mr. Salah BOURENNANE
Thesis co-advisor: Mr. Mohammad-Ali KHALIGHI

COMMITTEE :

Reviewers:	Mrs. Anne JULIEN-VERGONJANNE	ENSIL, Limoges
	Mr. Eric Pierre SIMON	University of Lille 1
Examiners:	Mr. Zabih GHASSEMLOOY	Northumbria University, United Kingdom
	Mr. Pierre LEON	IFREMER
Thesis advisors:	Mr. Salah BOURENNANE	École Centrale Marseille
	Mr. Mohammad-Ali KHALIGHI	École Centrale Marseille

YEAR : 2016

Table of contents

List of Notations

$A_r(\cdot)$	effective receiving area
ϕ	emitting angle
φ	incident angle
$\phi_{1/2}$	semi-angle
B	signal bandwidth
E_b	average energy per bit
f_c	cut-off frequency
$\mathcal{I}m\{*\}$	imaginary part of a complex number
κ	clipping factor in dB
$\odot$	circular convolution
*	complex conjugation
$\otimes$	convolution
$\mathcal{R}e\{*\}$	real part of a complex number
I	electrical current
β_{DC}	DC-bias current
τ	mean excess delay
μ	RMS delay spread
e	electron charge
η	quantum efficiency
$E[\cdot]$	statistical expectation
$\exp(\cdot)$	exponential function
ν	frequency of the light
c	light propagation speed
N_0	noise power spectral density
$\hbar$	Planck constant
P_{opt}	optical power

$Q(\cdot)$	Q function
$T(\cdot)$	radiation pattern
G	optical concentrator gain
R	responsitivity of the photodiode
T_b	bit duration
T_s	symbol duration
Vpp	peak-to-peak voltage

List of Acronyms

A/D	analog-to-digital converter
AC	alternative-current
ACO	asymmetrically clipped optical
ADSL	asymmetric digital subscriber line
AWG	arbitrary waveform generator
AWGN	additive white Gaussian noise
BER	bit error rate
BF	Bessel filter
CAP	carrier-less amplitude and phase
CCDF	complementary comcumulative distribution function
CLT	central limit theorem
CP	cyclic prefix
D/A	digital-to-analog converter
DC	direct-current
DCO	direct-current-biased optical
DFT	discrete Fourier transform
DMT	discrete multitone
FDE	frequency domain equalization
FDM	frequency-division multiplexing
FFT	fast Fourier transform
FIR	finite impulse response
FOV	field-of-view
FR	frequency response
HDSL	High-bit-rate digital subscriber line
i.i.d.	independent and identically distributed
I/Q	inphase/quadrature

ICI	inter-carrier interference
IDFT	inverse discrete Fourier transform
IFFT	inverse fast Fourier transform
IM/DD	intensity modulation and direct detection
IR	impluse response
ISI	intersymbol interference
LED	light-emitting diode
LOS	line-of-sight
LTE	Long-Term Evolution
LTI	linear time-invariant
MCM	multi-carrier modulation
MF	matched filter
MIMO	multiple-input multiple-output
NCR	noise-to-carrier ratio
NRZ	non-return-to-zero
OCRG	optical communications research group
OFDM	orthogonal frequency-division multiplexing
OOK	on-off keying
OWC	optical wireless communications
P/S	parallel/serial
PAM	pulse amplitude modulation
PAPR	peak-to-average power ratio
PD	photo-detector
PIN	P-i-N
PPM	pulse position modulation
PSD	power spectral density
PWM	pulse width modulation
QAM	quadrature amplitude modulation
RCF	raised-cosine filter
RF	radio frequency
RMS	root mean square
RRCF	root-raised-cosine filter
RV	random variable
RZ	return-to-zero
S/P	serial/parallel
SC	single-carrier

SC-FDE	single-carrer frequency domain equalization
SCM	single-carrier modulation
SER	symbol error rate
SIR	signal-to-ISI ratio
SNR	signal-to-noise ratio
SRRC	squared-root-raised-cosine filter
TIA	transimpedance amplifier
TOV	turn-on voltage
VLC	visible-light communications
VOOK	variable OOK
VPPM	variable PPM
WDM	wavelength-division multiplexing
ZF	zero-forcing

CHAPTER 1

General Introduction

1.1 Visible-light communication, overview

1.1.1 Research background

In recent years, world has witnessed a dramatic mobile data traffic growth due to emerging services such as video telephony, real-time video streaming, online gaming and cloud computing. According to Cisco's Global Mobile Data Traffic Forecast, the global mobile data traffic has grown 4000-fold over the past 10 years and this trend will continue to

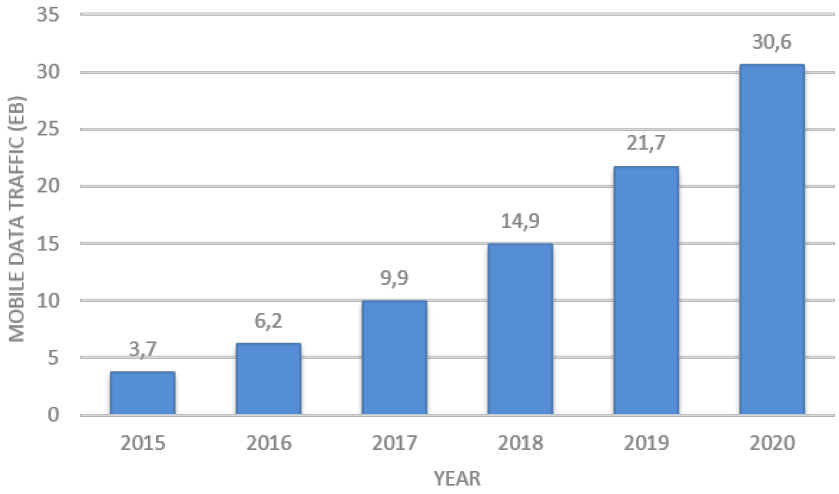

Figure 1.1 — Cisco forecast of mobile data traffic per month by 2020 (Source: Cisco VNI Mobile, 2015)

persist and will reach a record of 30.6 exabytes per month by 2020 as shown in Figure 1.1. This demand for mobility and high data-rate transmission has strengthened the

need for further innovation and development in new emerging wireless technologies. The current radio frequency (RF) transmission standards appear incapable to address all the challenges and requirements. Indeed, the world's mobile offload exceeded the RF-based cellular traffic for the first time in 2015 and about half of the mobile data traffic was offloaded onto the fixed network through Wi-Fi [1]. In fact, the major bottleneck arises from the available RF spectrum. Nearly all of the RF spectrum in the range of 3 KHz to 300 GHz has already been allocated to various wireless standards and little is left to be exploited. Moreover, the overall system performance can be severely degraded due to the interference between neighbour RF systems operating in the same frequency band. Currently, the potential solutions under investigation for addressing this "future of data traffic hunger" problem can be categorized into two approaches:

- Increasing the spectral efficiency of the current RF systems by means of multiple-input multiple-output (MIMO) techniques, carrier-aggregation, cooperative communications, etc.
- Exploiting the unused frequency bands above 300 GHz.

Following the path of the second approach, optical wireless communications (OWC), which utilize the optical spectrum from 300 GHz to 790 THz, are a promising solution for future high data-rate transmission. By harnessing this vast unlicensed spectrum, OWC can potentially provide very high data-rate point-to-point communication and have been shown to be a powerful complementary technology to RF transmission standards.

Visible-light communications (VLC) are one of the OWC variants by which the information is modulated on the visible light usually produced by a light-emitting diode (LED). As shown in Figure 1.2, the wavelength of the visible light spectrum ranges from 380 nm to 750 nm summing up to a whole bandwidth of about 300 THz, which is orders of magnitude higher than the typical bandwidth of most RF systems. As such, VLC links can deliver much higher data-rate transmission in indoor environments than the traditional RF-powered Wi-Fi technology with a lower power consumption. VLC have been an attractive subject of research in the recent years and will play an important role in the future high data-rate home access networks.

1.1.2 Brief history

The use of visible light for communication dates back to two thousand years ago by many different cultures, *e.g.*, the fire beacons on the great wall of ancient China for

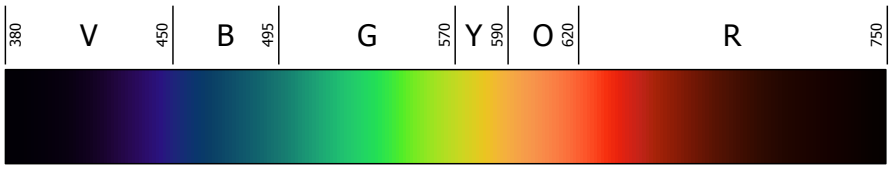

Figure 1.2 — The visible spectrum (Source: http://commons.wikimedia.org/wiki/File:Spectrum4websiteEval.png, license:public domain)

transmitting military intelligence and the lighthouses for navigating ships in harbors of ancient Greece [2]. However, the first sophisticated communication system employing visible light is the "Photophone" invented by a Scottish scientist Alexander Graham Bell in 1880. This system was based on the voice-caused vibrations on a mirror at the transmitter and was capable to achieve a transmission length of 213 meters [3]. In 1962, Biard and Pittman patented the first p-n junction infrared LED and lately the first visible-spectrum (red) LED was developed by Nich Holonyak at General Electric. Since then, numerous advances have been made in solid-state-lighting area, including the invention of high-brightness blue LED by Shuji Nakamura. In 2000s, people realized that the LED can also be modulated to provide a data connection in addition to its original illumination purpose [4]. Since then, the idea of VLC has been spread out and they have become a dynamic subject of research and development. The Visible Light Communication Consortium (VLCC) is founded in Japon in 2003 to publicize and guide the standardization of VLC [5]. The OMEGA project under the Europe Union Framework Program 7 (FP7), started in 2008, demonstrated a VLC-based high data-rate home access network [6]. The IEEE 802.15.7 standard [7] has been approved in June 2011 to define the physical layer and medium access control (MAC) for VLC systems. Numerous prototypes have also been realized, such as those in Frauhofer Institute [8], Berlin, OCRG Laboratory, Newcastle, and Scuola Superiore Sant'anna with the data-rates exceeding 1 Gbps. Also, a few commercial products have been recently released to market, such as those of PureLiFi [9].

1.1.3 Pros and cons and possible applications

VLC have numerous advantages over the traditional RF technology. Firstly, by this technology, one can potentially use a very large worldwide unregulated bandwidth up to 300 THz [10]. Secondly, the VLC signal can not penetrate through walls, thus, VLC communication cells in adjacent rooms does not interfere with each other, which allows a larger spatial reuse factor than RF cellular technology [11]. In addition, this charac-

teristics of VLC prevents eavesdropping and brings higher transmission security. Also, the visible light produced by the LED is harmless for human health, in contrast to the potential health concerns on RF electromagnetic radiations. This is important in restrictive areas where RF is not desired such as in hospitals, air planes and chemical plants. Last but not least, by exploiting the existing LED-based illumination facilities, VLC are also more energy-efficient than RF in terms of power consumption per users. Due to these advantages, VLC can be used in various applications such as indoor high data-rate connection, usually referred to as Light-Fidelity (Li-Fi), indoor positioning, car-to-car communications, etc.

Despite these advantages, there are several challenges in the deployment of VLC links. Firstly, the performance of VLC links can be severely impacted by the interference from background light sources, *e.g.*, sunlight. Also, data transmission may be interrupted in case of blocked line-of-sight (LOS) path between the transmitter and the receiver. In addition, the LED has a limited modulation bandwidth and exhibits non-linear characteristics. Lastly, establishing the uplink and addressing the user mobility and light dimming are among the important challenges that need to be answered in the future [12]. Nevertheless, VLC can be an efficient complementary technology to RF in the establishment of future high data-rate indoor wireless networks.

1.2 Thesis objective

As described above, the VLC technology today is far to be mature and faces several challenges. In particular, in terms of achieving high data rates in indoor applications, there are two main challenges arising from the indoor VLC channel and the LED transmitter. Indeed, the indoor VLC channel can be frequency selective due to multipath propagations, which consists of the LOS and the reflected or diffuse light. The degree of frequency selectivity highly depends on the room geometry, surface reflectance and transceiver arrangements. Secondly, the commercially available white LEDs have a raw modulation bandwidth limited to a few MHz only and exhibit non-linear characteristics within their operation range. High spectral efficiency schemes such as optical orthogonal frequency-division multiplexing (OFDM) have become very popular in the indoor VLC context to achieve high data-rate transmissions. However, the drawbacks of optical OFDM schemes is their high peak-to-average power ratio (PAPR), which could result in severe non-linear distortion that is difficult to compensate. An alternative approach is to use single-carrier (SC) modulations combined with frequency domain equalization

(FDE), which has the same advantage as optical OFDM schemes in terms of robustness against channel delay dispersion and simple equalization while benefiting from a lower PAPR.

The objective of this thesis is to investigate, characterize and model the two main limiting factors in VLC systems and to propose efficient transmission solutions that can alleviate their effect. More specifically, the main questions motivating our research are summarized below:

1. Concerning the indoor VLC channel, how to characterize and quantify its effect if we aiming high data-rate transmission? (addressed in Chapter 3)
2. Regarding their high PAPR, what are the benefits of using optical OFDM schemes to overcome the limited modulation bandwidth of the LED? (addressed in Chapter 4)
3. Besides the optical OFDM schemes, are there any alternative solutions to address the LED limited modulation bandwidth problem? Considering the use of SC, in particular, carrier-less amplitude and phase (CAP) modulation, combined with FDE, are there any advantages over optical OFDM schemes?(addressed in Chapter 5)
4. How to model the non-linear characteristics of the LED and what is its impact on the system performance? (addressed in Chapter 6)

1.3 Thesis structure and contributions

1.3.1 Thesis outline

This dissertation is organized in seven chapters as described in the following:

Chapter 2 is devoted to the description of a general VLC system. We start by describing the possible LED transmitters, including white, RGB and organic LEDs, that are commonly used in VLC systems. The drawbacks of those components regarding the limited modulation bandwidth and the non-linear characteristics are also addressed. Then, we give details of the optical receivers. and also discuss the characteristics of the indoor VLC channel. Finally, we review the possible signal modulations in VLC systems and explain potential solutions to address the dimming control issue. In a nutshell, the main purpose of this chapter is to give a general overview of VLC system.

Chapter 3 focuses on modeling the indoor VLC channel. We start by specifying the main assumptions concerning the source and the receiver. Then, we present details of the

method that we used to simulate the impluse response (IR) of the indoor VLC channel. Next, we move to the characterization of the indoor VLC channel by different metrics, including the classical frequency response (FR) and root mean square (RMS) delay spread, and also introduce the more appropriate metric of signal-to-ISI ratio (SIR) for quantifying the channel frequency selectivity. Lastly, we present the simulation results of the channel IR for different indoor scenarios and discuss the usefulness of the three channel metrics mentioned above. Based on these results, we specify the main assumptions on the indoor VLC channel that we make for later use in the following chapters.

Chapter 4 investigates the suitability of optical OFDM schemes for VLC to achieve high data-rate transmission. We first explain the general principles of OFDM by giving details on discrete Fourier transform (DFT), cyclic prefix (CP) insertion and also adaptive bit-power loading. Next, we present three optical OFDM schemes that are commonly used in VLC systems: direct-current-biased optical (DCO)-OFDM, asymmetrically clipped optical (ACO)-OFDM and pulse amplitude modulation (PAM)-discrete multitone (DMT). The PAPR issues of optical OFDM-based schemes together with the clipping noise are also addressed. Lastly, we present a set of simulation results to study their performance by taking into account the frequency response of the LED and the clipping noise.

Chapter 5 studies the benefits of using FDE in VLC systems. In particular, we propose to employ the CAP modulation together with FDE as an alternative to optical OFDM. We first present the principles of CAP modulation and explain the condition of zero interference. Then, we explain how to cope CAP with FDE and how to perform matched filtering and FDE at once in the frequency domain at the receiver. Next, we discuss the pros and cons of this scheme compared to optical OFDM-based schemes considered in the previous chapter. Lastly, we investigate the system performance of CAP-FDE through some numerical results.

Chapter 6 is dedicated to the investigation and modeling of the non-linear characteristics of the LED. In particular, we focus on how to model the non-linear transfer function of the LED, as it is crucial for designing appropriate signal processing techniques, such as modulation and equalization. Three models with different accuracy and complexity are reviewed and compared. The performance of the optical OFDM and CAP-FDE schemes are then compared to investigate the impact of non-linearity on the system performance.

Chapter 7 presents some experimental works that we carried on in the optical communications research group (OCRG) laboratory at Newcastle, UK, thanks to the support from IC1101 COST Action. We validate our assumptions that we made in this thesis on

the characteristic of the LED through measurements. Then, we present the results for the cases of DCO-OFDM and CAP-FDE transmission for a typical VLC link.

Chapter 8 concludes the thesis and gives some perspectives for future work.

1.3.2 Author's contributions

The main contributions of this thesis are briefly mentioned in the following:

- Simulated the indoor VLC channel and evaluated the usefulness of different channel characterization metrics. Demonstrated that the frequency selectivity of indoor VLC channel mainly arises from the multiple LOS instead of the diffuse response. Showed that the indoor VLC channel is not the main limiting factor to achieve high data rates except the case of purely diffused channel.

- Investigated the suitability of using optical OFDM schemes to overcome the limited modulation bandwidth of the LEDs in VLC systems.

- Proposed using FDE-based schemes, in particular, CAP-FDE, as an alternative to optical OFDM for indoor VLC systems. The proposed CAP-FDE has the advantages of high spectral efficiency as well as a lower PAPR, compared with optical OFDM-based schemes.

- Studied the non-linear characteristics of the LED and its mathematical modeling. Investigated the potential performance degradation for optical OFDM and FDE-based schemes due to this non-linearity.

- Experimentally investigated the BER performance of DCO-OFDM and CAP-FDE for a typical VLC link and demonstrated the merits of using the latter signaling scheme.

1.3.3 Author's publications

Journal papers

1. S. Long, M. A. Khalighi, M. Wolf, S. Bourennane, and Z. Ghassemlooy, "Investigating channel frequency selectivity in indoor visible-light communication systems," *IET Optoelectronics*, vol. 10, no. 3, pp. 80-88, May, 2016.

2. M. A. Khalighi, S. Long, S. Bourennane, and Z. Ghassemlooy, "Alternative Transmission Schemes to Optical-OFDM for Indoor High Data-Rate Visible Light Communications," *IEEE Communications Magazine*, submitted, May 2016.

Conference papers

1. S. Long, M. A. Khalighi, M. Wolf, S. Bourennane, and Z. Ghassemlooy, "Channel Characterization for Indoor Visible Light Communications," *International Workshop on Optical Wireless communications (IWOW)* , Madeira, Portugal, pp. 75-79, Sept. 2014.

2. S. Long, M. A. Khalighi, M. Wolf, S. Bourennane, and Z. Ghassemlooy, "Performance of Carrier-less Amplitude and Phase Modulation With Frequency Domain Equalization for Indoor Visible Light Communications," *International Workshop on Optical Wireless Communications (IWOW)*, Istanbul, Turkey, pp. 15-20, Sept. 2015.

3. K. Werfli, P. A. Haigh, Z. Ghassemlooy, P. Chvojka, S. Zvanovec, S. Rajbhandari and S. Long, " Multi-band carrier-less amplitude and phase modulation with decision feedback equalization for bandlimited VLC systems," *International Workshop on Optical Wireless Communications (IWOW)*, Istanbul, Turkey, pp. 6-10, Sept. 2015.

4. M. Wolf, S. A. Cheema, M. A. Khalighi and S. Long, "Transmission Schemes for Visible Light Communications in Multipath environments," *International Conference on Transparent Optical Networks (ICTON)*, Budapest, Hungary, pp. 1-7, July. 2015.

CHAPTER 2

Fundamentals of VLC systems

2.1 Introduction

A typical VLC system consists of a transmitter, a propagation channel and a receiver, as shown in Figure 2.1. At the transmitter, the information bits are firstly modulated and converted to an electrical signal by passing through a digital-to-analog converter (D/A). Then, with the help of a driver circuit, this latter is fed into an LED to modulate its output light intensity. Note that the LED is usually a non-coherent source and only intensity modulation is feasible. For this, the electrical current signal should be positive, thus a direct-current (DC) component is usually added to it to insure that the modulating signal is unipolar, *i.e.*, positive-valued. After being focused by an optional cover lens, this generated light intensity signal propagates through the indoor VLC channel towards the receiver. A lens could be employed at the receiver to collect the projected light intensity signal on the photo-detector (PD), which is usually a P-i-N (PIN)-diode. Then the resulting photo-current is passed to a transimpedance amplifier (TIA) circuit, prior to being sampled by an analog-to-digital converter (A/D). Finally, after signal demodulation, the original transmitted information bits are recovered.

In this chapter, we describe briefly the general components used in the indoor VLC system described above. In Section 2.2, we give details about the transmitters by explaining different types of LEDs commonly used in VLC systems and discuss the potential issues such as limited bandwidth and non-linear characteristics of these components. In Section 2.4, we study the physical indoor VLC channel by presenting the baseband channel model and different indoor link scenarios. In Section 2.3, we describe the photo-detector and also discuss the receiver design in VLC systems. Then in Section 2.5, we explain the commonly-used modulation schemes for VLC, including the baseband

pulse modulations and multi-carrier modulations, and review the possible solutions for addressing the dimming control problem. Lastly, Section 2.6 concludes this chapter.

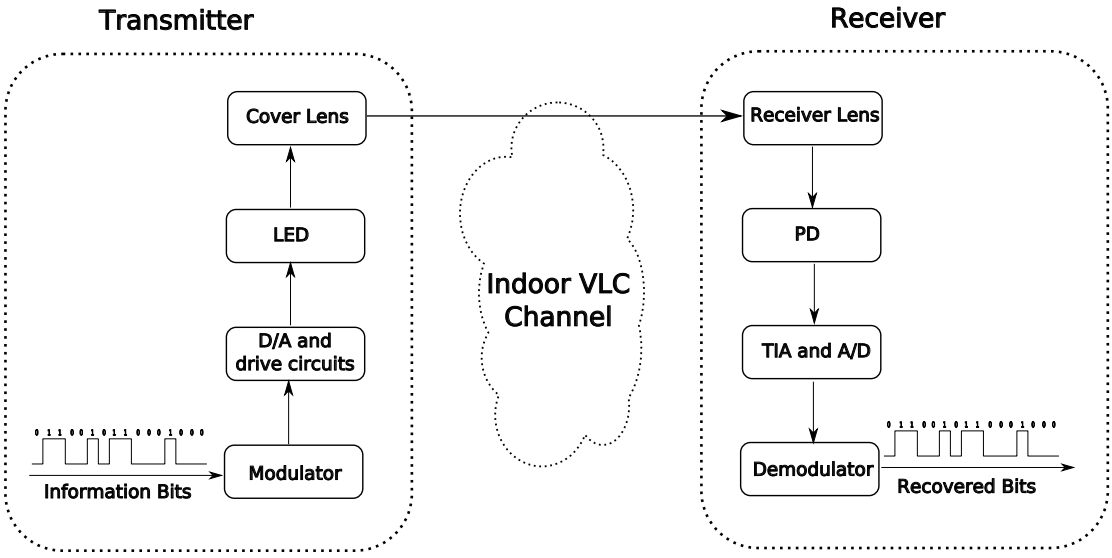

Figure 2.1 — The general block diagram of a typical VLC system

2.2 Transmitter

2.2.1 LED types

An LED is a small p-n junction diode which can emit light when fed with an electrical current. Compared to other artificial lighting sources such as incandescent bulbs and fluorescent lamps, LEDs have advantages such as compact size, high energy efficiency and long lifespan [13]. What is more important, LEDs have a relatively fast response and thus can also be used for optical communications in addition to their original illumination purpose.

Two different types of LEDs widely used in VLC systems are RGB LEDs and phosphor-based LEDs (also known as white LEDs). RGB LEDs consist of red, green and blue chips, and are able to produce any color by mixing different amounts of the three primary colors. Moreover, each color can be separately modulated and together they can offer a higher capacity through wavelength-division multiplexing (WDM) techniques [14–16]. The spectrum of the emitted light by an RGB LED is shown in Figure 2.2. The main problem with RGB LEDs is how to balance the red, green and blue components

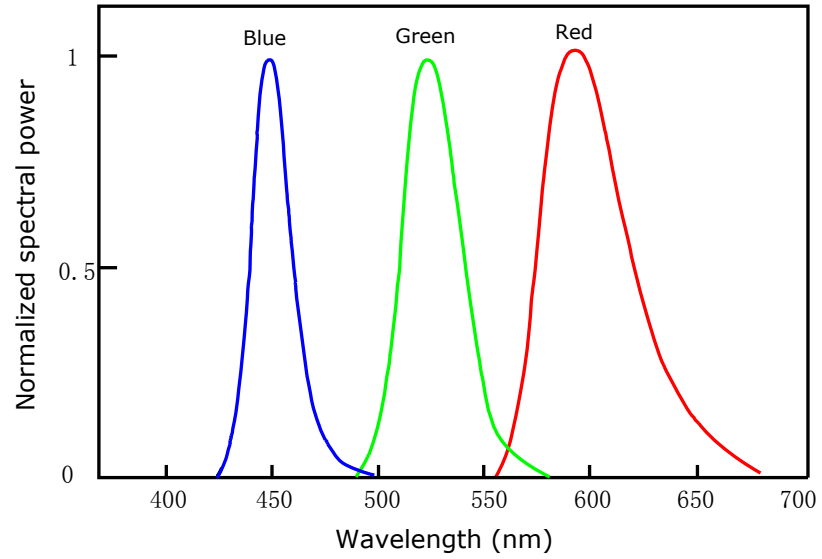

(a)

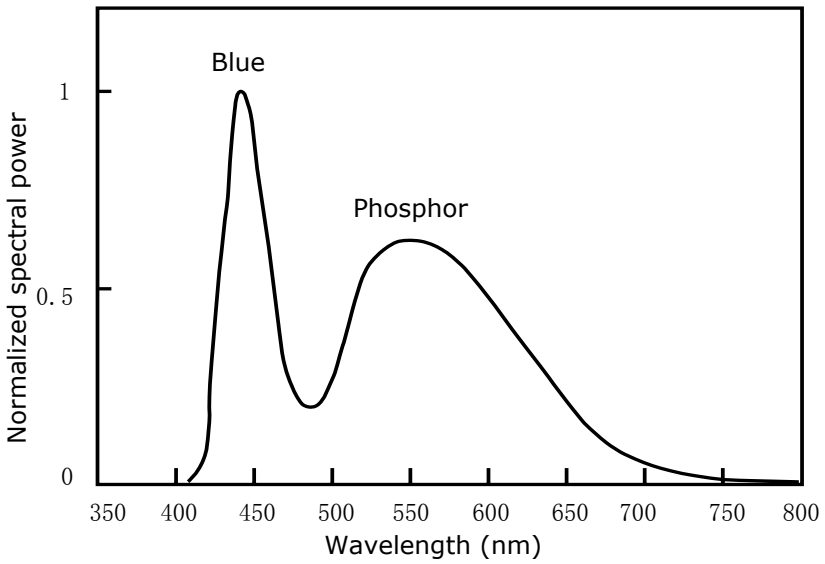

(b)

Figure 2.2 — Measured normalized power spectrum of a (a) RGB LED and (b) phosphorescent white LED, reproduced from [4, 17]

to obtain white light as the color of each component may change overtime, *e.g.*, due to rising temperature, which can lead to a substantial color shift [13]. For this reason, they are barely used in today's illumination market.

Another type of LEDs is the so-called white LED, where a blue LED is used together with yellowish phosphor coating to emit broad-spectrum white light, as shown in Figure 2.2. White LEDs have the advantages of lower cost and simpler structure, compared with RGB LEDs. For this reason, they are omnipresent in today's illumination market. The main drawback of these phosphor-based LEDs for the purpose of data transmission is their slow modulation response due to the slow phosphorous part, which leads to a relatively small modulation bandwidth of only a few MHz [18], hence limiting the transmission capacity of the VLC link. One approach is to use a blue filter at the receiver to remove the slow phosphor part of the spectrum [17]. In this way, the modulation bandwidth can be increased to about 20 MHz, but at the cost of relatively high power loss [19]. The data rate can be further improved by means of pre- or post-equalization, as proposed in [20,21]. Another approach is to employ high spectral efficiency modulations, *e.g.*, multi-level modulations or multi-carrier modulations, such as optical OFDM schemes, which we are going to study in Chapter 4.

Recently, researchers have also proposed using other types of LEDs for VLC, such as GaN-based micro LEDs [22,23] and organic LEDs [24]. Micro LEDs offers a much higher modulation bandwidth compared to phosphor-based LEDs, typically around 60 MHz. Organic LEDs, on the other hand, have a very limited modulation bandwidth around 100 KHz. In this thesis, we focus on the use of white LEDs for indoor VLC systems since they are the primary components used for the illumination of indoor environment. We will later consider solutions to overcome the limited modulation bandwidth of the white LEDs in order to obtain high data-rate signal transmission.

2.2.2 Modulation characteristics

As stated above, white LEDs usually have a raw modulation bandwidth limited to a few MHz. Thus, it is crucial to know their modulation characteristics before investigating appropriate signal processing techniques. The frequency response of an LED is determined by the carrier dynamics, *i.e.*, the carrier lifetime, and its parasitic capacitance. When driven by a low short pulse current, the frequency response of a white LED is very similar to a first-order low pass RC filter, which can be approximately written as [20]:

$$H(f) = \frac{1}{2\pi(f_c + jf)} \tag{2.1}$$

where f_c is the measured 3-dB cut-off frequency. However, this model provides poor accuracy in the high-frequency range [25]. Therefore, more precise modelling of the characteristics of the LEDs is necessary, which we are going to discuss later in Chapter 6.

2.2.3 Non-linear characteristics

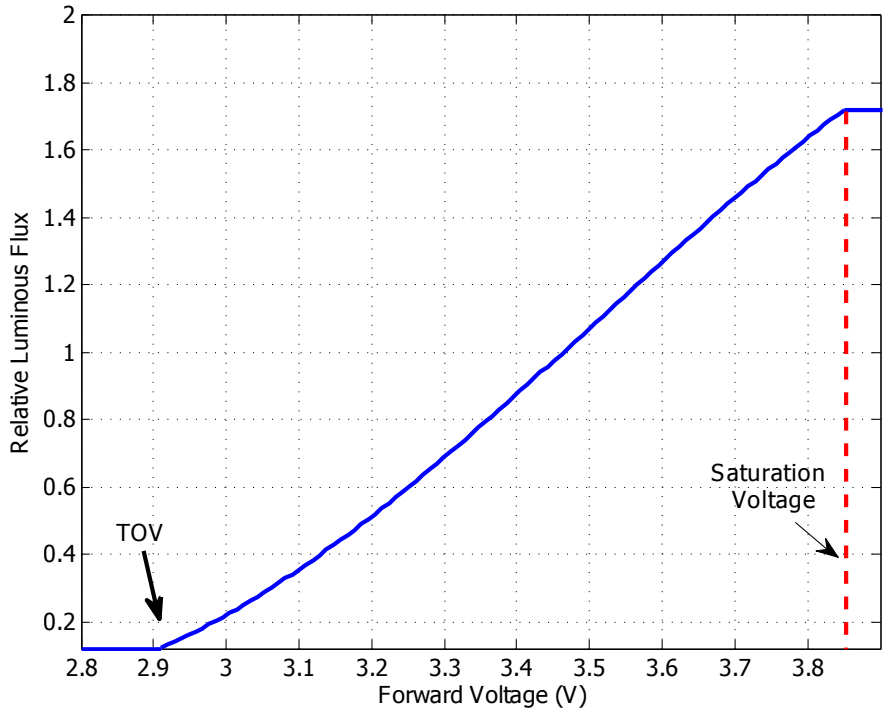

Figure 2.3 — The transfer function of the forward voltage-output optical power of a white LED (OSRAM LE CW E3B)

The non-linear characteristics of the LED transmitter is another important factor which should be taken into account for a practical VLC system. The non-linearity arises from two facts: On one hand, every LED has a dynamic operation range whose lower limit is known as the turn-on voltage (TOV) and upper limit known as the saturation voltage as illustrated in Figure 2.3. In other words, the TOV is the minimum driving voltage, below which the LED is considered to be in a cut-off region where no intensity is generated [26]. The saturation voltage corresponds to the maximum permissible alternative-current (AC)/pulsed current defined by manufacturers for avoiding the problems of overheating. Thus, any voltage outside the operation range should be clipped before being fed to the LED, which results in a non-linear distortion called clipping noise [27,28]. On the other hand, the number of generated photons of an LED is not usually directly proportional to the injected current, which leads to a non-linear relationship between the input current and the output optical power, as shown in Figure 2.3. These two kinds of non-linearity could highly degrade the system performance. Thus, detailed modelling is necessary for

designing proper modulation schemes and equalizations, which we will later elaborate in Chapter 6.

2.3 Receiver

The most commonly used photo detector in VLC system is the PIN photo-diode, which is based on the photoelectric effect. When stricken by photons of sufficient energy, it can generate free electron-hole pairs which produce correspondingly an electrical current. Note that a photo-diode is a non-coherent receiver as all the incident light of whatever phase and frequency contribute equally to this generated photo-current. The relationship between the incident optical power P_{opt} and the generated photo-current I can be expressed as [3]:

$$I = \frac{\eta e}{\hbar \nu} P_{\text{opt}} = R P_{\text{opt}} \tag{2.2}$$

where η is the quantum efficiency of the photo-diode, e is the electron charge, $\hbar$ is the Planck's constant, ν is the frequency of the incident light, and R is the responsitivity of the photo-diode.

In VLC systems, an optical concentrator (usually a lens) can be used at the receiver to collect as much as possible the incident optical signal. The system performance is improved by employing an optical concentrator since it increases the effective receiving area of the photo-diode. According to [29], the gain brought by an idealized optical concentrator can be written as

$$G(\varphi) = \begin{cases} \frac{n^2}{\sin^2(\varphi^2)} & 0 \leq \varphi \leq \text{FOV} \\ 0 & \varphi > \text{FOV} \end{cases} \tag{2.3}$$

where FOV is the field-of-view of the receiver, n is the refractive index of the lens, and φ is the incident angle.

2.4 Channel

In this section, we will overview the basic channel model and different link scenarios in VLC systems.

2.4.1 IM/DD Baseband model

As explained previously, only positive-valued signal can be transmitted in VLC systems as the emitted light intensity of the LEDs cannot be negative. Moreover, the frequency or phase of the transmitted signal can not be acknowledged at the receiver due to the non-coherent nature of the photo-diode. Therefore, the only convenient way of signal transmission is to use intensity modulation and direct detection (IM/DD) . As a result, the baseband equivalent model of a VLC link is similar to the case of infrared communication and can be written as [29]:

$$r(t) = GRs(t) \otimes h(t) + n(t) \tag{2.4}$$

where $r(t)$ is the instantaneous electrical current produced by the photo-diode, G is the optical concentrator gain, R is the responsitivity of the receiver photo-diode, $s(t)$ is the instantaneous optical power emitted by the LED, $\otimes$ denotes convolution, $h(t)$ is the channel IR, and $n(t)$ represents the receiver noise.

There are two main noise sources in VLC systems: shot noise and thermal noise where we denote the variances by σ_s^2 and σ_t^2, respectively. The shot noise originates from the random fluctuations of the generated photo-current [3] and is proportional to the projected optical power on the photo-diode, which consists of the useful signal and ambient radiations. In most VLC systems, the ambient light induced shot noise is dominant given the typical use of a PIN photo-diode, which can be modelled as a signal-independent zero mean additive white Gaussian noise (AWGN) [29,30]. Thermal noise is generated by the receiver electronic circuits and can also be modelled as a signal-independent zero mean AWGN. As a result, the overall noise component $n(t)$ is a AWGN of variance $\sigma_n^2 = \sigma_s^2 + \sigma_t^2 = BN_0$ where B is the signal bandwidth and N_0 is the one-sided noise power spectral density.

2.4.2 Link scenarios

The indoor VLC channel depends on many parameters, such as the room geometry, the radiation pattern of the LED lamp, the position, angle and FOV of the receiver, etc. Depending on whether or not there exists a LOS between the transmitter and receiver, the VLC channel can be categorized into three link scenarios: direct LOS, purely diffuse and hybrid links.

For direct LOS links, the transmitter and the receiver are pointed directly towards each other, as illustrated in Figure 2.4 (a). The LED transmitter has usually a narrow

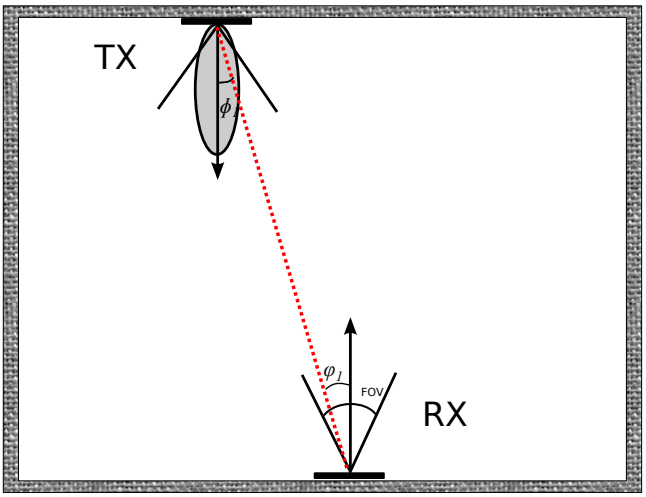

(a)

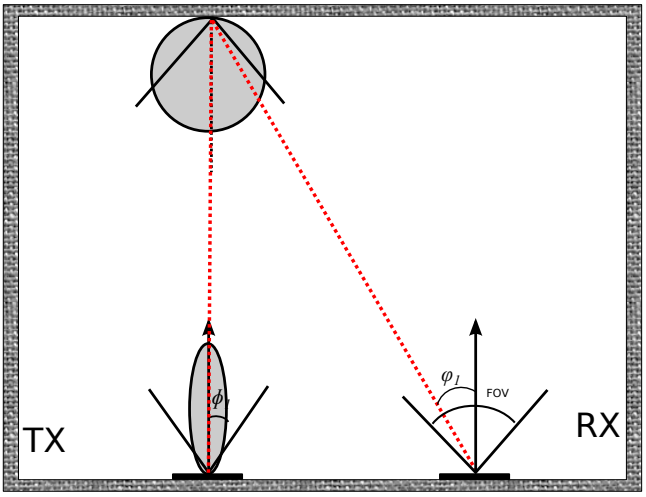

(b)

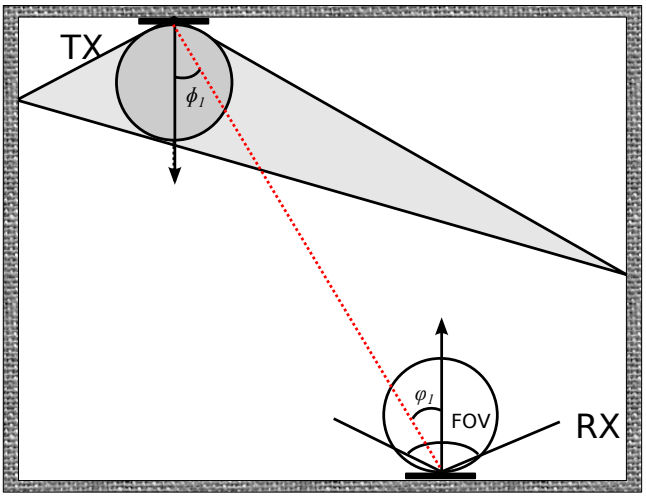

(c)

Figure 2.4 — Link scenarios for indoor VLC channel (a) direct LOS (b) diffuse (c) hybrid link

beam and the receiver has also a small field-of-view (FOV) in order to minimize the LOS path loss. The disadvantage of this configuration is that it needs a complex feedback tracking device to maintain a LOS path between the transmitter and the receiver in the case of receiver mobility. In contrast to the direct LOS link, the diffuse link does not need to have a direct LOS path. As shown in Figure 2.4(b), both transmitter and receiver are pointed towards the ceiling in this configuration. The light intensity signal is first diffusely reflected by the ceiling before reaching the receiver. In this way, it allows a maximum receiver mobility, but at the cost of large power loss and high channel dispersion. The most common link configuration in VLC system is the hybrid link shown in Figure 2.4(c), where the indoor channel contains contributions from both the LOS and diffuse part. This is usually achieved by employing wide-angle or multiple LED transmitters and receiver with a large FOV. It has advantages such as high power efficiency and low complexity, as well as allowing a sort of receiver mobility. For this reason, it is the most common link configuration in VLC systems as it offers a good compromise between power efficiency and system complexity.

2.5 Modulation techniques

As explained previously, IM/DD is used in VLC systems. In this section, we review the most widely used IM/DD modulation schemes by focusing on pulse modulation techniques and multi-carrier techniques. Note that it is also important for these modulations to support dimming control, which we discuss in Appendix A.

2.5.1 Pulse modulation techniques

By pulse modulation techniques, the information is transmitted by a train of pulses. Popular pulse modulation schemes include binary-level modulations such as on-off keying (OOK), pulse position modulation (PPM), and multi-level modulations such as PAM. These modulations are distinguished by different power and spectral efficiencies, as explained in the following.

NRZ-OOK

OOK is the simplest intensity modulation scheme where the information bits are sent by switching on (bit 1) and off (bit 0) the transmitter for a given symbol duration. There are two different types of OOK: return-to-zero (RZ) and non-return-to-zero (NRZ) where the

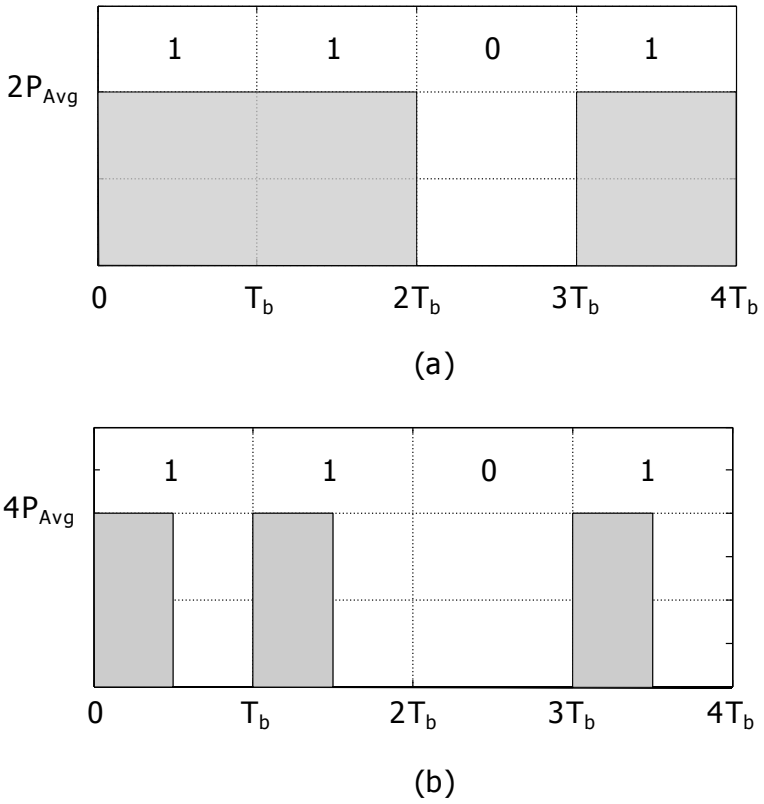

Figure 2.5 — An example of (a) NRZ-OOK (b) RZ-OOK of duty cycle of 0.5

difference lies on the pulse width representing a bit 1. For NRZ-OOK, the pulse duration equals the symbol duration, while for the RZ scheme, the pulse occupies only a part of the symbol duration (which is called duty cycle). Figure 2.5 illustrates an example of NRZ and RZ OOK (with a duty cycle of 0.5) for a given average transmit optical power of P_{Avg}. Since OOK is a binary modulation scheme, the bit error rate (BER) of OOK $P_{\text{BER,OOK}}$ for an AWGN channel is equal to its symbol error rate (SER), which is given by [31]

$$P_{\text{BER,OOK}} = Q\left(\sqrt{\frac{E_b}{N_0}}\right), \tag{2.5}$$

where E_b is the average energy per bit at the receiver, N_0 is the one-sided noise power spectral density, and $Q(\cdot)$ is the is the Q-function which is defined as $Q(x) = 1/\sqrt{2\pi}\int_x^\infty \exp(-u^2/2)du$.

In the case of an AWGN channel, E_b of NRZ-OOK is given by

$$E_{b,\text{NRZ-OOK}} = 2(GRP_{\text{Avg}})^2 T_b \tag{2.6}$$

where G is the concentrator gain, R is the responsitivity of the photo-diode, and T_b is the bit duration. For RZ-OOK with a duty cycle γ, the average energy per bit for the same P_{Avg} is increased by a factor of $1/\gamma$ as

$$E_{b,\text{RZ-OOK}} = \frac{2(GRP_{\text{Avg}})^2 T_b}{\gamma}. \tag{2.7}$$

The signal bandwidth for a symbol duration T_b for NRZ-OOK and RZ-OOK are $1/T_b$ and $1/(\gamma T_b)$, resulting in bandwidth efficiencies of 1 and $1/\gamma$ bit/s/Hz, respectively. As a result, the RZ-OOK scheme with $\gamma = 0.5$ illustrated in Figure 2.5 has a 3 dB performance gain in terms of electrical powerb(or 1.5 dB gain in terms of average optical power) compared with OOK-NRZ, but this advantage comes at the expense of twice bandwidth requirement. Although allowing a low complexity transceiver, OOK has a limited usage for high data-rate transmission due to its relatively low bandwidth efficiency.

PPM

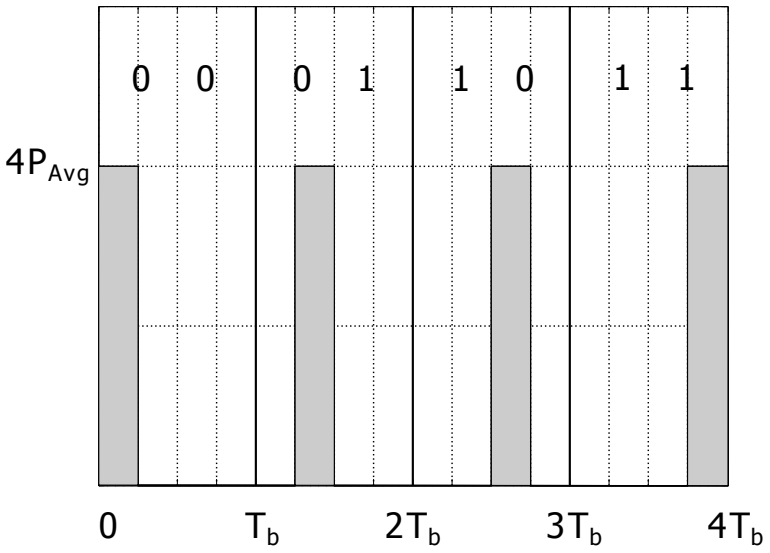

Figure 2.6 — An example of 4-PPM modulation

PPM is another popular modulation scheme that achieves a better power efficiency than OOK but at the cost of increased bandwidth requirement, *i.e.*, lower bandwidth efficiency. The symbol duration of an M-PPM is subdivided into M slots and the transmitter is only switched on during one of the slots with the remaining slots being empty.

In this way, the information bits are encoded into the position of the pulse within the symbol duration. Figure 2.6 shows an example of a 4-PPM modulated signal for a given P_{Avg}. The analytical BER expression of a M-PPM is difficult to derive, however, a lower bound on the BER of an M-PPM can be written as [31]:

$$P_{\text{BER},M-\text{PPM}} \geq \frac{M}{2} Q\left(\sqrt{\frac{ME_b}{2N_0}}\right). \tag{2.8}$$

M-PPM needs less electrical or optical power than OOK for achieving the same BER but its bandwidth efficiency is $\log_2(M)/M$, which is lower than OOK [32]. For this reason, PPM is usually used in power sensitive systems where bandwidth is not a major concern.

PAM

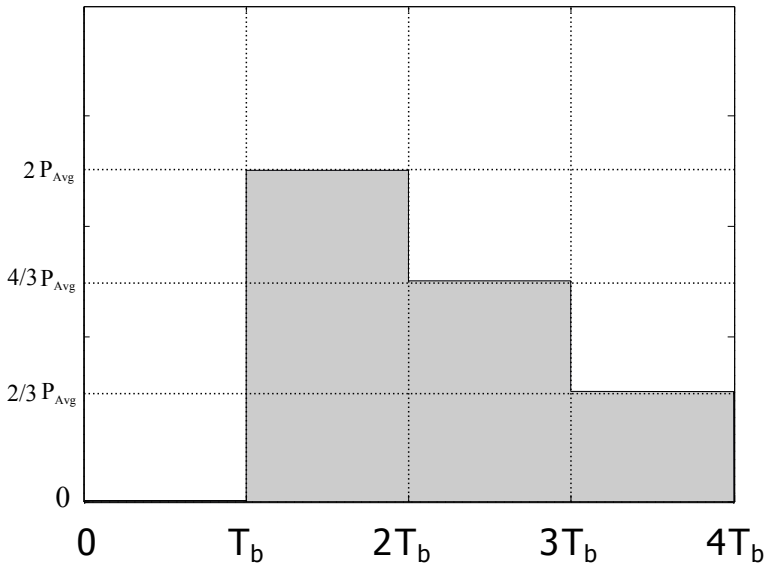

Figure 2.7 — An example of 4-PAM modulation

In contrast to binary intensity modulations such as OOK and PPM, PAM is a multi-level intensity modulation scheme. The information bits for unipolar M-PAM are encoded by different intensity levels which are given by:

$$P_m = \frac{2mP_{\text{Avg}}}{M-1} \quad \text{for} \quad m = 0, 1, \ldots .(M-1) \tag{2.9}$$

An example of a 4-PAM modulated optical signal is illustrated in Figure 2.7. A lower

bound on the BER of an M-PAM can be written as [31]:

$$\mathrm{BER}_{M-\mathrm{PAM}} \geq \frac{2(M-1)}{M\log_2(M)} Q\left(\frac{1}{M-1}\sqrt{\frac{E_b}{N_0}}\right). \tag{2.10}$$

The bandwidth efficiency of M-PAM is $\log_2(M)$ bit/s/Hz, therefore, it could provide a higher bandwidth efficiency than OOK and PPM but at the expense of reduced power efficiency.

2.5.2 Muti-carrier modulation techniques

One major disadvantage of the pulse modulation techniques presented above is that they may suffer from intersymbol interference (ISI) caused by multipath propagation of the indoor VLC channel and the frequency response of the LEDs. This will necessitate computationally complex equalization techniques at the receiver in the case of high data-rate transmission. Multi-carrier modulation schemes and in particular, optical OFDM schemes, efficiently resolve this problem and can achieve a high bandwidth efficiency. By optical OFDM, the signal bandwidth is divided into a number of narrow bands which are transmitted in parallel. This way, the symbol duration corresponding to each sub-carrier is much longer than the delay spread caused by the frequency selective channel. In addition, the insertion of a guard interval called cycle prefix (CP) at the beginning of each OFDM symbol ensures that the channel can be equalized using a simple one-tap equalizer at the receiver. The modulation and demodulation of an OFDM signal can be realized using an inverse fast Fourier transform (IFFT) and a fast Fourier transform (FFT), respectively, which enables simple and efficient implementation. The detailed review of optical OFDM schemes and their performance for indoor VLC systems will be later presented in Chapter 4.

2.6 Chapter summary

We reviewed the fundamentals of a general VLC system in this chapter by giving details on the main parts that form an indoor VLC link. The LED transmitters and their characteristics were presented in detail, together with discussions on the receiver design, indoor VLC channel, and signal modulation. We have also specified the main assumptions that we make for later use summarized in the following:

1. Use of white LEDs at the transmitter with limited dynamic range and non-linear

transfer function. The frequency response of the LED is modelled by a first-order low-pass filter.

2. IM/DD signaling.
3. Hybrid link configuration which includes the LOS and the diffuse components.
4. Use of a PIN PD without an optical concentrator at the receiver.

CHAPTER 3

Study of the VLC channel

3.1 Introduction

The purpose of this chapter is to investigate limitations arising from the indoor VLC channel and to determine the situations where it can effectively limit the data transmission rate.

The effect of the propagation channel depends on several parameters, including the room geometry, transceiver arrangement and the reflectivity of the inner surface, and is totally characterized by the channel IR. Generally, the IR of an indoor VLC channel consists of two parts: the LOS response corresponding to the direct paths between the transmitter and the receiver and the diffuse part corresponding to multiple reflections of the light before reaching the receiver. The LOS can be easily calculated for a given room geometry and source and receiver positions. However, the accurate evaluation of the diffuse part is far to be an easy task. Numerous experimental studies were carried out in [33, 34] using either the short pulse method or the frequency sweep technique. These studies validated the basic diffuse reflection model and studied the impact of the orientation of the transmitter and the receiver. However, experimental studies are usually very specific and will lose their interest if we have a totally different link configuration. Statistical models were developed in [35] and have shown the importance of the radiation pattern of the transmitter and the FOV of the receiver. However, these models are of limited usage for quantifying the real limitation that could arise from the channel. For this reason, simulation-based methods are commonly used in the literatures as they offer the flexibility to determine the channel characteristics for different link configurations. Among the simulation-based techniques, ray-tracing technique is a very popular approach which offers a good precision in evaluating the impulse response of the indoor VLC

channel [36–38]. However, this method needs exuberant computations in case of high reflection orders. In addition, existing ray-tracing simulation software are very expensive. A *recursive* method was developed in [39] and a fast geometric approach was introduced in [40] to simulate the IR of the indoor optical channel. However, these methods are still limited by their high computational complexity in case of high reflection orders, like the ray-tracing approach. An *iterative* approach was later proposed in [41] to improve the performance of the *recursive* approach. This method makes a good compromise between complexity and precision in simulating the IR. For this reason, we have reimplemented it using dynamic programming in order to simulate and characterize the indoor VLC channel.

Using this developed simulation tool, we investigate the limitations arising from the indoor propagation channel on data transmission. Our main contribution in this chapter resides in demonstrating the usefulness of the signal-to-ISI ratio in determining the degree of channel frequency selectivity and also in clarifying the role of the receiver filter for baseband VLC systems. The remainder of this chapter is organized as follows: In Section 3.2, we describe the transmitter and receiver model together with the detail of our method to simulate the channel IR. In Section 3.3, we present three different metrics for quantifying the channel frequency selectivity. Some numerical results are given in Section 3.4 by considering several practical indoor VLC link scenarios. The effect of the receiving filters and the impact of ISI on the BER performance for a baseband VLC system using OOK modulation are also discussed in this section. Lastly, Section 3.5 concludes this chapter.

3.2 Simulation of indoor channel IR

In this section, we explain the method we used to simulate the IR of the indoor VLC channel.

3.2.1 Propagation model

The channel IR consists of contributions from the LOS and multiple reflections (diffuse) paths. For a given LED transmitter and receiver, the channel IR can be written as

$$h(t) = \underbrace{V_i\, T(\phi_i)\, \frac{A_r(\varphi_i)}{d_i^2}\, \delta(t - \frac{d_i}{c})}_{\text{LOS}} + \underbrace{\sum_{k=1}^{\infty} h^k(t)}_{\text{Diffuse}}. \tag{3.1}$$

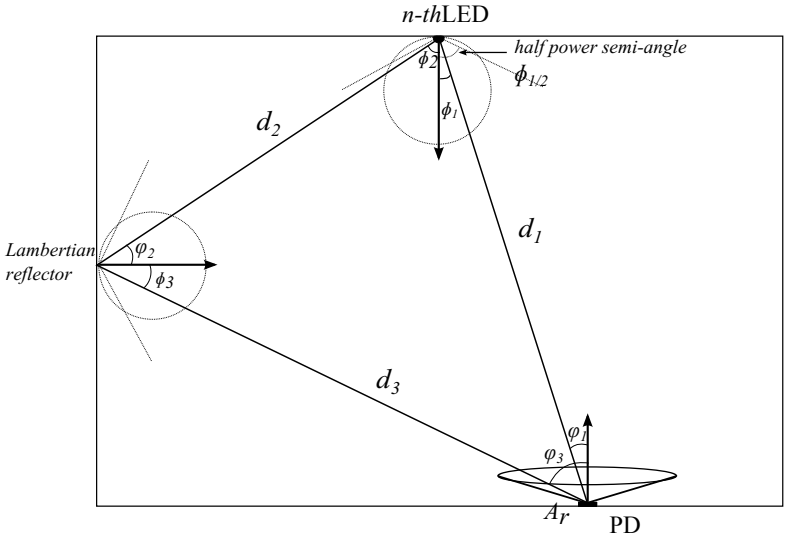

Figure 3.1 — Propagation model for the indoor VLC channel.

where $\delta(.)$ denotes the Dirac delta function, V_i is the visibility function which is set to 0 when the LOS path between the transmitter and the receiver is blocked, and to 1 otherwise, ϕ and φ denote the emitting and incident angles, respectively, as illustrated in Figure 3.1, $A_r(\cdot)$ is the effective receiving area of the PD, d_i is the link distance, c is the speed of light, and $T(\cdot)$ is the radiation pattern of the LED transmitter. In this chapter, we assume a Lambertian radiation pattern for the LED transmitters as

$$T(\phi) = \frac{m+1}{2\pi}\cos^m(\phi), \tag{3.2}$$

where m is the Lambertian order, which is related to the semi-angle at half power $\phi_{1/2}$ of the emitter as: $m = -\ln 2/\ln(\cos(\phi_{1/2}))$.

The LOS part of the IR can be directly calculated using (3.1). However, calculating the diffuse component is far to be an easy task as it contains light that undergoes multiple reflections. We have adopted the iterative site-based method for evaluating the non-LOS components. By this method, the inner surface of the room and the objects inside it are firstly decomposed into N tiny Lambertian reflecting elements with a given reflectivity. The k reflection response $h^{(k)}(t, S, R)$ for a given pair of source S (i.e., an LED or a reflecting surface) and receiver R (i.e., a surface or the PD) can be approximately evaluated as [41]:

$$h^{(k)}(t, S, R) \approx \sum_{n=1}^{N} \rho_{\varepsilon_n} h^{(k-1)}(t, S, \varepsilon_n^r) \otimes h^{(0)}(t, \varepsilon_n^s, R), \tag{3.3}$$

where ε_n^r and ε_n^s represent the n-th element ε_n acting as a receiver and a source, respectively, and ρ_{ε_n} is the reflectivity of ε_n. It is worth mentioning that the convolution in Equation (3.3) can be greatly simplified since $h^{(0)}(t, \varepsilon_n^s, R)$ is the LOS IR between the element n and R and is just a shifted Dirac delta function according to (3.1). Equation (3.3) implies that the k-reflection response can be recursively calculated using response corresponding to less k reflections. In order to reduce the computational complexity, we implemented this method in an *iterative* way. The pseudo-code of this algorithm using dynamic programming can be found in Appendix B.

3.3 Channel characterization metrics

Based on the simulated IR of the indoor propagation channel, we consider different criteria to quantify the limitation on the transmission rate, including conventional metrics such as the channel frequency response and the root-mean-square (RMS) delay spread, and also the rather-new metric of signal-to-ISI ratio.

3.3.1 Conventional metrics

Two conventional channel characterization metrics are the 3-dB cut-off frequency and ther RMS delay spread. Let us denote the channel frequency response by $H(f)$. The 3-dB channel cut-off frequency f_c corresponds to:

$$|H(f_c)|^2 = 0.5|H(0)|^2. \tag{3.4}$$

The RMS delay spread μ is given by [29]:

$$\mu = \left[\frac{\int_{-\infty}^{\infty} (t-\tau)^2 \, h^2(t) \, dt}{\int_{-\infty}^{\infty} h^2(t) \, dt} \right]^{1/2}, \tag{3.5}$$

where τ is the channel mean excess delay, defined as the square root of the second central moment of the IR squared [29]:

$$\tau = \frac{\int_{-\infty}^{\infty} t \, h^2(t) \, dt}{\int_{-\infty}^{\infty} h^2(t) \, dt}. \tag{3.6}$$

These two metrics are commonly used in RF to characterize the degree of channel frequency selectivity. However, they are of limited usage in the VLC context. This is because the propagation channel usually involves several LOS paths with different delays from multiple LED transmitters, as we demonstrate in Section 3.4.

3.3.2 Signal-to-ISI ratio

The signal-to-ISI ratio that we denote by SIR is defined as:

$$\mathrm{SIR} = \frac{P_{R,\mathrm{sig}}}{P_{R,\mathrm{ISI}}}, \tag{3.7}$$

where $P_{R,\mathrm{sig}}$ and $P_{R,\mathrm{ISI}}$ is the received powers corresponding to the 'desired' signal and the ISI, respectively. A high SIR corresponds to an almost frequency non-selective channel whereas a relatively low SIR signifies the need to channel equalization at the receiver. Let P_R be the total received power corresponding to a transmitted symbol. In some previous works (e.g., in [42]), $P_{R,\mathrm{sig}}$ is considered as the optical received power during the symbol duration T_s and $P_{R,\mathrm{ISI}}$ as the received power outside T_s. In other words, it is assumed that:

$$\begin{aligned} P_{R,\mathrm{sig}} &= P_R(t \leq T_s), \\ P_{R,\mathrm{ISI}} &= P_R(t > T_s). \end{aligned} \tag{3.8}$$

Here we consider a more realistic definition for $P_{R,\mathrm{sig}}$ and $P_{R,\mathrm{ISI}}$ that has a more practical interest. In fact, at the receiver, the electrical signal is filtered and then sampled prior to detection. Therefore, it is more reasonable to define the SIR after signal sampling. Let us consider the transmitted signal as follows:

$$x(t) = \sum_j a_j \, g(t - jT_s), \tag{3.9}$$

where a_j denotes the j-th transmitted symbol (equal to zero or one for the case of NRZ-OOK modulation, for example) and $g(t)$ is the pulse shaping filter. At the receiver, considering a sampling rate of $1/T_s$ and assuming negligible noise, the signal corresponding to the time sample j is given by:

$$y_j = a_j \, p(0) + \sum_{m \neq j} a_m \, p((j-m)T_s), \tag{3.10}$$

where $p(t) = g(t) \otimes h(t) \otimes r(t)$ with $r(t)$ being the IR of the receiver filter. Notice that in (3.10), a_j is the desired signal and the right-hand-side term is in fact the ISI. We

accordingly define the SIR as follows:

$$\mathrm{SIR} = \frac{\mathrm{E}[a_j^2][\,p(0)\,]^2}{\sum\limits_{m\neq j} \mathrm{E}[a_m^2]\,\big[\,p((j-m)T_s)\,\big]^2}, \tag{3.11}$$

where $E[\cdot]$ stands for the expectation. Assuming power-normalized symbols and also normalized channel with respect to the main LOS path, Equation (3.11) can be simplified as:

$$\mathrm{SIR} = \frac{[\,p(0)\,]^2}{\sum\limits_{m\neq j} \big[\,p((j-m)T_s)\,\big]^2}. \tag{3.12}$$

The pulse shaping filter $g(t)$ is usually chosen as a rectangular shape for the case of pulse modulation. At the receiver, we may consider the optimal matched filter (MF) which allows to maximize the signal-to-noise ratio (SNR) at the sampling times. However, the design of the MF becomes a complex task when we should deal with non-white noise (note that we consider here an analogue receiver filter and a sampling rate of one sample per symbol duration). For instance, if a large area PD (of relatively large capacitance) is used, the f^2-noise can be non-negligible [43]. This will necessitate a sharp roll-off of the filter transfer function in the stop-band. A suitable choice is a Bessel filter (BF), which has a constant group delay in its pass-band. Alternatively, other filter types can be used such as a Butterworth filter, as suggested in [32]. These filters have the advantage of providing a sharper transition between the pass-band and the stop-band for a given filter order, but at the cost of significant group delay distortion for high orders. We elaborate the impact of different receiver filters in the next section.

3.4 Numerical results

We present here some numerical results to study the indoor multiple propagation channel and investigate its limitations on the maximum transmission rate before necessitating equalization at the receiver.

3.4.1 Main assumption and link configuration

We consider the case of a medium-size room as shown in Figure 3.2. An array of (2×2) LEDs is considered, positioned on the ceiling as shown in Figure 3.4(a). We particularly study three receiver positions of R_1, R_2, and R_3 with coordinates

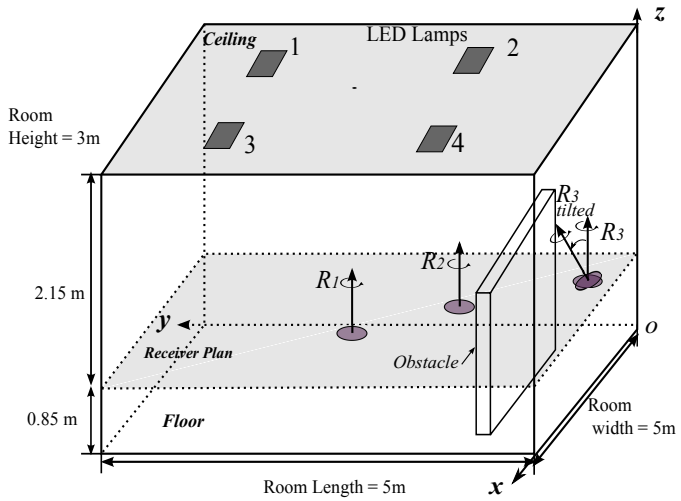

Figure 3.2 — An indoor VLC system configuration in a medium-size room.

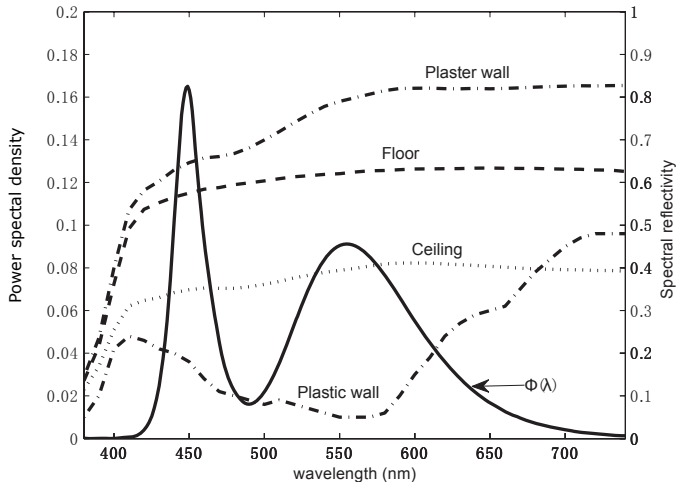

Figure 3.3 — Power spectral density $\Phi(\lambda)$ of a white LED (solid line, which corresponds to the left axis) and the measure spectral reflectance (which corresponds to the right axis) of plastic and plaster wall, floor, and ceiling, reproduced from Figure 1 in [44].

(2.5 m , 2.5 m), (1.25 m , 1.25 m) and (0.5 m , 0.5 m), respectively, at a height of 0.85 m above the floor. Receivers are pointing upward (i.e., vertically towards the ceiling) and we do not consider any receiver lens. The reflecting surfaces of walls, floor, and the ceiling are assumed of plastic materials and as Lambertian reflectors of order 1. Note that, although the surface reflectivity is usually wavelength dependent, it is quite difficult to perform the simulations in the whole visible spectrum by considering this dependency, from the point of view of computational complexity. To simplify the simulations, we have used the results in Figure 3.3 and calculated the average reflectivity over the entire visible spectrum. This is a good approximation if the maximum number of reflections considered in the simulations is not too high [44]. The calculated average reflectivities together with the other parameters adopted in our simulations are specified in Table 3.1.

We also consider two un-typical, yet realistic, situations: when all LOS paths are blocked by an obstacle, and when the receiver is tilted with respect to the vertical axis. For the blocked LOS case, we consider an obstacle of length, width, and height of 1.75, 0.25, and 2 m, respectively, at the origin coordinates (0.75 m , 0.25 m , 0) as shown in Figure 3.2. The surface reflectivity of this obstacle is set to the same as of the wall.

Furthermore, in order to investigate the impact of the room size and multiple LOS paths from different LED transmitters , we consider a relatively large room of dimension $(10\times10\times4)\,\mathrm{m}^3$ with an array of (4×4) LED lamps on the ceiling. The layout of the LED lamps for this case is shown in Figure 3.4(b). We investigate three receiver positions that we denote by R'_1, R'_2, and R'_3 at the coordinates (5 m , 5 m), (2 m , 2 m), and (0.5 m , 0.5 m), respectively.

To simulate the IR, we assume that the same signal is transmitted from all LEDs. For the case of a small-to-medium size room, the use of several LEDs has the advantage of offering space diversity in the sense of avoiding signal loss in the case of LOS beam blocking. Concerning the iterative site-based method that we use for simulating the IR, we consider a maximum reflection order of 3. Indeed, as it is shown in [41], the power contribution by considering more reflections is practically negligible for the typical VLC link that we considered here. The spatial resolution of the simulation method, i.e., the area of each reflecting surface, is set to 10 cm×10 cm. Also, the temporal resolution, i.e., the bin width of the simulated IR is set to 0.1 ns.

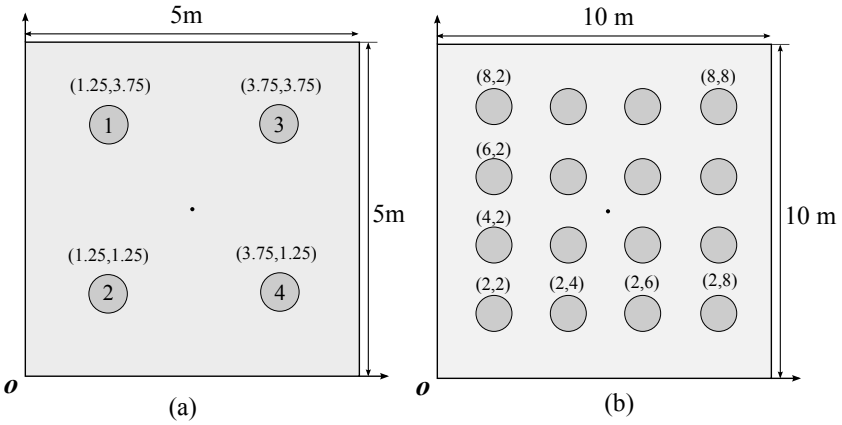

Figure 3.4 — The layout of LEDs on the ceiling for the two cases of: medium-size (a), and large (b) rooms of dimensions $(5\times5\times3)\,\mathrm{m}^3$ and $(10\times10\times4)\,\mathrm{m}^3$, respectively.

Table 3.1 — Parameters for simulating the indoor VLC channel

Parameter	Value
Ceiling reflectivity	0.38
Floor reflectivity	0.61
Wall reflectivity	0.74
Transmitter Lambertian order	1
Receiver FOV (half angle)	70°
PD active area	$1\,\mathrm{cm}^2$

3.4.2 Simulated IR

We have shown in Figure 3.5 the simulated IR of the LOS paths and those corresponding to one, two, and three reflections for the case of the medium-size room. Notice that the levels of different LOS components are indicated by labels for the purpose of illustration. R_1 and R_3 positions are considered together with the two cases of blocked LOS and tilted receiver for the latter. For the tilted receiver case, we consider a tilting angle of 30° towards the center of the ceiling (an untilted receiver points vertically towards the ceiling). This way, we have different LOS paths and also additional reflections from the floor and walls. At R_1, concerning the LOS component, we notice a single shifted Dirac delta function from Figure 3.5(a), which is due to the symmetry of the LED arrangement with respect to the receiver position in this case (see Figure 3.2). There are three shifted Diracs at R_3 (except for the blocked-LOS case), where we have a symmetry with respect

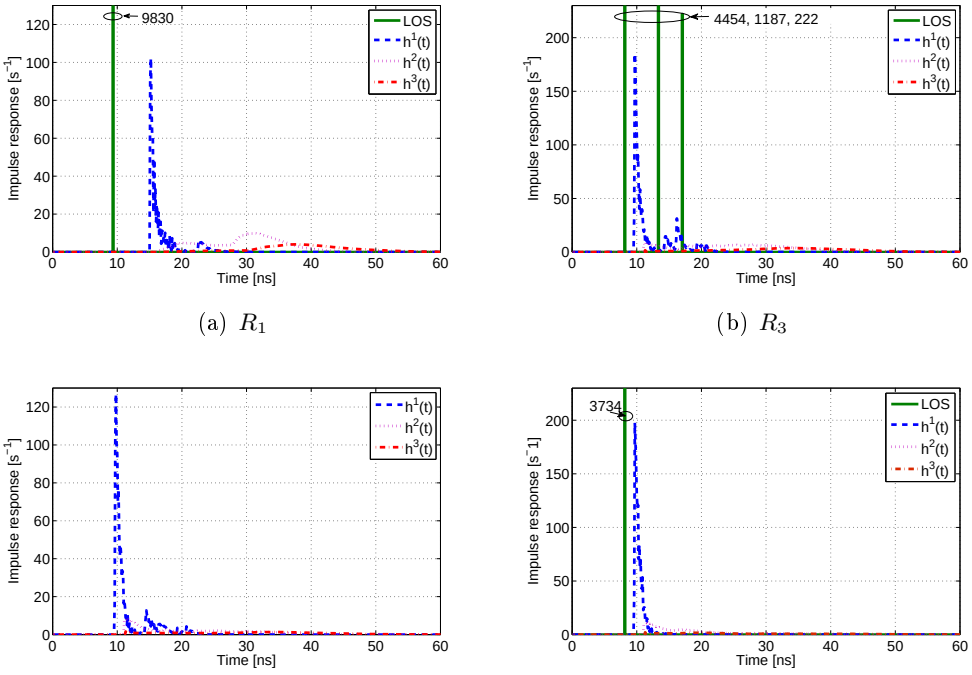

(a) R_1 (b) R_3

(c) R_3, Blocked LOS (d) R_3 Tilted receiver

Figure 3.5 — Medium-size room case, channel IR at receiver positions R_1 and R_3.

to LEDs 1 and 4. It is worth mentioning that since the LOS paths dominate the diffuse components in the IR, they are the main factor that determines the channel frequency selectivity. Lastly, we have an almost similar behavior for the cases of tilted and untilted receivers as in Figure 3.5(b), (d), apart from the received intensity level, as expected.

3.4.3 Investigating the frequency response

Let us now investigate the usefulness of the channel frequency response for evaluating the degree of channel frequency selectivity. We have presented in Figure 3.6 plots of normalized modulus of the channel frequency response for the case of medium-size room at receiver positions R_1, R_2, and R_3 (untilted and tilted receiver, and blocked LOS), as well as for the case of the large room at R'_3 position. Firstly, we notice that for R_1 position, the frequency response is almost flat except for data rates lower than about 30 MHz, which confirms the results of Figure 3.5: Here, the dominant factor is the LOS component, which is a single shifted Dirac delta function. Thus, it is quite reasonable to have an almost flat frequency response. However, we cannot determine an explicit

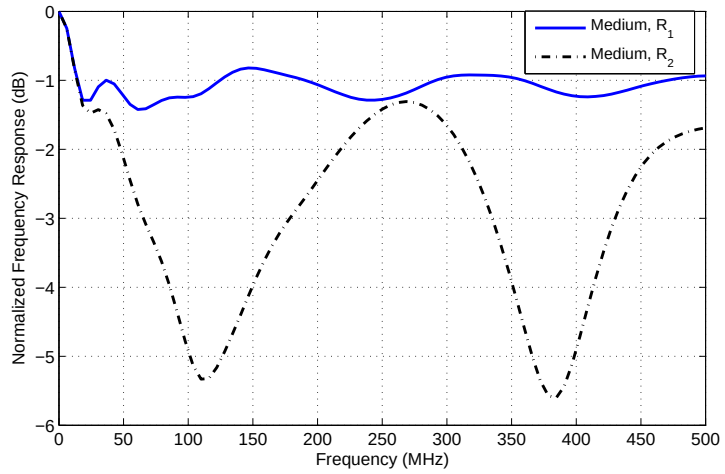

(a)

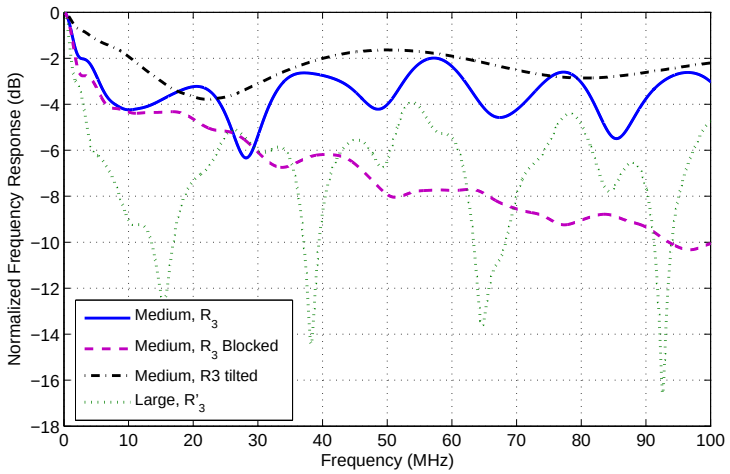

(b)

Figure 3.6 — (a) Medium size room with receiver at positions R_1 and R_2; (b) medium-size room at R_3 position for the cases of untilted and tilted receivers and blocked-LOS, and large room at position R_3'.

limitation on the data rate based on the frequency response. For the cases of R_2 and R_3 positions, we notice oscillations of a few decibels. Once again, the dominant factor is the LOS component of the IR, and since we have three shifted Dirac delta functions (see Figure 3.5), we have an oscillating behaviour. From Figure 3.6(b) we notice a somehow similar behaviour for the case of tilted receiver at R_3. For the case of R'_3 position in the large room, we notice more significant fluctuations (in amplitude) in the frequency response. The reason is the contribution of the 16 LOS paths of different delays to the IR; as a result, in certain frequencies we experience more severe "fades", compared to the previous cases for the medium-size room.

For all these studied cases, because of the oscillating behaviour of the frequency response (which is due to the contribution of the LOS component), fixing a 3 dB bandwidth for the channel is effectively useless. The 3 dB bandwidth becomes meaningful only for the purely diffuse channel in the case of blocked-LOS at R_3 position, which is about 43 MHz.

3.4.4 Investigating the RMS delay spread

Table 3.2 — Mean excess delay and RMS delay spread for different link scenarios. "LOS" refers to considering only the LOS component of the IR, whereas "Aggregate Channel" includes both the LOS and the diffuse components.

	Receiver position	RMS delay spread μ [ns]		Rice factor
		LOS	Aggregate channel	
Medium-size Room	R_1	0	0.26	3.56
	R_2	1.53	1.58	2.90
	R_3	1.69	1.76	1.43
	R_3, blocked LOS	0	4.37	0
	R_3, tilted	2.08	2.15	2.59
Large Room	R'_1	1.83	2.00	6.53
	R'_2	2.43	3.07	2.96
	R'_3	3.37	4.66	0.89

In order to evaluate the channel frequency selectivity based on the delay spread criterion, we calculate for different scenarios the mean excess delay τ and the RMS delay spread μ using the simulated aggregated IRs (i.e., taking both LOS and diffuse

components into account). At the same time, since both the asymmetry between the LOS paths (if any) and the diffuse component (non-LOS) contribute to the channel frequency selectivity, in order to see the significance of the former factor, we have also calculated τ and μ based only on the LOS component. The results are summarized in Table II where the two cases of medium-size and large rooms are considered. We have furthermore shown in the last column of the table the ratio of the total power corresponding to the LOS component to that of the diffuse component; what is usually referred to as "Rice-factor" in RF systems. Let us focus on the RMS delay spread and the case of medium-size room. At R_1, there is no delay spread corresponding to the LOS component due to the symmetry of LEDs arrangement with respect to the receiver position. We notice a larger μ for R_2 and R_3 positions, compared to R_1. The reason is that at these positions we have more asymmetry between the LOS paths and this results in a larger delay spread. We also note a slightly larger μ for the case of tilted receiver, which is quite logical. In fact, for a larger tilting angle, we receive more contribution from the LOS and also from the diffused light due to the reflections from the floor and the walls. Lastly, for the case of blocked LOS, we obtain a relatively large μ of more than 4 ns.

On the other hand, for the case of a large room, we notice generally larger delay spreads. Interestingly, here the major part of μ arises from the contribution of LOS, and taking the diffuse component into account affects the delay spread only slightly. As a matter of fact, the more significant factor affecting μ is the asymmetry between the multiple LOS paths (16 in total for the large room case). As expected, again the largest delay spread corresponds to the room corner, i.e., R_3' position.

As a matter of fact, although the study of the RMS delay spread seems to be useful in comparing the degree of channel frequency selectivity of the different link configurations, its absolute value cannot be used to determine the limitation on the transmission rate. For instance, for the case of the medium-size room at R_3 position, a μ of 1.76 ns would suggest that we can transmit with up to a rate of $\approx$ 500 Mbps with OOK signaling. However, as we will show later in the following, the data rate is much more constrained.

3.4.5 Investigating SIR

As mentioned previously, the interest of studying the SIR is that we can predict whether or not a channel equalization is necessary for a given transmission rate. In order to evaluate the SIR, for the sake of simplicity, we consider the NRZ OOK modulation. We obtain the received signal by convolving the transmitted OOK signal with the IR of the

channel and the receiver filter. Then, we calculate the SIR numerically using (3.8). Here, a_j, i.e., the "desired" signal sample is that corresponding to the highest amplitude. In other words, we assume perfect synchronization at the receiver where received pulses are sampled at their maximum [45]. Notice that this does not happen in practice as we cannot predict the exact sampling time, for instance, due to the imperfect knowledge of the channel, the receiver noise, and the clock frequency jitter of the transmitter and the receiver. The results we present here, hence, provide an optimistic estimation of the SIR.

Concerning the receiver filter, we consider the two cases of MF and a BF, as explained in Section 3.3.2. For the latter, we consider a fifth-order Bessel filter and set its 3-dB bandwidth to $R_b/2$, where R_b is the symbol rate since it results in the best SNR at the filter output [45]. We have presented plots of the SIR as a function of the transmission data rate in Figure 3.7(a) and 3.7(b) for the two cases of MF and BF, respectively. Generally, SIRs are relatively high for data rates lower than 10 Mbps, which means that we have effectively a flat channel. It is quite reasonable since the channel delay dispersion becomes negligible, compared to the symbol duration T_s. Note that for the case of MF, the SIR tends to infinity when data rate tends to zero. This is not the case, however, for the BF, since it does not fully satisfy the Nyquist criterion and introduces a small amount of ISI in the received signal [46].

We notice from the presented results a decrease in SIR as the data rate increases. Interestingly, this is not the case for R_1 position in the medium-size room: we notice an increase in SIR for data rates higher than about 40 Mbps. We can explain this phenomenon by considering the corresponding frequency response in Figure 3.6(a): Given that the frequency response is almost flat at high frequencies, we suffer from less distortion when shifting to larger bandwidths, i.e., high data rates. In other words, we can consider the diffuse component of the channel as a "low-pass" component that we can neglect at high frequencies, where the LOS component dominates. Note that this is also true for the other case studies but the particularity of R_1 position is that due to the symmetry in the LED lamp arrangement, we have one single Dirac as the LOS component of IR. For the other cases, the existence of several Dirac functions in the IR determines the SIR limitation at high data rates.

From Figure 3.7, the worst SIR corresponds to the case of R_3' in the large room where the limitation on the SIR arises from the numerous (i.e., 16) LOS paths that contribute to ISI at relatively high data rates. For the medium-size room, the case of blocked LOS at R_3 is reasonably much more constraining than the unblocked cases. Theses results are in accordance with the conclusions of the previous subsections.

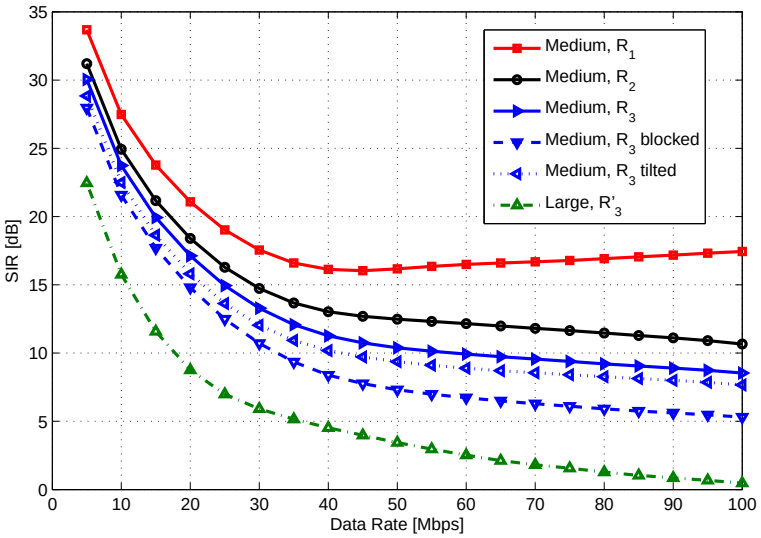

(a)

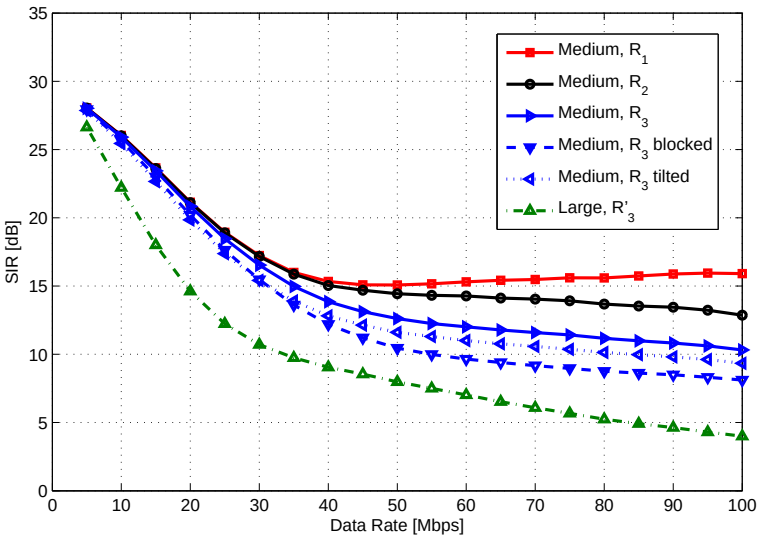

(b)

Figure 3.7 — SIR as a function of data transmission rate assuming simple NRZ-OOK signaling while taking into account the effect of: (a) Matched filter, and (b) Bessel filter.

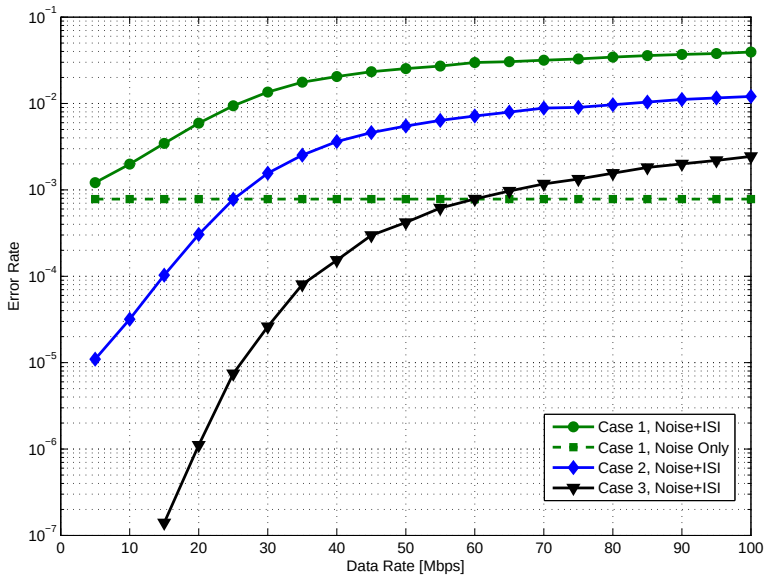

Figure 3.8 — Receiver BER as a function of the data transmission rate for R_3 position in the medium-size room. OOK modulation with MF at the receiver; Case 1: $E_b/N_0 = 10\,\text{dB}$, Case 2: $E_b/N_0 = 13\,\text{dB}$, Case 3: $E_b/N_0 = 16\,\text{dB}$.

Another interesting point is that SIRs are generally higher when using a BF (except at relatively low data rates less than 10 Mbps for medium-size room). As a matter of fact, as mentioned previously, the BF does not fully satisfy the Nyquist criterion and introduces a vertical eye-opening penalty of about 0.9 dB in the electrical domain for $h(t) = \delta(t)$, compared to the MF. However, the shape of the eye is significantly flatter near the sampling time. As a result, the BF is more tolerant to sampling time errors than the MF. For the same reason, it is also more robust against multipath dispersion.

Lastly, it is worth mentioning that at relatively high data rates (here, about more than 5 Gbps), the SIR tends to an asymptotic value. Indeed, by increasing the data rate, the transmitted pulses become more and more narrow, and at the limit, the received signal approaches the IR. This asymptotic value of SIR can be validated from the simulated IR results.

3.4.6 Effect of ISI on BER

In order to get more insight into the real impact of the ISI on the system performance, let us investigate the BERs. Assuming signal-independent AWGN of one-sided power

spectral density (PSD) N_0, we consider two case studies where we fix the electrical E_b/N_0 to 10, 13, and 16 dB. We will refer to them as Cases 1, 2, and 3, respectively. We consider NRZ-OOK modulation with MF at the receiver and assume perfect time synchronization and channel knowledge at the receiver. The BER of such scheme is given by Equation (2.5), which corresponds to 7.83×10^{-4}, 3.97×10^{-6}, 1.4×10^{-10} for Cases 1, 2, and 3, respectively. The mean optical transmit power P_t for NRZ-OOK is related to E_b according to the following equation:

$$P_t = \sqrt{\frac{E_b}{2T_b}}, \tag{3.13}$$

where we have normalized the received signal with respect to the PD responsivity and TIA gain, for simplicity. Results are shown in Figure 3.8, where we have presented plots of BER a function of the data rate for the case of R_3 receiver position for the medium-size room. The case of "ideal" flat channel, denoted by "Noise Only" on the figure, serves as the benchmark, for which the BER remains unchanged, irrespective of the data rate. The plots denoted by "Noise+ISI" correspond to the real channel and are obtained through Monte Carlo simulations. We can clearly notice the BER penalty due to ISI; this penalty becomes logically more important by increasing the data rate. For instance, if we consider a target BER of 7.83×10^{-4} (from Case 1, Noise Only), we have no ISI penalty at ∼1 Mbps (from Case 1, Noise+ISI); a 3 dB SNR penalty at ∼25 Mbps (from Case 2, Noise+ISI), and a 6 dB SNR penalty at ∼60 Mbps (from Case 3, Noise+ISI). These results are in accordance with those of Figure 3.7, that is, we suffer from more and more ISI by increasing the data rate.

3.5 Chapter summary

In this chapter, we simulated the impulse response of the aggregate indoor VLC channel using the iterative site-based method for different scenarios, and then investigated the necessity of channel equalization at the receiver. We showed that channel frequency selectivity arises mainly from the multiple LOS paths rather than diffuse propagation, i.e., multipath reflections. It can be relatively significant for large rooms where numerous LED lamps are used for illumination. We illustrated the interest of the proposed SIR metric in determining the degree of channel frequency selectivity. Meanwhile, we discussed the choice of the receiver filter and demonstrated the interest of using a Bessel low-pass filter, which provides a higher SIR at relatively high data rates, compared to the MF, for instance. The impact of the channel frequency selectivity was also shown through

numerical results on the receiver error rate. After this detailed analysis of the propagation channel, we will focus on the limitations arising from the LED transmitters in the next chapters and investigate appropriate signaling schemes that allow achieving high data-rate transmission.

CHAPTER 4

Optical OFDM for VLC

4.1 Introduction

Regarding the bandwidth limitation of the white LEDs explained in Section 2.2.2, in this chapter, we investigate the suitability of optical OFDM-based schemes at the aim of achieving high data-rate transmission in VLC systems.

OFDM is a multi-carrier modulation (MCM) scheme by which the data is carried over a number of spectrally spaced sub-carriers. The basic concept behind OFDM is that one single high data-rate stream is split into multiple streams of lower data-rate, which are transmitted in parallel on different sub-carriers. As a result, the symbol period corresponding to each sub-carrier is much larger than that of the equivalent single-carrier system so that the ISI affects at most one symbol. Moreover, by inserting a guard interval called CP, the inter-carrier interference (ICI) can be removed, allowing a simple channel estimation and equalization method at the receiver.

In addition to the advantages of robustness against channel dispersion and simple channel equalization, by assigning different data rate and transmit power per sub-carrier according to its channel characteristics, the data-rate of an OFDM-based system can be further maximized [47, 48]. Due to these interesting features, OFDM-based schemes have also been applied to VLC systems in order to overcome the limited modulation bandwidth of the LEDs. Since IM/DD is employed in VLC systems, the information-bearing signal must be real and positive before the intensity modulation of the LED. This is the most important difference between optical OFDM and the classic OFDM signaling used in RF systems. In this chapter, we present and describe three most commonly considered schemes in the VLC context, in particular, DCO-OFDM [14,23,49,50], ACO-OFDM [28,51–53] and PAM-DMT [54,55], while focusing later on DCO-OFDM.

OFDM-based schemes have been proven to be powerful in VLC systems to achieve

high data-rate transmission. Indeed, a record data rate of 513 Mbps was first reported in [49] on a single white LED using blue-filtering and bit-power-loading techniques. Data rates beyond Gbps have been also demonstrated in [14, 23, 50]. Despite their success, a major drawback of OFDM-based schemes is their relatively high PAPR. As stated previously, the LEDs in VLC systems have only a limited dynamic range beyond which the signal amplitude should be clipped. A high PAPR implies more severe signal distortion caused by the clipping effect. Moreover, OFDM signals could be further distorted by the non-linear transfer function of the LED due to their large peak signal amplitudes. Modelling the clipping effect for OFDM-based schemes has been discussed in [27, 28], where analytical solutions are derived based on the Bussgang theorem. However, there is a lack of study of optical OFDM signaling that takes into account the clipping effect and the LED frequency response at the same time, which is important from a practical point of view. Our main contribution in this chapter is to investigate this point while considering the most appropriate scheme, *i.e.*, DCO-OFDM. This chapter also provides an overview of the principles of OFDM-based schemes and investigates their applications in the VLC context.

The remainder of this chapter is organized as follows: In Section 4.2, we explain the fundamentals of an OFDM systems, including the principles of FFT as well as the role of CP. Then, in Section 4.3, we describe the three commonly used optical OFDM schemes for VLC systems and compare them in terms of PAPR performance. The clipping effect is also discussed in this section. In Section 4.4, we provide a set of numerical results to investigate the interest using optical OFDM schemes to achieve high data-rate transmission in VLC systems by taking into account both the clipping noise and the frequency response of the LED transmitter. Lastly, Section 4.5 concludes this chapter.

4.2 Principles of OFDM signaling

OFDM is a special class of frequency-division multiplexing (FDM) signaling with the general block diagram depicted in Figure 4.1. As seen, the information bits are sent over a number of sub-channels associated with a set of sub-carriers. The key difference between FDM and OFDM is that by OFDM sub-channels can overlap in frequency, however they do not interfere with each other due to the harmonic relationship between the sub-carriers (known as orthogonality). This way, densely-spaced sub-carriers can be used for data transmission, thus greatly increasing the achievable data-rate.

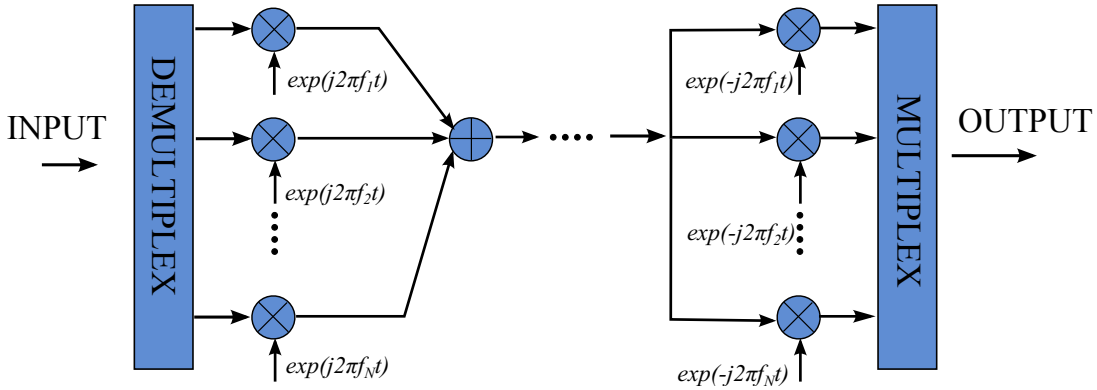

Figure 4.1 — Block diagram of a generic FDM system

For FDM systems, the transmitted signal $s(t)$ can be written as [2]:

$$s(t) = \sum_{i=-\infty}^{\infty} \sum_{k=0}^{N-1} x_{ik} s_k(t - iT_s) \tag{4.1}$$

where x_{ik} is the data carried by the k-th sub-carrier corresponding to the i-th FDM symbol, N is the number of sub-carriers, T_s is the symbol duration, and $s_k(t)$ is the waveform of the k-th sub-carrier that can be written as:

$$s_k(t) = \Pi(t) \exp\left(j2\pi f_k t\right), \tag{4.2}$$

where f_k is the frequency of the sub-carrier, $\exp(\cdot)$ is the exponential function, $\Pi(t)$ is the baseband pulse shaping filter which is usually a rectangular function given by

$$\Pi(t) = \begin{cases} 1 & 0 < t <= T_s \\ 0 & \text{otherwise} \end{cases} \tag{4.3}$$

Thus, the correlation between the m-th and n-th sub-carriers can be written as [2]:

$$\begin{aligned} \sigma_{mn} &= \frac{1}{T_s} \int_0^{T_s} s_m s_n^* dt = \frac{1}{T_s} \int_0^{T_s} \exp\left(j2\pi(f_m - f_n)t\right) dt \\ &= \exp\left(j2\pi(m-n)T_s\right) \frac{\sin(\pi(f_m - f_n)T_s)}{\pi(f_m - f_n)T_s} \end{aligned} \tag{4.4}$$

In the case of OFDM signaling, the frequency of the sub-carriers is chosen such that

$$f_m - f_n = 1/T_s \tag{4.5}$$

This way, from (4.4), we get $\sigma_{mn} = 0$, which means that the sub-carriers are orthogonal to each other. This ensures that the original information can be rather easily recovered at the receiver using matched filtering despite the relatively strong signal spectral overlapping.

4.2.1 DFT and IDFT

At the earlier time of the development of OFDM, one big challenge was the generation of a large number of orthogonal sub-carriers, which involved the use of a large number of oscillators and analog filters at the transmitter and at the receiver. In 1969, Weinstein *et al.* realized that the OFDM modulation and demodulation can be implemented using inverse discrete Fourier transform (IDFT) and discrete Fourier transform (DFT). Considering $s(t)$ within a symbol period T_s, if we sample it at the rate of N/T_s, the discrete samples $s_n, n = 0, 1, \ldots, N-1$, can be expressed as:

$$s_n = \sum_{k=0}^{N-1} x_k \exp\left(j2\pi f_k \frac{nT_s}{N}\right). \tag{4.6}$$

The orthogonality condition in (4.5) can be reformed as:

$$f_k = \frac{k}{T_s}, k = 0, 1, \ldots, N-1 \tag{4.7}$$

Substituting (4.7) into (4.6), we have:

$$s_n = \sum_{k=0}^{N-1} x_k \exp\left(j2\pi \frac{kn}{N}\right) = \text{IDFT}\{x_k\}. \tag{4.8}$$

In other words, according to (4.8), the sampled transmitted OFDM signal s_n is just an N-point IDFT of the information symbols x_k.

In a similar manner, the original information symbols x_k can be extracted from the received signal sampled at intervals of T_s/N using a DFT. Thus, the modulation(demodulation) of OFDM can be done digitally using IDFT(DFT) and a D/A(A/D) at the transmitter(receiver). This avoids using multiple oscillators and analog filters and greatly simplifies the system implementation. Moreover, the IDFT/DFT can be calculated using an efficient FFT algorithm, which further reduces the computational complexity of the system.

4.2.2 Cyclic prefix

CP refers to prefixing an OFDM symbol with a repetition of its end [2]. By inserting a CP at the beginning of every transmitted OFDM symbol, the distortion caused by a linear dispersive channel can be corrected using a simple one-tap equalizer.

To illustrate this, let us first consider two consecutive OFDM symbols of symbol period T_s, and a linear dispersive channel with a delay spread of t_d, as shown in Figure 4.2.A. The received symbols are the linear convolution of the transmitted OFDM

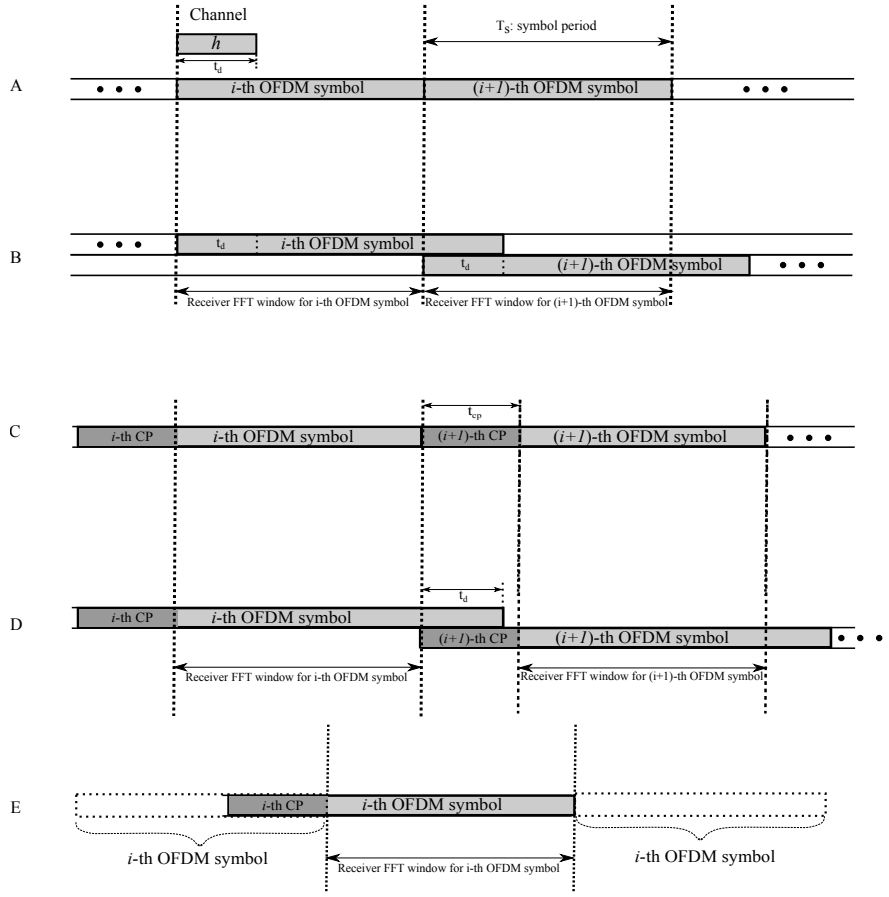

Figure 4.2 — A. Transmitted signal, B. Received signal, C. Transmitted signal with CP, D. Received signal with CP, E. Received i-th OFDM symbols.

symbols with the IR of the channel h, with a total length of $t_d + T_s$, see Figure 4.2.B. At the receiver, for detecting the transmitted symbols, the receiver DFT size should be the same as the length of the transmitted symbols, *i.e.*, N. It is clear from the figure that the received signal (within the i-th symbol receiver DFT window) is just a truncated

version of the complete received signal after passing through the dispersive channel. As a result, the orthogonality between the sub-carriers of the i-th and $(i+1)$-th symbols is no longer satisfied, resulting in an ICI penalty. Furthermore, a part of the received i-th symbol exceeds the symbol boundary T_s and "leaks" to the DFT window of the $(i+1)$-th symbol, leading to ISI between neighbour OFDM symbols.

The solution to this problem is to insert a CP at the beginning of every OFDM symbol as a guard interval, as shown in Figure 4.2.C. We can see from Figure 4.2.D that as long as the length of CP, t_{cp}, is larger than the channel delay spread t_d, there is no ISI between adjacent OFDM symbols. That is, the signal received in the i-th window depends only on the i-th transmitted symbol. Moreover, as shown in Figure 4.2.E, the signal received in the i-th window can be regarded as a convolution of the periodic summation of the i-th transmitted OFDM symbol with the channel IR. Thus, the signal received in a given window $y(t)$ can be written as:

$$y(t) = s_{T_s}(t) \odot h(t) \tag{4.9}$$

where $\odot$ is the circular convolution. Denoting that the samples of $y(t)$, $s(t)$ and $h(t)$ at intervals of T_s/N by y_k, x_k and h_k, $k = 0, 1, \ldots, N-1$, according to the circular convolution theorem, we have:

$$Y_k = H_k \cdot X_k \tag{4.10}$$

where Y_k, H_k and X_k are the DFTs of y_k, h_k and x_k, respectively. Thus, the transmitted data symbols $X(k)$ can simply be recovered as follows:

$$\hat{X}_k = \frac{Y_k}{H_k} \tag{4.11}$$

This one-tap channel equalization greatly simplifies the receiver structure compared with the case of SC modulation, which usually involves long-tap time domain equalization filters with high computational complexity.

4.3 OFDM for VLC

As stated previously, to apply to the VLC context, conventional OFDM signals must be made real and unipolar (positive). In this section, we review three commonly used OFDM schemes for optical systems: DCO-OFDM, ACO-OFDM, and PAM-DMT.

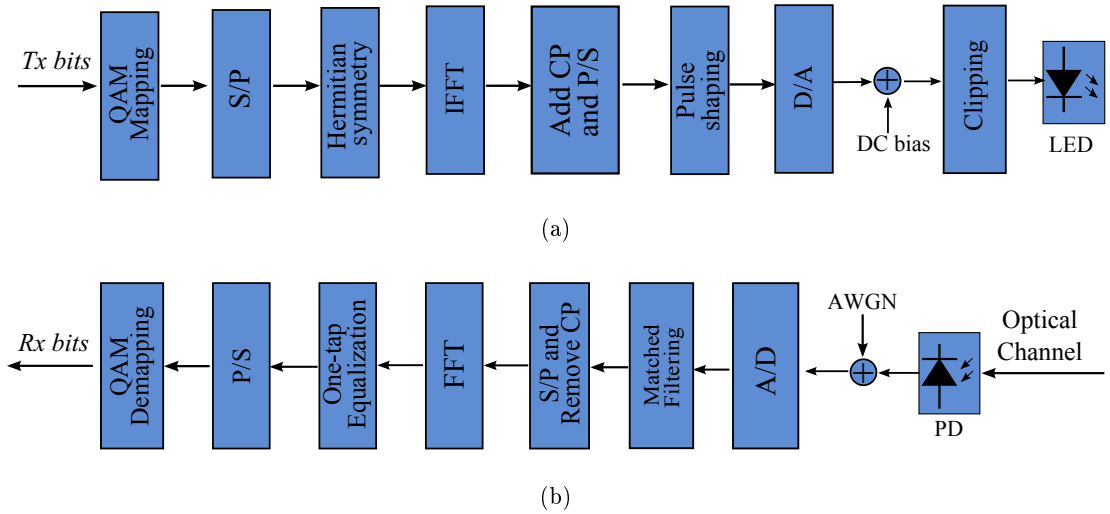

Figure 4.3 — General block diagram of DCO-OFDM (a) Transmitter (b) Receiver.

4.3.1 DCO-OFDM

As its name suggests, by DCO-OFDM, the signal is made unipolar by adding a DC bias current. The general block diagram is shown in Figure 4.3. At the transmitter, the data symbols X_k in the frequency domain after quadrature amplitude modulation (QAM) mapping is first organized into blocks by serial/parallel (S/P) conversion prior to passing through the IFFT block to form the time-domain signal x_n. In order to obtain a real signal after IFFT, the Hermitian symmetry is imposed on the k-th sub-carrier X_k (see Appendix C for proof), which is defined as:

$$\begin{cases} X_0 &= X_{N/2} = 0\,, \\ X_k &= X^*_{N-k}\,, \quad 0 < k < N/2 \end{cases} \tag{4.12}$$

where * denotes complex conjugation. A CP is then added to the beginning of each block serving as a guard interval. After digital pulse shaping and D/A, it is converted to an electrical current signal, to which a DC bias is added to obtain a non-negative signal. Then, the signal amplitude beyond the dynamic range of the LED is double-side clipped prior to feeding the LED to generate an optical signal. At the receiver, a PD is used to capture the optical signal and to regenerate an electrical signal. After matched filtering, A/D and S/P conversion, the CP of each block is first removed, and then a one-tap equalization is performed in the frequency domain to compensate the aggregate channel. Lastly, the transmitted information bits are recovered after parallel/serial (P/S)

conversion and symbol de-mapping.

Note that after adding a DC-bias, the DCO-OFDM signal has to be clipped from both sides (upper and lower bounds) in order to obtain a unipolar signal and to fit into the operation range of the LED. For a given clipping level k, the double-side clipped DCO-OFDM signal can be written as

$$x_{\text{clip}} = \begin{cases} k\sqrt{E\left[x^2(t)\right]}, & x(t) > k\sqrt{E\left[x^2(t)\right]} \\ x(t), & -k\sqrt{E\left[x^2(t)\right]} \leq x(t) \leq k\sqrt{E\left[x^2(t)\right]} \\ -k\sqrt{E\left[x^2(t)\right]}, & x(t) < -k\sqrt{E\left[x^2(t)\right]} \end{cases} \tag{4.13}$$

where $x(t)$ is the unclipped signal. The DC-bias current β_{DC} is therefore is set as

$$\beta_{\text{DC}} = k\sqrt{E\left[x^2(t)\right]}. \tag{4.14}$$

to obtain a unipolar signal. It is also convenient to define the so-called clipping factor κ as $\kappa = 10\log_{10}(k^2+1)$ since it denotes the total power increase in dB of the transmitted signal after adding the DC bias. The spectral efficiency η_{DCO} of an M-QAM mapped DCO-OFDM with an FFT size of N and a CP length of N_{cp} is

$$\eta_{\text{DCO}} = \frac{\log_2(M)(N-2)}{2(N+N_{\text{cp}})} \quad \text{bits/s/Hz}. \tag{4.15}$$

Remember from (4.12) that due to the Hermitian symmetry constraint, only $(N-2)/2$ sub-carriers are modulated.

4.3.2 ACO-OFDM

A disadvantage of DCO-OFDM system is the power efficiency penalty due to the added DC bias current. ACO-OFDM is a more power efficient scheme with the general diagram of the transmitter and receiver depicted in Figure 4.4. As we can see, the transceiver for ACO-OFDM is very similar to the DCO-OFDM case. The main difference is that the time-domain signal is made positive by loading information only on the odd sub-carriers and clipping entirely the negative signal amplitudes after IFFT. This clipping does not result in an information loss due to the anti-symmetry property of the time-domain ACO-OFDM signal. In fact, denoting $x_{k,n}$ as the contribution of the sub-carrier X_k at time n, we have

$$\begin{aligned} x_{k,n} &= \frac{1}{N}X_k \exp\left(j2\pi\frac{kn}{N}\right), \\ x_{k,n+N/2} &= \frac{1}{N}X_k \exp\left(j2\pi\frac{k(n+N/2)}{N}\right) = \frac{1}{N}X_k \exp\left(j2\pi\frac{kn}{N}\right)e^{j2\pi k}, \end{aligned} \tag{4.16}$$

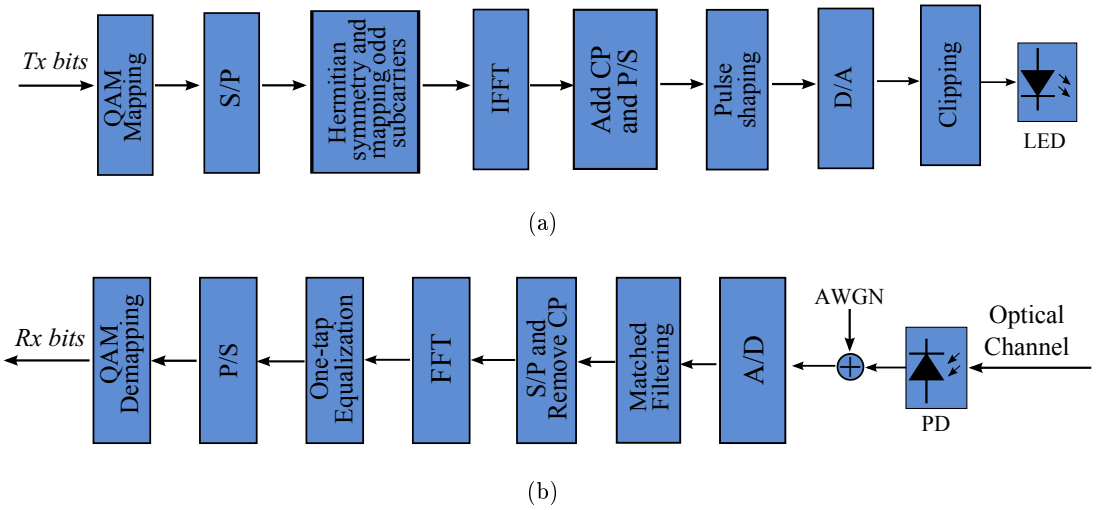

Figure 4.4 — General block diagram of ACO-OFDM (a) Transmitter (b) Receiver

which means that $x_{k,n} = -x_{k,\,n+N/2}$ for odd values of k. Thus, we have:

$$x_n = -x_{n+N/2} \tag{4.17}$$

if only the odd sub-carriers are modulated. This is what we called the anti-symmetry property of the time-domain signal. It can be shown that, in this way, the clipping distortion affects only the even sub-carriers in the frequency domain while for the odd sub-carriers, it results in only an attenuation factor of $1/2$ [51]. As a result, the signal can simply be demodulated by taking into account this attenuation factor at the receiver. In summary, ACO-OFDM does not need a DC bias to obtain a unipolar signal, compared to DCO-OFDM. Note that, however, the peak positive signal amplitudes will still be clipped if they exceed the maximum allowable LED current.

Given the unclipped signal $x(t)$ and the clipping level k, the ACO-OFDM signal after clipping can therefore be written as:

$$x_{\text{clip}} = \begin{cases} k\sqrt{E\left[x^2(t)\right]}, & x(t) > k\sqrt{E\left[x^2(t)\right]} \\ x(t), & 0 \leq x(t) \leq k\sqrt{E\left[x^2(t)\right]} \\ 0, & x(t) < 0 \end{cases} \tag{4.18}$$

As mentioned above, the advantage of ACO-OFDM over DCO-OFDM is its improved power efficiency [51], but its drawback is its lower spectral efficiency. In fact, since only odd sub-carriers are modulated, the spectral efficiency η_{ACO} is roughly half of η_{DCO} in

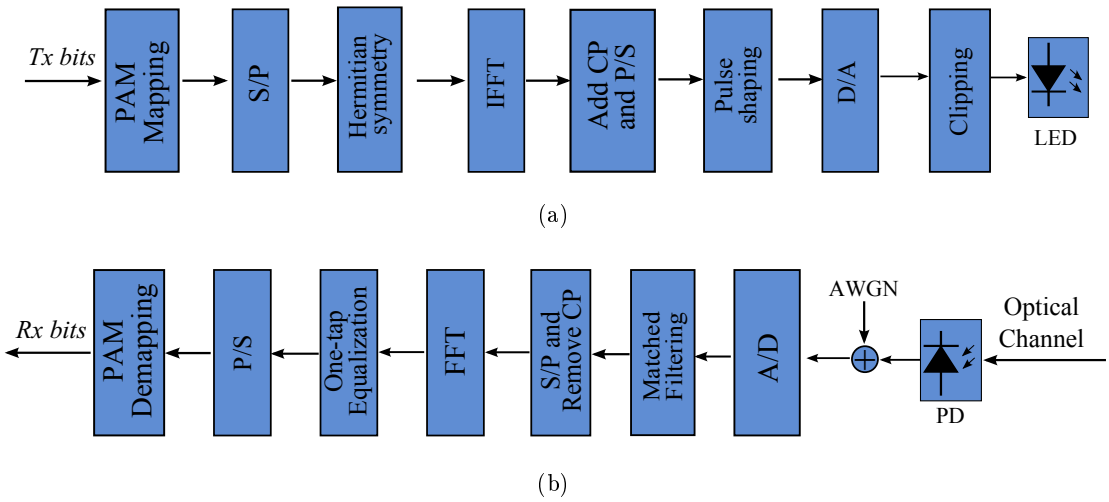

Figure 4.5 — General diagram of ACO-OFDM (a) Transmitter (b) Receiver

(4.15) as:

$$\eta_{\text{ACO}} = \frac{\log_2(M)N}{4(N+N_{\text{CP}})} \quad \text{bits/s/Hz.} \tag{4.19}$$

4.3.3 PAM-DMT

PAM-DMT is another unipolar transmission scheme in the VLC context where the general diagram is shown in Figure 4.5, which is very similar to the case of ACO-OFDM. The main difference with the latter scheme is that by PAM-DMT all sub-carriers are modulated, while the anti-symmetry property is satisfied by modulating with imaginary symbols from $M-$PAM. More specifically, the symbols in the frequency domain (*i.e.*, prior to IFFT) are set as follows:

$$\begin{cases} X_0 = X_{\frac{N}{2}} = 0 \\ X_k = jC_k, \quad 0 < k < \frac{N}{2} \\ X_k = -jC_{N-k}, \quad \frac{N}{2} < k < N \end{cases} \tag{4.20}$$

where $C_k, k = 1, 2, \ldots, \frac{N}{2} - 1$ corresponds to symbols from M-PAM mapping. Thus, the time-domain signal x_n is given by:

$$x_n = \frac{1}{N}\sum_{k=0}^{N-1} X_k \exp\left(j2\pi\frac{kn}{N}\right) = -\frac{2}{N}\sum_{k=1}^{\frac{N}{2}-1} C_k \sin\left(2\pi\frac{kn}{N}\right) \tag{4.21}$$

Therefore, we have the following anti-symmetry property:

$$x_{N-n} = -\frac{2}{N}\sum_{k=1}^{\frac{N}{2}-1} C_k \sin\left(2\pi\frac{k(N-n)}{N}\right) = \frac{2}{N}\sum_{k=1}^{\frac{N}{2}-1} C_k \sin\left(2\pi\frac{kn}{N}\right) = -x_n. \quad (4.22)$$

As a result, clipping the negative part does not lead to an information loss, as explained in Section 4.3.2, or in other words, we do not need to add a DC bias. The clipped PAM-DMT can be expressed by Equation (4.18) like for ACO-OFDM and its spectral efficiency $\eta_{\text{PAM-DMT}}$ for the case of M-PAM mapping is:

$$\eta_{\text{PAM-DMT}} = \frac{\log_2(M)(N-2)}{2(N+N_{\text{cp}})} \quad \text{bits/s/Hz}. \quad (4.23)$$

It is worth mentioning that the M-PAM mapped PAM-DMT has the same spectral efficiency as $\sqrt{M}$-QAM DCO-OFDM, and almost the same as M-QAM ACO-OFDM. The main interest of using PAM-DMT over ACO-OFDM is when using adaptive loading to maximize the link spectral efficiency. In fact, given that all sub-carriers are modulated with PAM-DMT scheme, the bit-power loading can be done in a more optimized way [54].

4.3.4 PAPR issue

As stated previously, the main drawback of the optical OFDM schemes is their potential high PAPR. It originates from the fact that the superposition of multiple sub-carriers (sinusoids) results in the occurrence of high peak magnitudes while the average signal power can be quite low due to destructive interference between the sinusoids. A high PAPR is very disadvantageous as it requires a large linear dynamic operation range of the optical front-ends, *e.g.*, LED, which results in a degradation of the system power efficiency. The PAPR ζ of a signal $s(t)$ is defined as the ratio between the maximum instantaneous power and the average power and can be expressed as:

$$\zeta = \text{PAPR}\{s\} = \frac{\max\left[s(t)s^*(t)\right]}{E\left[s(t)s^*(t)\right]}. \quad (4.24)$$

In fact, the PAPR can be regarded as a random variable (RV) and the common approach to characterize it is to consider the probability P_c that the PAPR exceeds a particular value ζ_0:

$$P_c = \Pr\left(\zeta > \zeta_0\right). \quad (4.25)$$

which is in fact the complementary comcumulative distribution function (CCDF) of the PAPR. We have shown in Figure 4.6 the CCDFs of the PAPR of 16-PAM PAM-DMT, 16-QAM DCO-OFDM and 256-QAM ACO-OFDM for the same spectral efficiency with

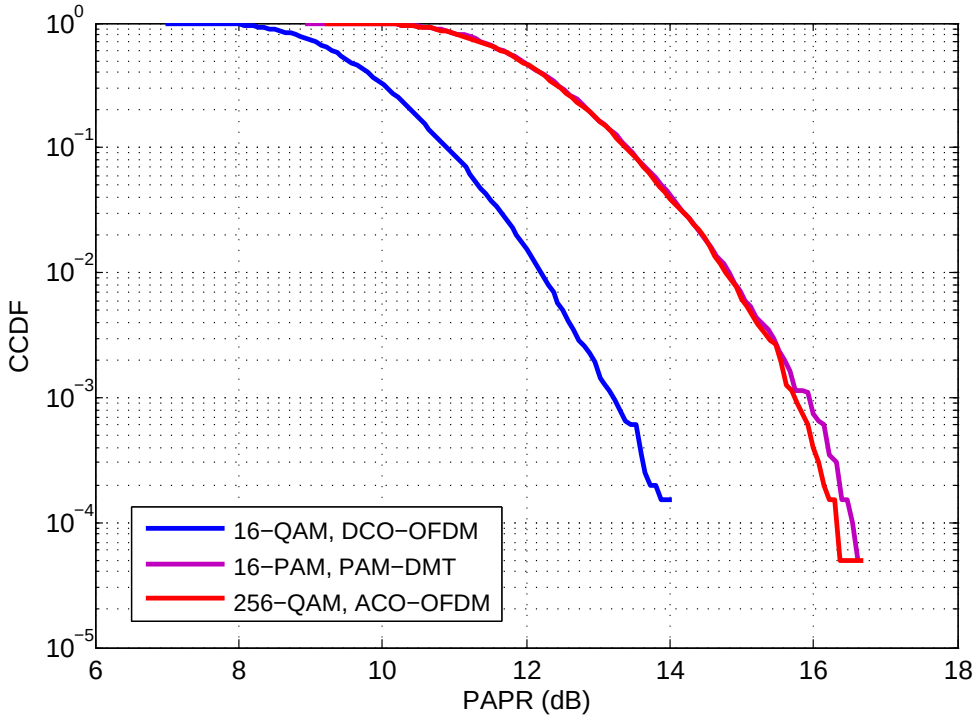

Figure 4.6 — CCDF of PAPR for 16-PAM PAM-DMT, 16-QAM DCO-OFDM and 256-QAM ACO-OFDM, $N = 256$, $N_{\text{cp}} = 12$

an FFT size of 256. We notice that the PAPR performance of ACO-OFDM and PAM-DMT are approximately the same for the same spectral efficiency while DCO-OFDM has the lowest PAPR. The reason is that to achieve the same spectral efficiency, DCO-OFDM needs the smallest constellation size. Nevertheless, we notice that the PAPR of 16-QAM DCO-OFDM at a CCDF of 10^{-2} is about 12 dB. That means that the peak power is one order of magnitude larger than the average power, which is still very high.

4.3.5 Clipping effect

The nature way to limit the signal PAPR is to perform clipping, but this results in signal distortion, which is usually modelled by a so-called clipping noise. In fact, for OFDM-based schemes, the time domain signal after IFFT can be considered as a Gaussian independent and identically distributed (i.i.d.) RV when the number of sub-carriers N is roughly larger than 64, according to the central limit theorem (CLT). Then, the clipping effect on the time-domain OFDM signal can be modelled as an attenuation factor plus

a non-Gaussian noise (almost uncorrelated with the signal clipping) using the Bussgang theorem [56,57], that is

$$x_{\text{clip}} = \alpha x + n_c \tag{4.26}$$

where α is the attenuation factor, and n_c is the clipping noise component where we have $E[xn_c] = 0$. After FFT at the receiver, this time-domain non-Gaussian noise is converted to the frequency domain and the resulting clipping noise on each sub-carrier Z_c can be modelled by a Gaussian distribution, again according to the CLT. Overall, the clipping effect on each sub-carrier for OFDM-based schemes can be modelled as an attenuation factor α of the signal power plus an uncorrelated Gaussian noise Z_c.

4.4 Numerical Results

After presenting the principles of the commonly-used optical OFDM schemes for VLC systems, we present in this section a set of simulation results to investigate their suitability for achieving high data-rate transmission by taking into account the clipping effect and the frequency response of the LED. Given the potentially high PAPR of ACO-OFDM and PAM-DMT schemes, here, we limit our study to the case of DCO-OFDM. Indeed, for the same reason, most of reported experimental set-ups in the literature have chosen DCO-OFDM [14,23] to achieve high data-rate transmission. Note that, the comparison between DCO-OFDM and the two other schemes is a well investigated subject for the case of an AWGN channel. We do not consider adaptive bit-power loading in our study either due to the difficulty of integrating the clipping noise into the existing adaptive loading algorithms, which we have explained in Appendix D.

4.4.1 Simulation parameters

We consider a linear transfer function for the LED whose input current is constrained in the interval $[i_{\min}, i_{\max}]$, where we set $i_{\min} = 0.1$ A and $i_{\max} = 1$ A. The response of the LED is modelled as a first-order low pass filter as we described in Section 2.2.2 with a 3-dB bandwidth of 20 MHz (the use of a blue filter is assumed). The indoor VLC channel is considered as flat assuming that we are not in the diffuse propagation mode, see Chapter 3. In other words, in order to focus on the bandwidth limitation of the LED, we model the indoor VLC channel as:

$$h_{\text{VLC}}(t) = \eta\, \delta(t - \Delta t) \tag{4.27}$$

where $\delta(t)$ is the Dirac delta function, Δt is the time delay of the LOS path, and $\eta = 10^{-4}$ is the LOS channel loss. Double-side clipping is considered for DCO-OFDM as described in (4.13) for a given clipping level. It is worth mentioning that if the signal amplitude after this clipping still falls outside the operation range of the LED, it will be further clipped to avoid overheating the LED. The FFT size N, the CP length N_{cp} and the total signal bandwidth are set to 256, 12 and 100 MHz, respectively. The pulse shaping filter is chosen to be a raised-cosine filter (RCF) with an up-sampling factor of 5 and a length of 16 symbols. Pilot sequences are used to estimate the aggregate channel, *i.e.*, the optical channel plus the LED response, and the signal is equalized in the frequency domain by using a one-tap zero-forcing (ZF) equalizer. Note that in typical indoor VLC scenarios, we benefit from a relatively high SNR that justifies the use of a simple ZF equalizer. The main simulation parameters are summarized in Table 4.1. We evaluate

Table 4.1 — Simulation parameters for DCO-OFDM

Parameter		Value
LED	Operation range	[0.1, 1] A
	3-dB bandwidth	20 MHz
DCO-OFDM modulation	FFT size	256
	CP length	12
VLC channel	Type	Flat channel
	LOS gain	10^{-4}
Pulse shaping filter	Type	Raised cosine filter
	Upsampling factor	5
	Filter span	16

the link performance in terms of BER as a function of the *electrical* SNR. Note that due to the clipping noise, it is not convenient to fix the SNR at the receiver. For this reason, we evaluate the BER performance as a function of the electrical SNR at the transmitter that we denote by $E_{b,\text{elec}}/N_0$, where $E_{b,\text{elec}}$ is the electrical energy per bit at the transmitter, and N_0 is the one-side noise power spectral density which is set to $N_0 = 10^{-21}$ W/Hz according to [30]. Otherwise, this SNR can be brought to the receiver side by multiplying it by η^2, but this will not be the "real" SNR as it does not take the signal clipping into account. Note that several related works, *e.g.* [58], have also evaluated the system performance in term of SNR at the transmitter.

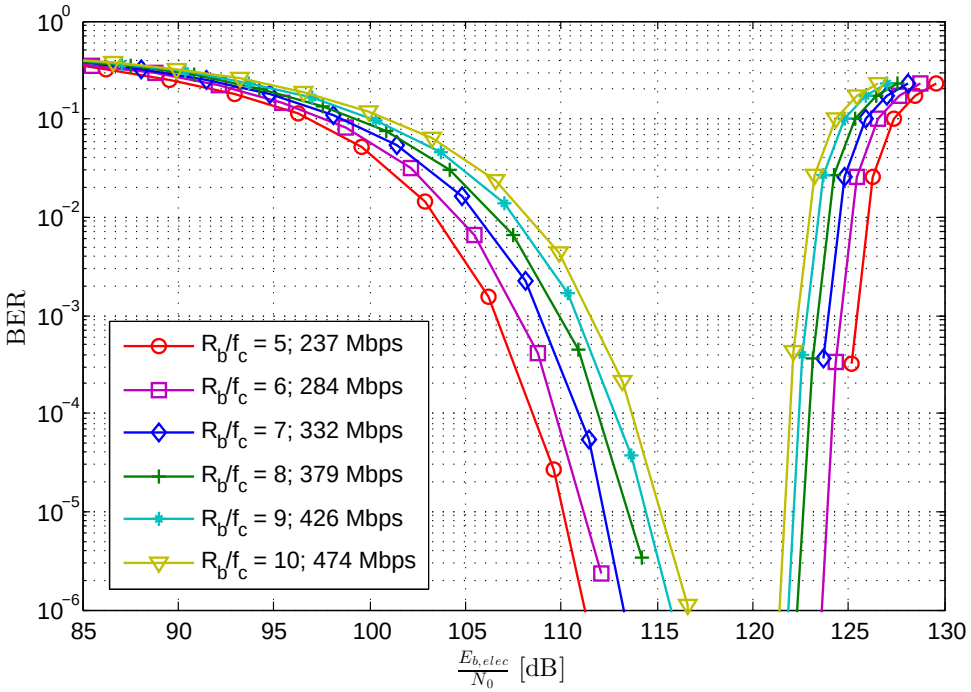

Figure 4.7 — BER performance of 32-QAM DCO-OFDM versus the electrical SNR at the transmitter for different R_b/f_c (data rates), the clipping factor is set to $\kappa = 10$ dB.

4.4.2 BER performance for different signal bandwidths

It is interesting to firstly investigate the merit of using DCO-OFDM to achieve high data-rate transmission. For convenience, we denote the metric R_b/f_c as the ratio between the signal bandwidth R_b and the 3-dB bandwidth of the LED f_c. We consider a clipping factor of $\kappa = 10$ dB to ensure a relatively low clipping noise. The BER results of 32-QAM DCO-OFDM as a function of $E_{b,\,\mathrm{elec}}/N_0$ for different R_b/f_c factors are shown in Figure 4.7. The BER first decreases with the increase in the electrical SNR at the transmitter. Then after passing a certain threshold, the signal amplitude falls more and more outside the operation range of the LED, resulting in the increase of the clipping noise and consequently very high BERs (roughtly for E_b/N_0 larger than 120 dB). Meanwhile, we notice the ability of DCO-OFDM to ensure very high data rates well above the 3-dB bandwidth of the LED, *e.g.*, 474 Mbps for $R_b/f_c = 10$, while using a simple ZF equalizer at the receiver.

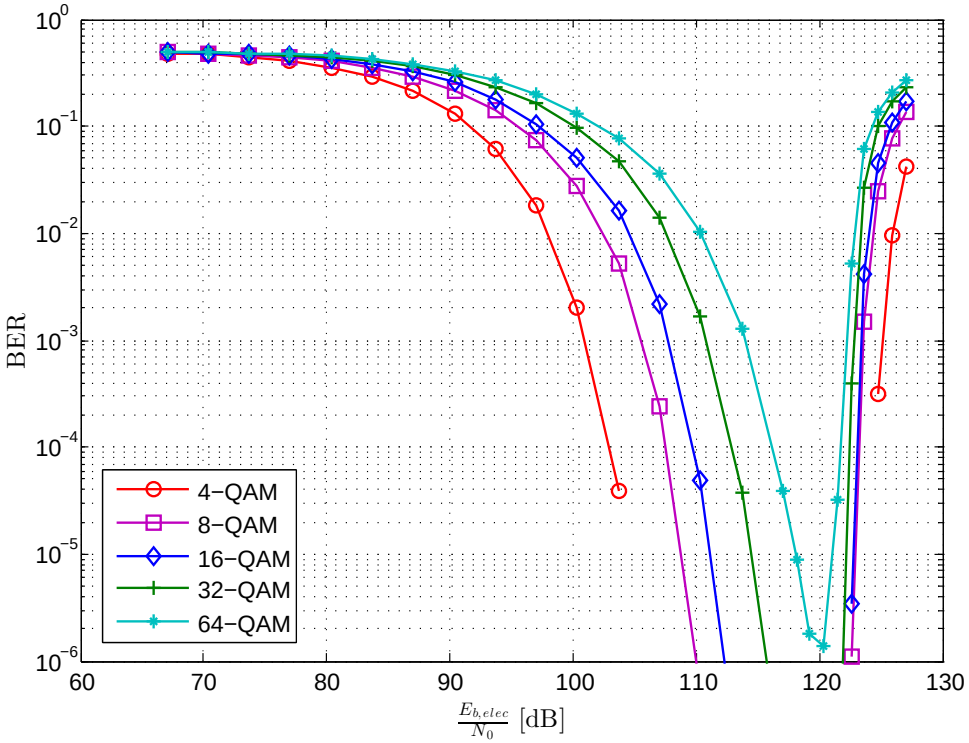

Figure 4.8 — BER performance of DCO-OFDM versus electrical SNR at the transmitter for different modulation orders, $\kappa = 10$ dB and $R_b/f_c = 10$ in this case.

4.4.3 BER performance for different constellation sizes

Figure 4.8 shows the BER performance of DCO-OFDM against the electrical SNR at the transmitter for different signal constellation sizes. Remember that here we use the same constellation size for all sub-channels. The clipping factor is set to $\kappa = 10$ dB and R_b/f_c is set to 10 in this case. As expected, with increased modulation order and consequently the PAPR, the performance is more affected by the clipping noise.

4.4.4 BER performance for different clipping factors

A large clipping factor results in less signal distortion arising from the clipping effect, but at the same time, it necessitates a larger DC-bias current according to (4.13), and hence, involves a higher power consumption at the transmitter. To investigate the impact of the clipping factor, we have presented the BER results for 32-QAM DCO-OFDM for the clipping factors of 7, 10 and 13 dB in Figure 4.9. We notice that at low SNR

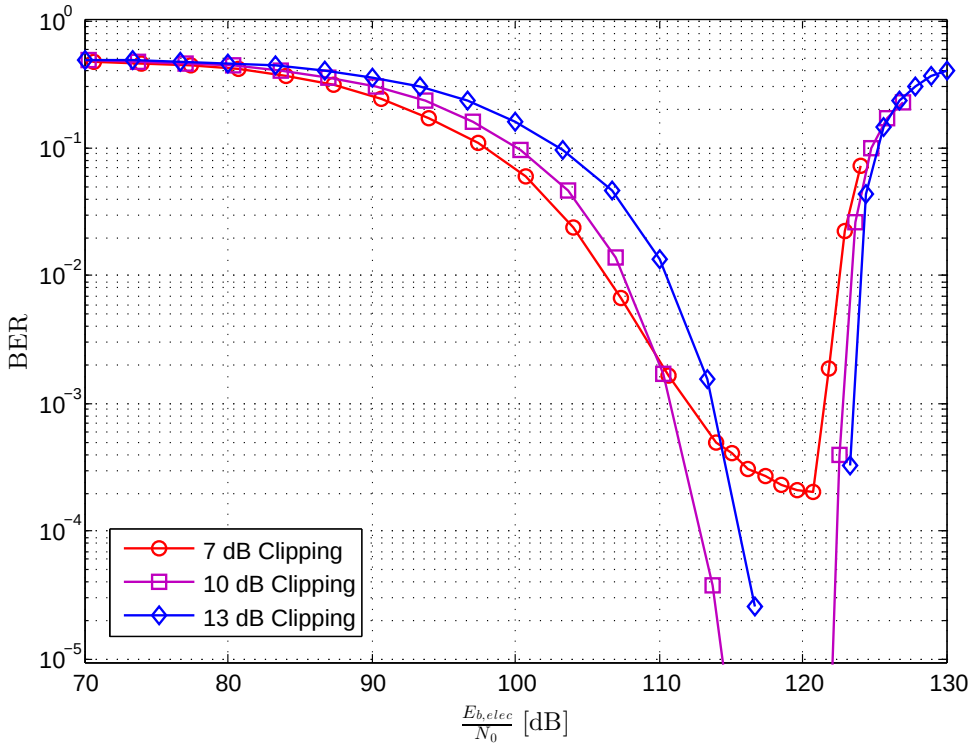

Figure 4.9 — BER performance of 32-QAM DCO-OFDM versus electrical SNR at the transmitter for different clipping factors κ, $R_b/f_c = 10$.

region, where the receiver Gaussian noise dominates the clipping noise, the case of $\kappa = 7$ dB has the best performance. Then, after passing a certain value, those with larger clipping factors exhibit a better performance. Indeed, with increased transmit power, the clipping noise becomes more and more important until it dominates the Gaussian noise, and consequently we notice a degraded performance, as compared with higher κ values. At low SNR region, we observe that the transmission of 7 dB clipping has the best performance. Then after passing a certain value, those with large clipping factors exhibit the better performance. The reason is that the Gaussian noise dominates the system performance for low SNR region. While at high SNR region, the clipping noise caused by the high PAPR begins to surpass the Gaussian noise, thus, resulting in a poor performance for the cases of relatively small clipping factors.

4.5 Chapter summary

In this chapter, we first reviewed the basic principles of OFDM signaling, and then introduced three commonly used optical OFDM schemes for VLC systems, *i.e.*, DCO-OFDM, ACO-OFDM, and PAM-DMT. Given the higher PAPR penalty for ACO-OFDM and PAM-DMT, we focused on the DCO-OFDM scheme and investigated its performance at the aim of achieving high data rate transmission by taking into account the frequency response of the LED and the clipping effect. By studying its BER for different signal bandwidths and constellation sizes, we demonstrated its merits in overcoming the limited modulation bandwidth of the LED and discussed the impact of the clipping noise on the overall system performance. Note that in the presented results, we did not consider any bit-power loading due to the difficulty of setting the target BER which is affected by clipping noise (see Appendix D). As we explained in this chapter, optical OFDM schemes suffer from a potentially high PAPR, in particular for increased constellation size and data rate (*i.e.*, R_b/f_c factor). For this reason, we are going to propose a more appropriate alternative solution for the indoor VLC context in the next chapter.

CHAPTER 5

CAP-FDE for VLC

5.1 Introduction

As stated in the previous chapter, the main drawback of optical OFDM schemes is their relatively high PAPR compared to single-carrier modulations. A high PAPR is very disadvantageous in VLC systems for two reasons: Firstly, it decreases the transmitter power efficiency as we need a relatively large DC bias to obtain a positive signal. Secondly, it requires a large dynamic range of the optical front-ends, *e.g.*, the LED. In fact, most of available commercial LEDs have a limited operation range as we explained in Section 2.2.3. The signal amplitude beyond this range has to be clipped, which could result in severe non-linear distortion [59].

SC modulation has been the traditional digital communication format before the emergence of multi-carrier systems. It has the advantages of a lower PAPR and robustness to frequency and phase noise [60], compared with its multi-carrier modulation counterparts, *e.g.*, OFDM. To deal with channel frequency selectivity, the conventional solution in the case of SC modulation is to use a time-domain equalization filter at the receiver. However, this approach becomes unfavourable and leads to high receiver computational complexity when the channel has a large delay spread, *i.e.*, highly frequency selective. A promising alternative approach is to perform the channel equalization in the frequency domain. When this is based on FFT and IFFT calculation, the corresponding computational complexity becomes much lower compared with the conventional time-domain equalization. This way, by transmitting the symbols block-wise and inserting a CP at the beginning of every block, the inter-block interference can be removed and the equalization in the frequency domain can be easily done using a one-tap equalizer, as we explained for OFDM-based schemes [45], thus reducing considerably the receiver complexity. The resulting single-carrer frequency domain equalization (SC-FDE), has essentially the same performance and complexity as OFDM-based transmission [61, 62],

but in addition, it benefits from a relatively low PAPR due to its inherent SC nature. The concept of SC-FDE has been applied to a number of communication systems [62–65] and has been adopted in various communication standards such as the uplink of the Long-Term Evolution (LTE) cellular networks. The adaptation of SC-FDE to VLC systems using IM/DD modulation has also been recently introduced as an alternative to OFDM-based signaling [45,66–69].

Carrier-less amplitude phase modulation (CAP), a variant of SC modulation, had been used in several rather old communication systems such as High-bit-rate digital subscriber line (HDSL). It had been also considered as an option for asymmetric digital subscriber line (ADSL) transmission [70] before being withdrawn in favour of DMT in 1990s. In contrast to other SC schemes, CAP does not rely on any sinusoidal oscillator for signal generation. Instead, two digital orthogonal finite impulse response (FIR) filters are employed to modulate the data in two dimensions, resulting in a relatively simple and low-cost system. Recently, CAP has been revisited and applied to VLC systems due to its advantages of higher spectral efficiency and lower PAPR [71–74]. Data rates up to Gbps has been demonstrated in [75] on a single white LED for relatively short-range links (about 30 cm). However, as a SC scheme, CAP may lose its interest in the case of highly dispersive channels due to the need to channel equalization at the receiver. Inspired by the idea behind FDE, we propose here to use CAP modulation together with FDE at the receiver for VLC systems. This scheme inherits both the advantages of CAP and FDE, *i.e.*, high spectral efficiency, low PAPR and low complexity equalization at the receiver. Moreover, we propose to perform the equalization and matched filtering at once in the frequency domain, hence, reducing further the receiver computational complexity.

The general aim of this chapter is therefore to investigate the merits of using this proposed CAP-FDE scheme in the VLC context. The remainder of this chapter is organized as follows: In Section 5.2, we present the principles of the CAP-FDE scheme by explaining separately the CAP modulation and the receiver using FDE. In Section 5.4, we compare its performance with its optical OFDM counterpart, *i.e.*, DCO-OFDM in terms of power and spectral efficiency, and PAPR performance. Then, in Section 5.5, we present some numerical results to investigate its BER performance by taking into account the clipping effect and the frequency response of the LED. Lastly, we summarize this chapter in Section 5.5.

5.2 Principle of CAP-FDE

In this section, we present the principle of the CAP modulation and the receiver with FDE.

5.2.1 CAP modulation

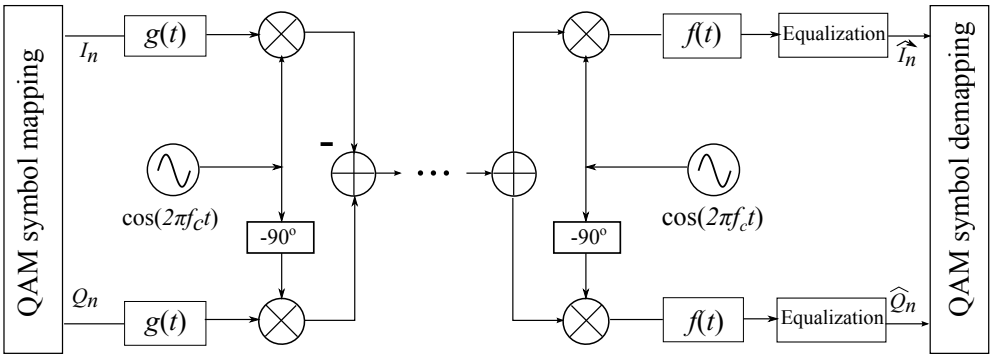

Figure 5.1 — Block diagram of Nyquist-SCM transceiver, f_c is the carrier frequency, $g(t)$ and $f(t)$ are the baseband pulse shaping filter, and its MF

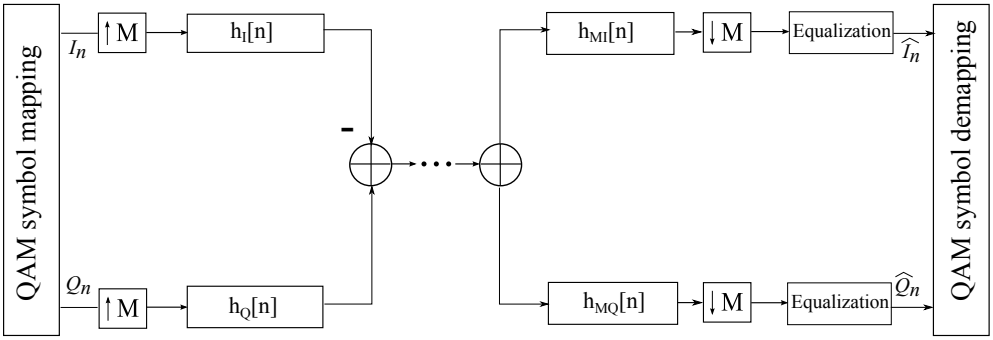

Figure 5.2 — Block diagram of conventional CAP transceiver, M is the up-sampling factor, $h_I[n]$ and $h_Q[n]$ are the digital in-phase and quadrature shaping filters, and $h_{MI}[n]$ and $h_{MQ}[n]$ are the corresponding MFs

CAP is a multi-level single-carrier modulation scheme. The word "carrier-less" in its name does not mean that CAP is a baseband modulation, but rather signifies that it does not need any analog *oscillators* for signal generation.

The transmitter of CAP is very similar to that of the so-called Nyquist pulse-shaped single-carrier modulation (SCM) [76], but has a big implementation difference, which

is illustrated in the transceiver block diagrams in Figures 5.1 and 5.2. Whilst by the classical Nyquist pulse-shaped SCM, the carrier frequency is generated by an analog oscillator, by CAP modulation, it is implicitly realized in the digital domain through two digital filters.

Consider the block diagram in Figure 5.2, at the transmitter, the signal after QAM mapping and inphase/quadrature (I/Q) separation is firstly up-sampled by a factor M before being filtered by two digital pulse shaping filters. Up-sampling is realized by inserting $(M-1)$ zeros between consecutive symbols. The two shaping digital filters, *i.e.*, $h_I[n]$ and $h_Q[n]$, are obtained from their corresponding analog equivalents $h_I(t)$ and $h_Q(t)$, which are related through the Hilbert transform [77]:

$$h_{\mathrm{I}}(t) = g(t) \cdot \cos(2\pi f_c t), \quad h_{\mathrm{Q}}(t) = g(t) \cdot \sin(2\pi f_c t). \tag{5.1}$$

where f_c is the carrier frequency and $g(t)$ is the IR of the baseband shaping filter, which is usually a root-raised-cosine filter (RRCF); also known as squared-root-raised-cosine filter (SRRC). Then, the subtraction of the two I and Q digital outputs is converted to an analog signal by passing through a D/A. Given a symbol duration T_s, the digital filters and D/A should work at the rate of M/T_s to match the rate of the input symbols after up-sampling [78]. The generated analog CAP signal can hence be written as

$$s(t) = \sum_{n=-\infty}^{\infty} I_n \cdot h_{\mathrm{I}}(t - nT_s) - Q_n \cdot h_{\mathrm{Q}}(t - nT_s), \tag{5.2}$$

where I_n and Q_n are the corresponding in-phase and quadrature symbols after QAM mapping. Correspondingly, at the receiver, the signal is first digitized by an A/D and then is filtered by two corresponding digital MFs, h_{MI} and h_{MQ}, whose analog IR are defined as

$$h_{\mathrm{MI}}(t) = f(t) \cdot \cos(2\pi f_c t), \quad h_{\mathrm{MQ}}(t) = f(t) \cdot \sin(2\pi f_c t). \tag{5.3}$$

where $f(t)$ is the MF of the baseband shaping filter $g(t)$. Then, after down-sampling by a factor M, QAM de-mapping is done to recover the transmitted information.

Condition of zero interference

For the case of CAP modulation, it is very important to have zero interference, or in other words, zero cross-talk, between the I and Q components after matched filtering at the receiver. Since pulse shaping and matched filtering are implemented in the digital domain, the following condition should be satisfied at the sampling points kT_s to have

zero interference between the I and Q signals:

$$h_{\mathrm{IQ}}(kT_s) = 0, \quad h_{\mathrm{QI}}(kT_s) = 0 \tag{5.4}$$

where $h_{\mathrm{IQ}}(t) = h_{\mathrm{I}}(t) \otimes h_{\mathrm{MQ}}(t)$ and $h_{\mathrm{QI}}(t) = h_{\mathrm{Q}}(t) \otimes h_{\mathrm{MI}}(t)$. Furthermore, to avoid ISI between adjacent symbols of the I and Q components, we should also have:

$$h_{\mathrm{II}}(kT_s) = h_{\mathrm{QQ}}(kT_s) = \begin{cases} 1; & k = 0 \\ 0; & k \neq 0 \end{cases} \tag{5.5}$$

where $h_{\mathrm{II}}(t) = h_{\mathrm{I}}(t) \otimes h_{\mathrm{MI}}(t)$ and $h_{\mathrm{QQ}}(t) = h_{\mathrm{Q}}(t) \otimes h_{\mathrm{MQ}}(t)$. The solution for (5.5) is to choose a shaping filters that satisfies the Nyquist criterion defined as:

$$h(kT_s) = \begin{cases} 1; & k = 0 \\ 0; & k \neq 0 \end{cases} \tag{5.6}$$

where $h(t) = g(t) \otimes f(t)$. Moreover, if the carrier frequency f_c is chosen such that $f_c \geq B$ with B being the bandwidth of the low pass baseband filters $f(t)$ and $g(t)$, the zero interference condition between the I and Q components described in (5.4) will also be guaranteed (detailed demonstration is provided in Appendix E).

Theoretically, the most bandwidth efficient Nyquist filter for $h(t)$ is the Sinc filter, whose spectrum has a rectangular shape. However, the IR of the Sinc filter has an infinite duration in the time domain, making it unfeasible for digital implementation. A practical choice for $h(t)$ is the RCF, which has a adjustable bandwidth in $[-\frac{1}{2T_s}(1+\alpha), \frac{1}{2T_s}(1+\alpha)]$ where $0 < \alpha \leq 1$ is the roll-off factor. Correspondingly, the shaping filter $g(t)$ at the transmitter and the MF $f(t)$ at the receiver are a RRCF filter and the carrier frequency is set to:

$$f_c = \frac{1}{2T_s}(1+\alpha). \tag{5.7}$$

Figure 5.3 illustrates an example of the auto-correlations and cross-correlations between the I and Q shaping filters and their MFs, from which we can clearly see the zero interference at every sampling time kT_s.

5.2.2 FDE-based receiver

As explained in the introduction, the use of FDE at the receiver can greatly reduce the equalization complexity. However, to cope the CAP modulation with FDE, the conventional CAP transmitter has to be modified accordingly. The first point is to do block transmission, this is, to arrange the data symbols at the transmitter into blocks of

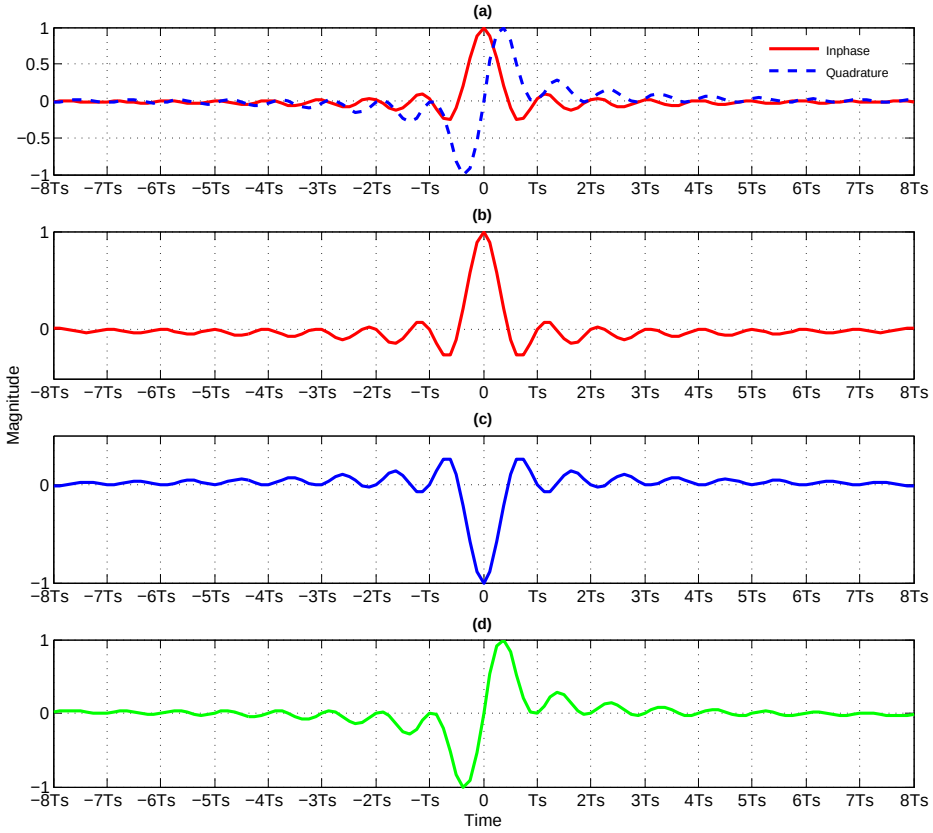

Figure 5.3 — Impulse response of (a) Inphase and quadrature shaping filters (b) $h_{\mathrm{II}}(t)$ (c) $h_{\mathrm{QQ}}(t)$ (d) $h_{\mathrm{IQ}}(t)$, RRCFs with $\alpha = 0.1$

length N. Then, a CP is added to the beginning of the every block as we do for OFDM-based schemes. In this way, the linear convolution between the transmitted frame and the aggregate channel IR becomes a circular convolution and an entire block of data symbols can be equalized at once in the frequency domain using a simple one-tap equalizer. For this, an FFT is done at the receiver after removing the CP. After equalization, an IFFT is used to convert the equalized signal to time-domain prior to signal de-mapping.

As we can see from Figure 5.2, for conventional CAP receivers, the signal must be filtered by two digital MFs to separate the I and Q components prior to down-sampling and equalization. Generally, matched filtering is realized in the time-domain by linear convolution, which needs extra computational resources. Here, we propose to do it in the frequency domain together with the one-tap equalization to further reduce the com-

putational complexity. Let us consider the signal after matched filtering for conventional CAP receivers that we denote by $r_m[n]$, we have:

$$\begin{aligned} r_m[n] &= s[n] \otimes h_{\mathrm{MI}}[n] + j \cdot s[n] \otimes h_{\mathrm{MQ}}[n] \\ &= s[n] \otimes h_{\mathrm{M}}[n] \end{aligned} \tag{5.8}$$

where $s[n]$ is the received signal, $j = \sqrt{-1}$ and we have defined $h_{\mathrm{M}}[n] = \{h_{\mathrm{MI}}[n] + j \cdot h_{\mathrm{MQ}}[n]\}$ as the aggregate complex MF that combines the MFs of the I and Q paths. Therefore, the two-step in-phase and quadrature matched filtering can be realized at once by multiplying the transfer function $H_{\mathrm{M}}[k] = \mathrm{FFT}\{h_{\mathrm{M}}[n]\}$ in the frequency domain. Moreover, suppose that the IR of the linear dispersive channel is $h_c[n]$, a simple one-tap equalizer is equivalent to multiplying the inverse of the channel $1/H_c[k]$ where $H_c[k]$ is the transfer function (*i.e.*, FFT) of $h_c[n]$ in the frequency domain. Thus, both matched filtering and FDE can be done in one step by multiplying an equivalent aggregate filter $H_{\mathrm{eq}}[k]$ in the frequency domain such that

$$H_{\mathrm{eq}}[k] = H_{\mathrm{M}}[k]/H_c[k]. \tag{5.9}$$

The overall block diagram of CAP-FDE signaling scheme is shown in Figure 5.4. At the transmitter, the information bits are first mapped into complex symbols using QAM mapping, which are then grouped into blocks of size N. A CP of length L is added at the beginning of each block. After I/Q separation, an up-sampling of factor M is performed prior to I and Q pulse shaping filters. The subtraction of the I and Q signals is then passed through a D/A to which a DC bias is added prior to intensity modulation of the LED. At the receiver, a PD is used to generate an electrical signal according to the received optical intensity. The generated analog electrical current is then converted to digital domain by an A/D. After removing the CP, matched filtering and one-tap equalization is performed at once in the frequency domain by multiplying the equivalent filter H_{eq} in (5.9). An IFFT operation is applied afterwards to convert the signal to the time domain prior to down-sampling and QAM demapping.

Comparing Figures 5.2 and 5.4, we can see that the two separate steps of I and Q matched filtering and equalization in the conventional CAP receiver are realized by a pair of IFFT/FFT operation plus a simple single-tap FDE in the proposed CAP-FDE scheme. This allows a significant reduction of the receiver computational complexity.

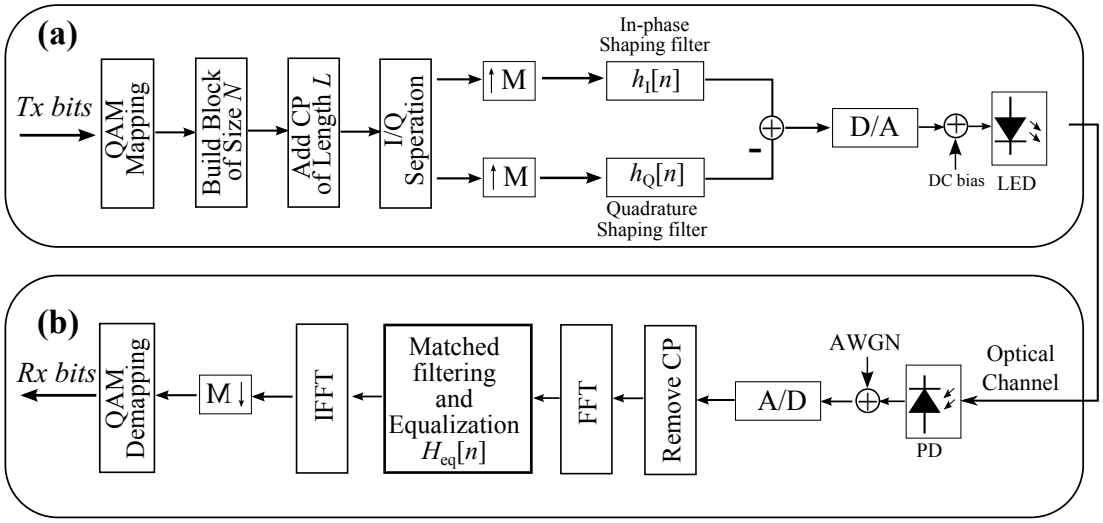

Figure 5.4 — General block diagram of (a) transmitter of (b) receiver of the CAP-FDE scheme

5.3 Multi-band CAP

A so-called multi-band CAP scheme has also been proposed in [73, 79] to overcome the limited modulation bandwidth of the LED for VLC systems. This scheme is in fact a multi-carrier transmission which divides the total signal bandwidth into a number of sub-channels, with each sub-channel being modulated by a conventional CAP, as shown in Figure 5.5. In this way, each sub-channel can be considered almost flat and can be equalized with low complexity at the receiver. In addition, adaptive loading can be used to maximize the channel capacity as for the OFDM-based schemes. However, a disadvantage of this scheme is its high computational complexity in both signal generation at the transmitter and matched filtering at the receiver. In fact, an m sub-band multi-CAP transmission involves the use of $2m$ pulse shaping filters and $2m$ matched filters. Moreover, being inherently a multi-carrier transmission scheme, it exhibits a higher PAPR than the conventional CAP, which can result in severe signal distortion due to clipping, as discussed previously. Nevertheless, owing to its high spectral efficiency, this scheme is still of great interest for VLC systems to achieve high data-rate transmission and spectral efficiencies of up to 4.85 bits/s/Hz have been reported in [73, 79]. Note however that if no bit-power loading is performed, multi-band CAP has no advantage over CAP in terms of spectral efficiency. The study of multi-band CAP is out of the scope of this thesis but a potential interesting research is to find solutions to reduce its computational

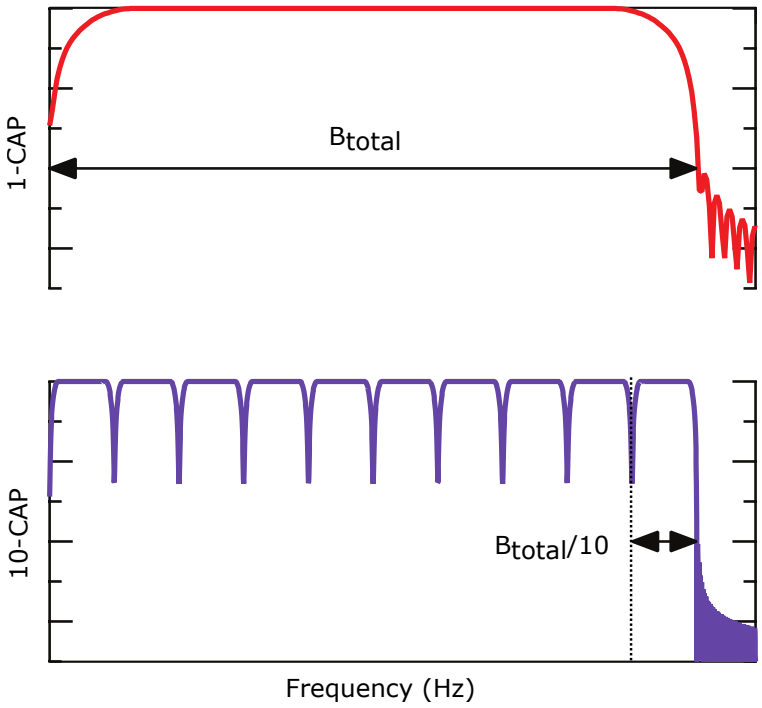

Figure 5.5 — Spectrum of a conventional CAP and a 10 sub-band multi-CAP transmission, B_{total} is the total system bandwidth, reproduced from [73].

complexity. We have presented a possible solution for this problem, *i.e.*, how to generate the multi-CAP signal at the transmitter with reduced complexity, in Appendix F.

5.4 Comparison of CAP-FDE with optical OFDM

Having presented the principles of CAP-FDE transmission scheme for VLC systems, in this section, we compare it with the optical OFDM schemes that we described in the previous chapter and discuss its pros and cons in terms of spectral and power efficiency, and PAPR performance.

Power efficiency

Since the generated CAP signal is a bipolar signal, a DC bias should be added to it to obtain a positive signal prior to intensity modulation of the LED. Thus, the optical/electrical power efficiency of CAP-FDE is approximately the same as that of DCO-

OFDM, which is lower than those of unipolar optical OFDM schemes, *e.g.*, ACO-OFDM and PAM-DMT.

Spectral efficiency

According to (5.7), the bandwidth of the CAP signal depends on the roll-off factor of the baseband RRCF shaping filters. For instance, for a roll-off factor of $\alpha = 0.1$ and a symbol rate of $1/T_s$, the spectrum of the CAP signal is showed in Figure 5.6. The bandwidth of

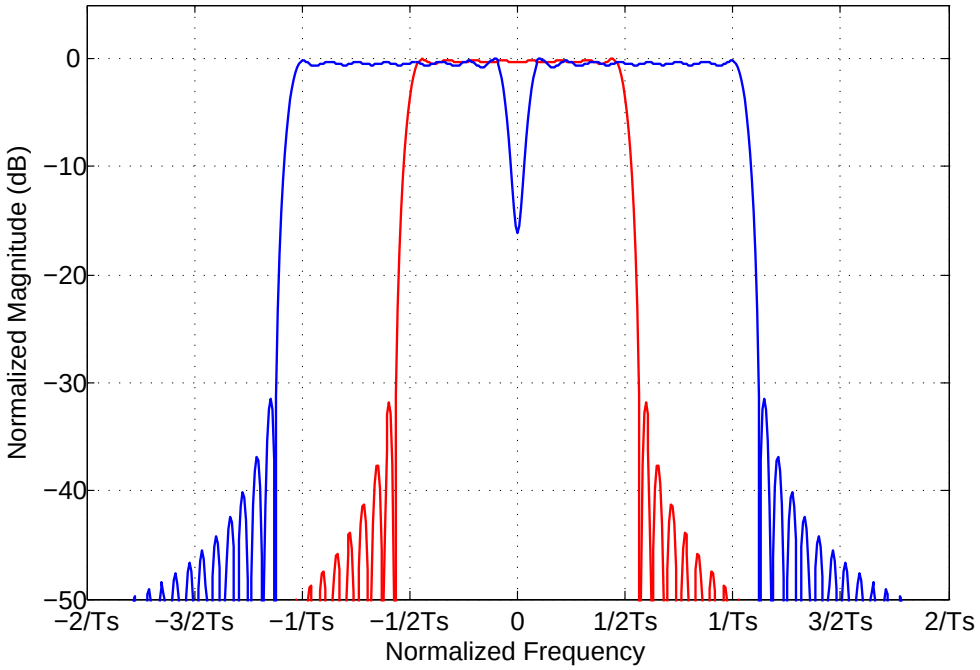

Figure 5.6 — Spectrum of CAP (blue line) and basedband RRCF shaping filters (red line)

the CAP signal is $(1+\alpha)\frac{2}{T_s}$, which is twice the bandwidth of the baseband RRCF shaping filter. Note that pulse shaping is also necessary for optical OFDM schemes, where we could assume the same baseband pulse shaping filters. So, to simplify the problem and in order to compare the the spectral efficiencies of CAP and optical OFDM, we ignore the excess bandwidth due to the roll-off factor. As a result, we can write the spectral efficiency of an M-CAP scheme with a block size of N and a CP of length N_{cp} by:

$$\eta_{\text{CAP-FDE}} = \frac{\log_2(M)N}{2(N+N_{\text{cp}})} \quad \text{bits/s/Hz.} \tag{5.10}$$

We notice that the spectral efficiency of CAP-FDE is approximately the same as DCO-OFDM, which is twice those of unipolar schemes such as ACO-OFDM and PAM-DMT.

PAPR performance

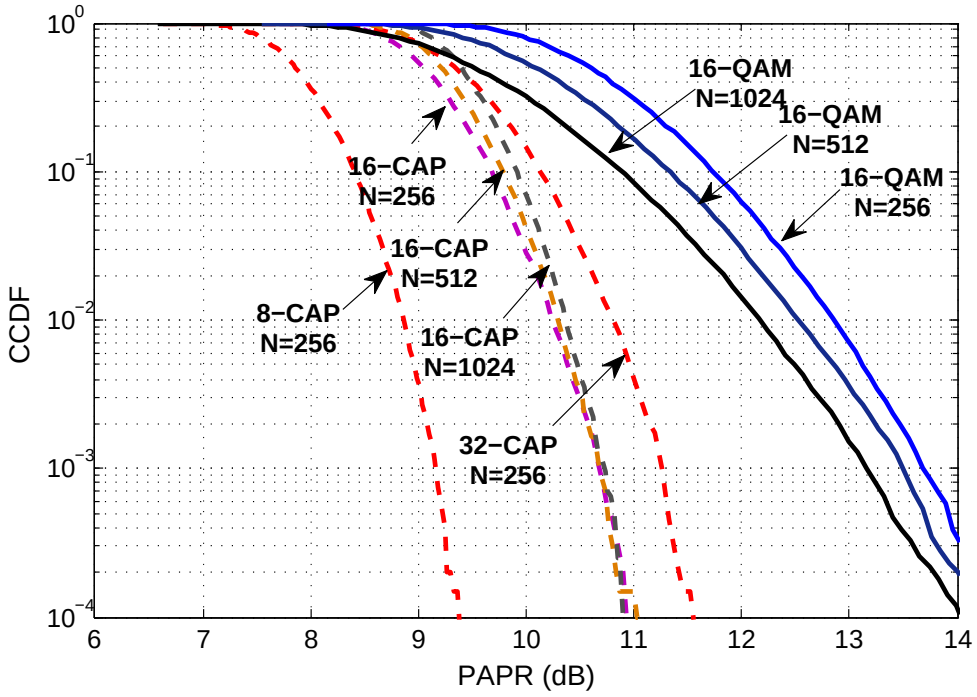

Figure 5.7 — CCDFs of PAPR of CAP (dashed lines) and DCO-OFDM (solid lines) for different modulation orders and block sizes.

As we stated above, being a SC modulation, CAP benefits from a lower PAPR compared with optical OFDM-based schemes. In the previous chapter, we compared the PAPR performance of different optical OFDM schemes. Here, we compare the PAPR performances of DCO-OFDM and CAP. Figure 5.7 shows the CCDF plots of PAPR for CAP and DCO-OFDM for different constellation sizes and block sizes. We can see that the PAPR of CAP is generally much lower than that of DCO-OFDM. For example, for a block size of $N = 256$ and a CCDF of 10^{-3}, the PAPR of 16-CAP is about 2.6 dB lower than 16-QAM DCO-OFDM. Moreover, in contrast to optical OFDM schemes where the PAPR increases remarkably with the block size, the PAPR of CAP remains approximately unchanged. The reason is that the PAPR of DCO-OFDM increases with the number of modulated sub-carriers in the frequency domain, which is directly related

to N, while this is not the case for CAP, being a SC modulation. This could bring extra advantage as we could use a larger N in the case of slowly-varying channel to decrease further the receiver computational complexity.

5.5 BER performance

In this section, we present simulation results to study the performance of the CAP-FDE scheme in the VLC context by taking into account the clipping effect and the frequency response of the LED. The comparison of CAP-FDE and DCO-OFDM in terms of BER performance is also discussed.

5.5.1 Simulation parameters

We assume the same LED transmitter, indoor VLC channel, pulse shaping filters and noise level that we used for evaluating the performance of DCO-OFDM scheme, see Table 4.1. The block size of the CAP-FDE scheme is set to 256 together with a CP of 12. Since CAP-FDE also needs a DC bias to obtain a unipolar signal, we consider the same clipping level and DC bias as we considered for DCO-OFDM in (4.13).

5.5.2 BER performance for different signal bandwidths

We are firstly interested to investigate the merits of using CAP-FDE transmission to go beyond the 3-dB modulation bandwidth of the LEDs. Setting the clipping factor to $\kappa = 10$ dB, as we did for DCO-OFDM, Figure 5.8 shows the BER plots of 32-CAP-FDE as a function of $E_{b,\,\mathrm{elec}}/N_0$ for different R_b/f_c factors. Similar to the case of DCO-OFDM (see Figure 4.7), due to the clipping effect, the system BER first decreases, and then increases after a certain turning point by increasing the electrical SNR. Interestingly, for a fixed target BER, we observe a smaller decrease in the required SNR for different signal bandwidths compared to the case of DCO-OFDM. This is better illustrated in Figure 5.9, where we have plotted the required SNR for CAP-FDE and DCO-OFDM to achieve a BER of 10^{-3} for different R_b/f_c. We notice that CAP-FDE outperforms DCO-OFDM for $R_b/f_c > 4$ in terms of the electrical SNR requirement at the transmitter. Therefore, for high data-rate transmission, CAP-FDE is a more energy efficient scheme. Note that here, although we limit the presented results to the case of 32-CAP for the sake of brevity, this conclusion is also valid for other modulation orders.

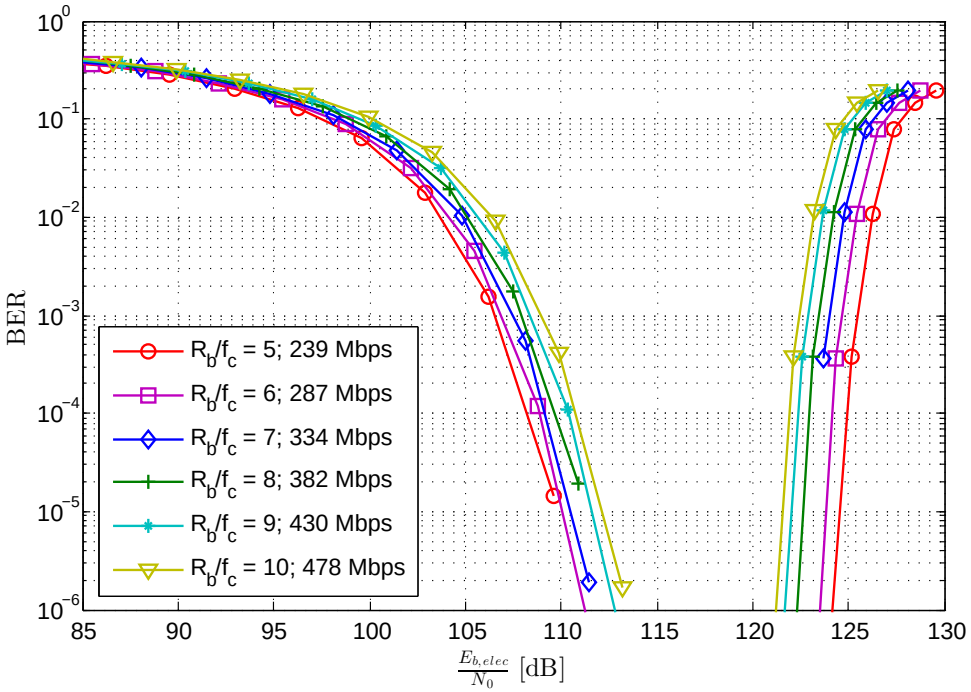

Figure 5.8 — BER performance of 32-CAP-FDE versus the electrical SNR at the transmitter for different R_b/f_c, the clipping factor is set to $\kappa = 10$ dB

5.5.3 BER performance for different clipping factors

As we did for DCO-OFDM, we investigate here the impact of the clipping factor on the system performance. The simulation results for 32-CAP-FDE with clipping factors of 7, 10 and 13 dB are shown in Figure 5.10. Again, we observe that 7 dB clipping provides a better performance than those of larger clipping factors in the low SNR region. Then, after passing a certain SNR, this trend inverses due to the clipping effect. Interestingly, the electrical SNR at the turning points due to clipping noise are approximately the same as for the case of DCO-OFDM in Figure 4.9. However, CAP-FDE has a better BER performance due to its lower PAPR.

5.5.4 Impact of the pulse shaping filter

It is interesting to study the impact of the pulse shaping filter parameters on the performance of CAP-FDE. In particular, these parameters can critically impact the conditions of zero interference between the in-phase and quadrature components. Figure 5.11 shows

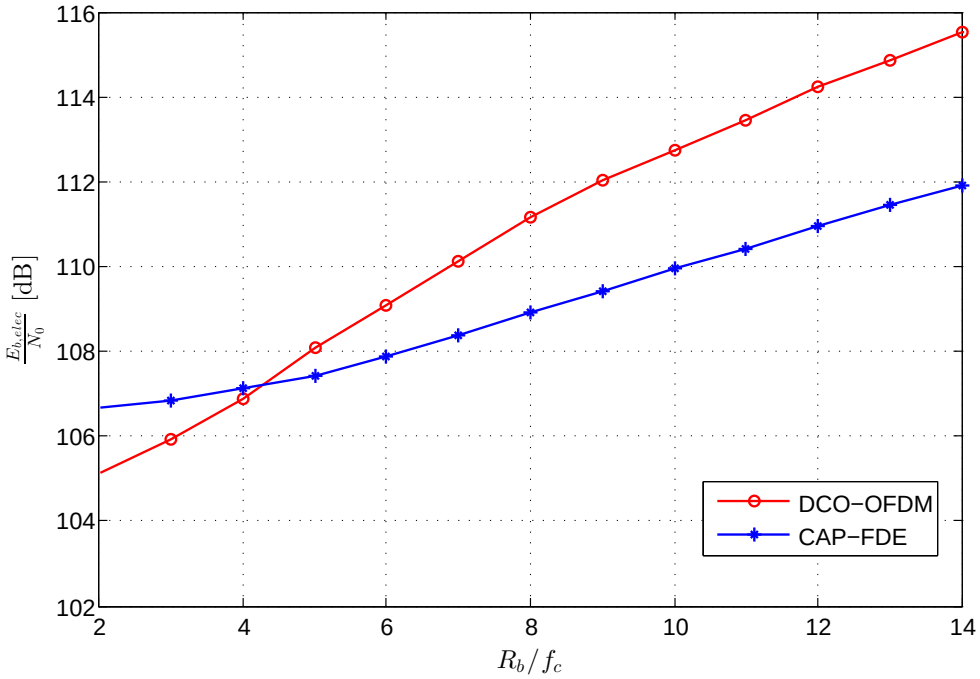

Figure 5.9 — Electrical SNR at the transmitter versus R_b/f_c to achieve a BER of 10^{-3} for 32-QAM DCO-OFDM and 32-CAP-FDE, the clipping factor is set to $\kappa = 10$ dB

the impact of the number of filter taps and roll-off factor of the shaping filters on the system BER performance. We notice from Figure 5.11 (a) that the BER decreases slightly with increasing the filter span as we approach more closely the analog filter, which reasonably results in reduced interference (cross-talk) between the I and Q signal paths. However, note that a longer filter span also involves a higher computational complexity. On the other hand, we observe from Figure 5.11 (b) that the best performance is achieved for the smallest roll-off factors, *i.e.*, 0.1. The reason is that a smaller roll-off factor results in a smaller signal bandwidth, thus, in less Gaussian noise after the MF.

5.6 Chapter summary

In this chapter, we presented the principles of CAP-FDE transmission. We derived the condition of zero interference for the CAP transmitter and explained how the matched filtering and the one-tap equalization can be done at once in the frequency domain to reduce the receiver computational complexity. We then compared CAP-FDE with

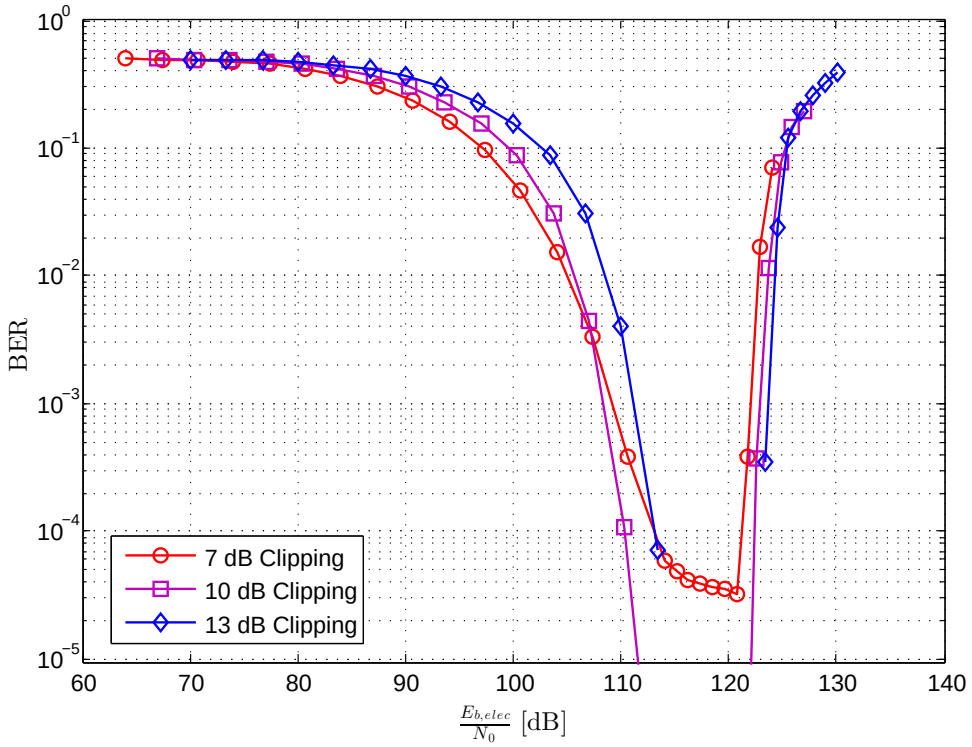

Figure 5.10 — BER performance of 32-CAP-FDE versus electrical SNR at the transmitter for different clipping factors, $R_b/f_c = 10$

optical OFDM schemes in terms of power and spectral efficiency, and PAPR performance. Through numerical results, we also investigated the use of CAP-FDE for high data-rate transmission and showed that it achieves a better performance than DCO-OFDM. The impacts of the filter length and roll-off factor of the pulse shaping filters for the case of CAP-FDE were also investigated. Note that in the comparative studies presented in this chapter, *i.e.*, the performance of CAP-FDE and DCO-OFDM, we did not consider any adaptive loading for the latter scheme. As explained in Appendix D, it is not an easy task to use any bit-power loading algorithm for optical OFDM schemes while taking into account the clipping effect. To make a fair comparison, we limited our study for the case of fixed constellation size (with equal power) for the case of DCO-OFDM.

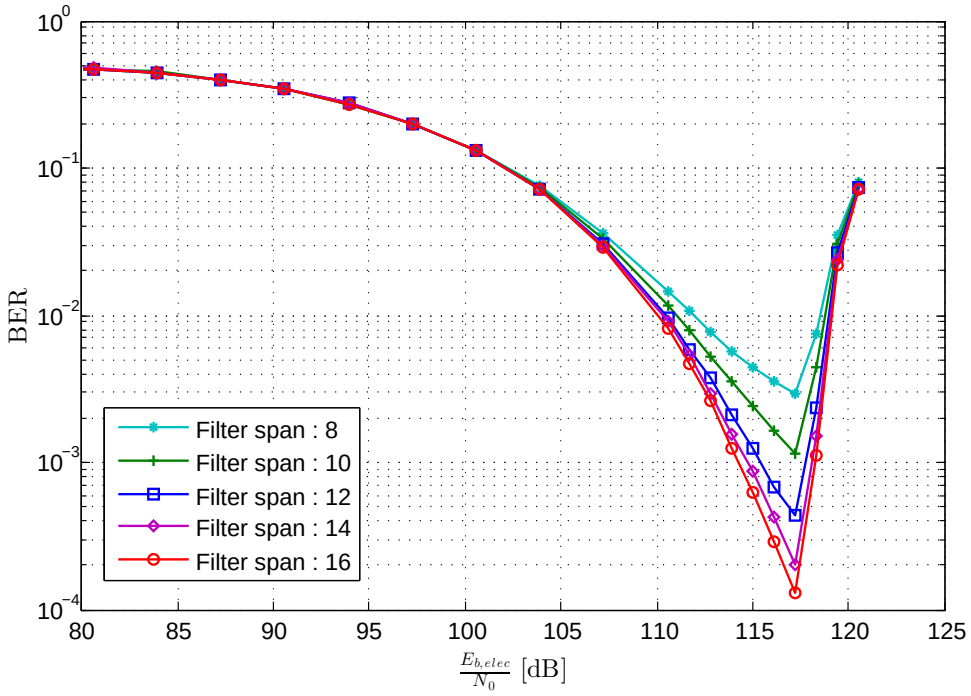

(a)

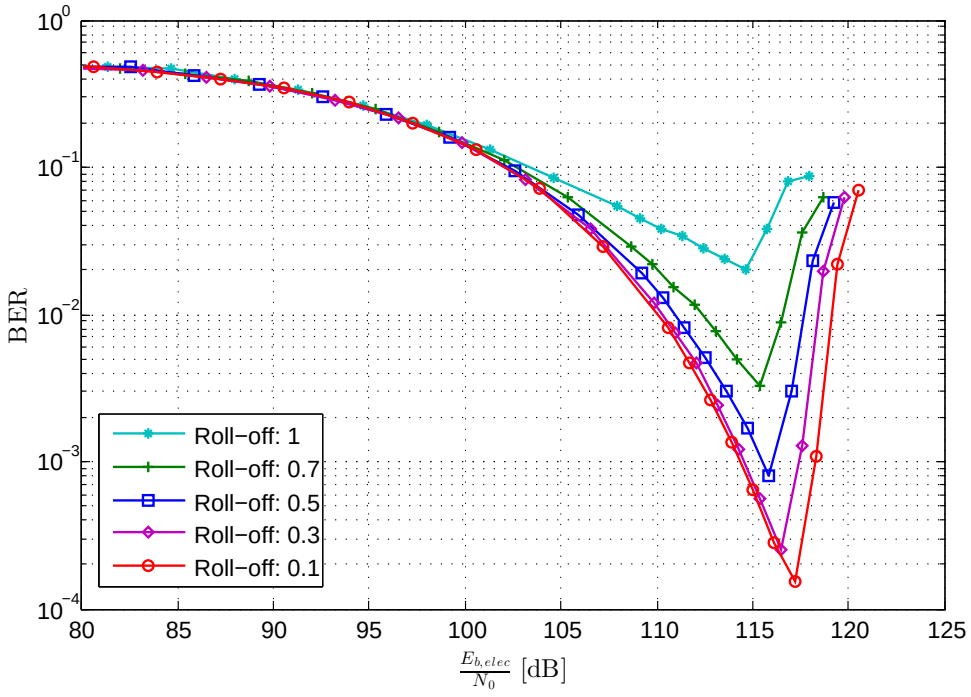

(b)

Figure 5.11 — Impact of (a) filter length with roll-off factor of 0.1 (b) roll-off factors with filter length of 16 symbols on the BER performance for 32-CAP-FDE, $\kappa = 10$dB and $R_b/f_c = 10$.

CHAPTER 6

Impact of LED non-linearity

6.1 Introduction

In the previous two chapters, we considered the use of optical OFDM and CAP-FDE to achieve high data-rate transmission given the limited modulation bandwidth of the LED transmitter, while taking into account the impact of signal clipping. Another important impairment that can degrade the system performance of a VLC link is the non-linear characteristics of the optical front-end including the LED, PD, D/A and A/D. Among all these, the LED is the major source of non-linearity in VLC systems, where in addition to its limited dynamic operation range, it has a non-linear transfer function. We investigated the impact of the clipping noise due to the limited dynamic range of the LED in the previous two chapters. In this chapter, we focus on studying the impact of the non-linear transfer function of the LED on the system performance of the VLC links.

The non-linearity of the transfer function of the LED arises from two phenomena: On one hand, the imperfection of the driving circuits of the LED leads to a non-linear voltage-current relationship. On the other hand, the number of emitted photons of the LED is not directly proportional to the amplitude of the injected electrical current in its active region, resulting in a non-linear transfer function between the input current and the output optical intensity. Figure 6.1 shows an example of the non-linearity between the voltage, current and output optical intensity of a typical white LED (LE CW E2B from ORSAM). Furthermore, note that the response of an LED depends not only on the current value of the injected electrical signal, but also on the previous input, giving rise to a memory effect [13, 25].

The general aim of this chapter is to model this LED non-linearity and gain insight

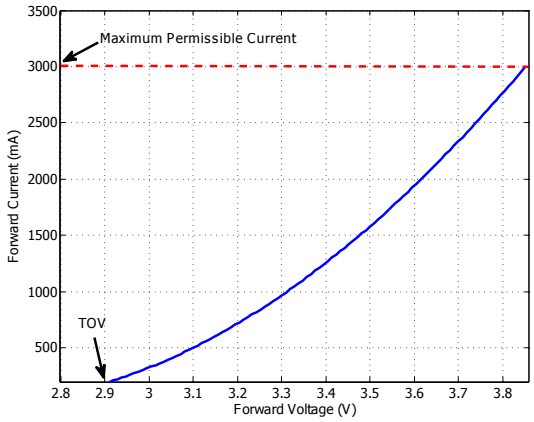

(a)

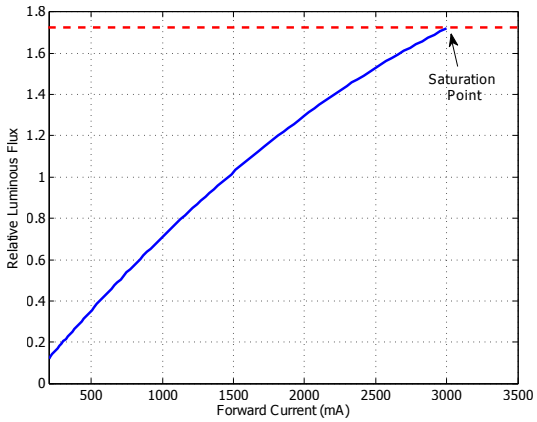

(b)

Figure 6.1 — The relationship of (a) voltage-vurrent curve (b) current-optical power curve of a white LED (OSRAM LE UW Q9WP)

into its impact on the link performance. As we will explain, due to the lack of time, we could not accomplish this study in this thesis. That is why the remaining research directions are presented as perspectives for future works. The remainder of this chapter is organized as follows: We review in Section 6.2 three commonly-used approaches to model the non-linear transfer function of an LED, that is, Volterra series-based model, polynomial model, and Wiener/Hammerstein model, and discuss their prons and cons in terms of accuracy and complexity. Then, in Section 6.3, we attempt to investigate the performance degradation caused by this non-linearity, and in particular, how it impacts

the performance of the two signaling schemes of DCO-OFDM and CAP-FDE. Lastly, we summarize this chapter in Section 6.6.

6.2 Non-linearity models

Depending on whether or not we take into account the memory effect in the non-linearity model of an LED, there exist two types of models: memory-less and memory models. For memory-less models, the common approach is the so-called memory-less polynomial model by which the non-linear transfer function of the LED is approximated using a power series [59, 80]. This approach is very popular in VLC systems due to its simplicity. However, its drawback is its very limited accuracy, especially for the case of high transmission rates. As a matter of fact, since the response of the LED degrades over the frequency of the input current, the LED exhibits strong memory effects as the signal bandwidth increases. In the high data-rate transmission case, memory models are more accurate than memory-less counterparts. For this reason, we focus on the memory models in this chapter and present in the following three widely used non-linear memory models with different accuracies and complexities.

6.2.1 Volterra series based model

Volterra series has been long used to model non-linear systems with memory. The Volterra series, which is a generalization of power series with memory [81], was first studied by Vito Volterra in 1880's as a generalization of the Taylor series of a given function. In fact, the output $y(t)$ for a linear time-invariant (LTI) system can be written as:

$$y(t) = \int_{-\infty}^{\infty} h(\tau)x(t-\tau)d\tau, \tag{6.1}$$

where $h(t)$ is the system IR and $x(t)$ is the input signal. An LTI system is essentially a *memory* system since the output $y(t_0)$ depends not only on the present value of the input $x(t_0)$, but also on the past values $x(t < t_0)$ and the future values $x(t > t_0)$ according to (6.1). However, usually we have $h(\tau = 0)$, for $\tau < 0$, to obtain a causal system.

On the other hand, the relationship between the output $y(t)$ and the input $x(t)$ for a non-linear memoryless system can be approached using power series as

$$y(t) = \sum_{n=0}^{\infty} c_n x^n(t). \tag{6.2}$$

The Volterra series, which is a combination of the non-linear memory-less system by (6.2) and the linear memory system by (6.1), is then defined as [81]:

$$y(t) = h_0 + \sum_{k=1}^{\infty} \int_{-\infty}^{\infty} \dots \int_{-\infty}^{\infty} h_k(\tau_1, \dots \tau_k) x(t-\tau_1) \dots x(t-\tau_k) d\tau_1 \dots d\tau_k \tag{6.3}$$

where h_0 is a constant and $h_k(\tau_1, \dots, \tau_k)$ are the kernels of the Volterra series, which determine the non-linearity and are of infinite length. For practical implementations, a discrete-time truncated version with finite LTI length and linearity order is more commonly used as follows:

$$y(n) = h_0 + \sum_{m=0}^{M} \sum_{k_1=0}^{K_1} \cdots \sum_{k_m=0}^{K_m} h_m(k_1, \cdots, k_m)\, x(n-k_1) \cdots x(n-k_m), \tag{6.4}$$

where M is the highest non-linearity order, and K_m is the memory length of the m-th order Volterra kernel.

Volterra series has a good accuracy in predicting the non-linear characteristics of an LED. It is shown in [25] that a second-order Volterra series can already provide a fair approximation to the power spectrum of the LED up to 14 MHz, which achieves the best accuracy compared with other models. However, the main drawback of the Volterra series based model is its high complexity. In fact, the number of coefficients of the n-th order discrete Volterra kernel $h_n(\tau_1, \dots, \tau_n)$ with a memory filter length of L is L^n. Thus, the total number of coefficients of the corresponding model increases exponentially as the non-linearity order and the memory length increase, which makes it impractical for real-time applications. The use of Volterra series based modeling for VLC systems has been considered in [82, 83], where a second-order Volterra series is used to make a good compromise between complexity and performance.

6.2.2 Memory polynomial model

The generalized memory polynomial model is a simplification of the complete Volterra series based models by considering only the diagonal coefficients [82, 84] in Volterra kernels. In other words, for the n-th order Volterra kernel $h_n(k_1, \cdots, k_n)$, we set $h_n(k_1, \cdots, k_n) = 0$ except along the diagonal $k_1 = \cdots = k_n$. Then, from (6.4) we obtain:

$$y(t) = \sum_{m=1}^{M} \sum_{k=0}^{K} a_{mk}\, x(n-k)^m \tag{6.5}$$

where $a_{mk} = h_m(k, k, \dots, k)$, M is the non-linearity order, and K is the memory length. The number of the coefficients of this model is on the order of $(K+1)$, which is a

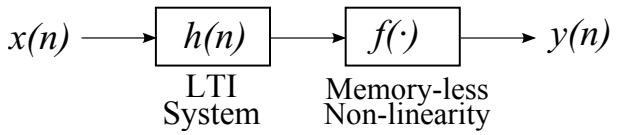

(a)

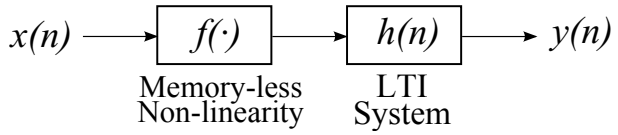

(b)

Figure 6.2 — Block diagram of (a) Wiener model (b) Hammerstein model

great simplification compared to $(K+1)^M$ in the case of using the complete Volterra series model. Thus, it offers a good compromise between accuracy and complexity, as compared with the memory-less models and the Volterra series based model. The use of the polynomial model for VLC systems is considered, for instance, in [85].

6.2.3 Wiener and Hammerstein model

Further simplification of the Volterra series leads to the so-called Wiener [85, 86] and Hammerstein [83,87] models. The Wiener model consists of an LTI system followed by a memory-less non-linear function. The Hammerstein model is similar to the Wiener model, while the order of the LTI system and the memoryless non-linear function is reversed. The block diagrams of these two models are shown in Figure 6.2, which are very popular in the current literature owing to their simplicity. In fact, in addition to its simplicity, the separation of the memoryless non-linearity part and linear memory part allows a simple equalization at the receiver. The memoryless non-linearity can be compensated using a simple pre-distorter at the transmitter or a post-distorter at the receiver, as studied in [26,87]. The linear memory part, on the other hand, can be equalized using the time-domain or frequency-domain equalization techniques [88]. Despite their simplicity, one drawback of these models is their relatively low accuracy, compared to other non-linear models. In particular, it is shown in [25] that these two models provide poor accuracy for modeling the non-linear characteristics of the LED in the case of large modulation

Table 6.1 — Fitted polynomial coefficients c_k of degree k of the LED according to the Hammerstein model [58]

c_3	c_2	c_1	c_0
0.29	-1.09	2.06	-0.0003

bandwidths. Therefore, a compromise should be made carefully between performance and simplicity when using these two models in the VLC context.

6.3 Impact of LED non-linearity

Here we present a set of numerical results to investigate the impact of the non-linear transfer function of the LED on the performance of DCO-OFDM and CAP-FDE.

6.3.1 Simulation parameters

For the reason of simplicity, we consider a Hammerstein model to model the non-linear transfer function of the LED. The memoryless non-linearity block of the Hammerstein model is approximated by a third degree polynomial whose coefficients are provided in Table 6.1 for a real white LED. The LTI block of the model is assumed to be a first-order low pass filter, as described in Section 2.2.2. The rest of the simulation parameters are the same as we considered for the case of linear LED for DCO-OFDM and CAP-FDE in Sections 4.4 and 5.5. Note that for illustrating the impact of the non-linear transfer function of the LED, we do not show the results in the high SNR region, which is dominated by the excessive clipping noise.

6.4 BER performance for different signal bandwidths

Figure 6.3 shows the BER performance of 32-QAM DCO-OFDM and 32-CAP-FDE as a function of the electrical SNR at the transmitter for different signal bandwidths . For comparison, we have also presented the results for the case of a linear LED that we considered in Chapters 4 and 5. Note that the case of a non-linear LED shows a better performance than those for the case of a linear LED, which could be misleading. The reason lies in the transfer functions of the LED that we consider for the linear and non-linear LED cases, which are shown in Figure 6.4. In fact, since a *linear* LED does

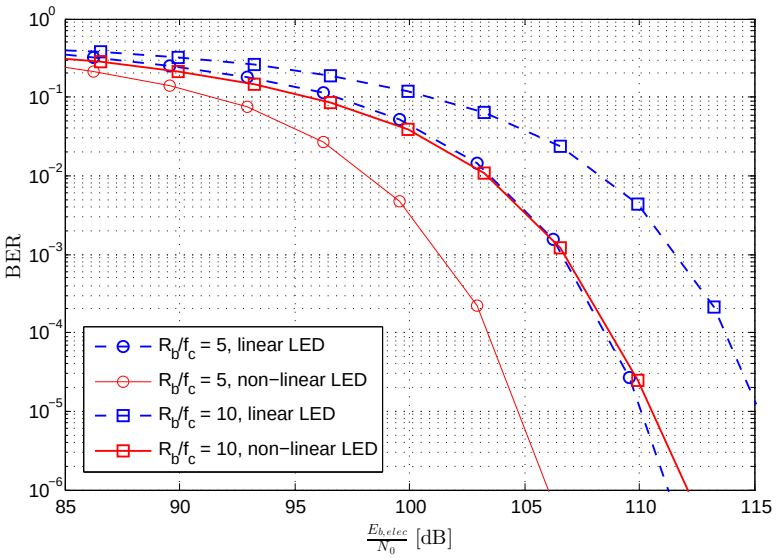

(a)

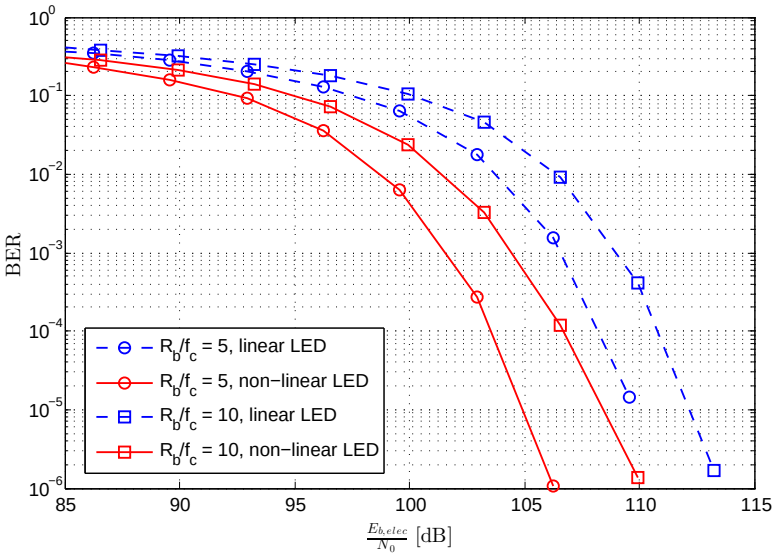

(b)

Figure 6.3 — BER performance as a function of the electrical SNR at the transmitter for the cases of a linear (dash lines) and a non-linear LED (solid lines) for different signal bandwidths (a) 32-QAM DCO-OFDM (b) 32-CAP-FDE, $\kappa = 10$ dB.

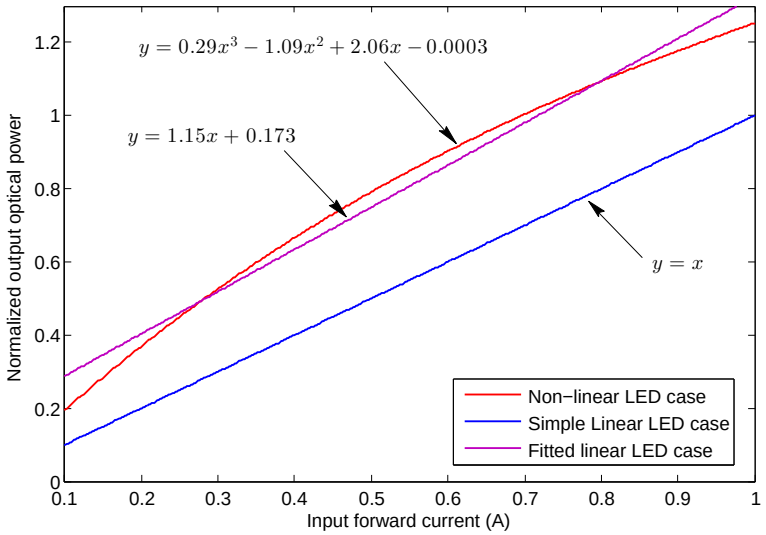

Figure 6.4 — Considered transfer functions for the case of linear and non-linear LED

not really exist, there are many choices for the linear approximations of the non-linear function given in Table 6.1, for example, we could use the linear fitted curve (purple line) or a simple $y = x$ line (in blue) to represent a linear LED.

To be coherent with our previous simulations where the non-linear transfer function is not considered, *i.e.*, a simple relationship $y = x$ was assumed for the input current-optical power relationship, here, we chose the simple identity line for comparison. As a result, we note that for the same input current, the non-linear LED has a larger output optical power. That is why we have a better for the non-linear case in Figure 6.3. For this reason, such a comparison is not fair and can not show the impact of non-linear transfer function of the LED. However, by comparing the difference of the required SNR to achieve a given BER for the linear and non-linear cases for different modulation schemes, we can determine which one is more sensitive to the signal distortion caused by this LED non-linearity. For example, considering a target BER of 10^{-3}, this SNR differences for DCO-OFDM are about 5.5 and 4.8 dB for $R_b/f_c = 5$ and 10, respectively, while for CAP-FDE, they are about 5 and 4.5 dB. The SNR penalties are slightly larger for the case of DCO-OFDM, which testifies its higher sensitivity to LED non-linearity, as compared with CAP-FDE.

6.5 BER performance for different constellation sizes

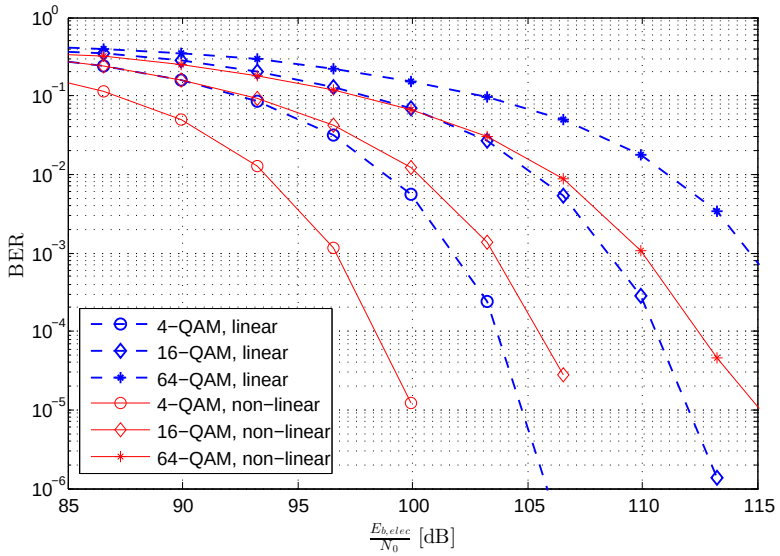

(a)

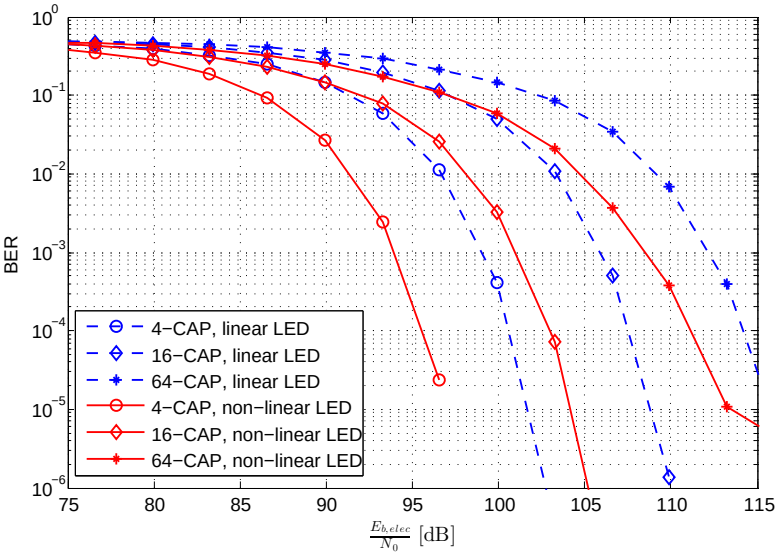

(b)

Figure 6.5 — BER performance as a function of the electrical SNR at the transmitter for the case of a linear (dash lines) and non-linear LED (solid lines) for different constellation sizes of (a) DCO-OFDM (b) CAP-FDE, $R_b/f_c = 10$ and $\kappa = 10$ dB.

We have also investigated the BER performance of DCO-OFDM and CAP-OFDM for different constellation sizes where the results are shown in Figure 6.5 for a fixed $R_b/f_c = 10$. For the same reason that we explained above, to compare the linear and non-linear cases, we should again reason in terms of SNR penalty. We notice that DCO-OFDM suffers more penalty from the LED non-linearity with increased constellation size. For instance, the SNR penalty between the linear and non-linear LED cases is about 5, 5, and 4.8 dB for the cases of 4-QAM, 16-QAM, and 64-QAM DCO-OFDM, respectively. The CAP-FDE scheme benefits from a lower penalty compared to DCO-OFDM, which is around 4, 4, and 2.9 dB for the cases of 4-CAP, 16-CAP and 64-CAP, respectively. Overall, these results testify again the lower sensitivity of CAP-FDE to LED non-linearity, as compared with DCO-OFDM.

6.6 Chapter summary

In this chapter, we focused on the modelling of the non-linear transfer function of the LED transmitter. We presented three commonly approaches with different accuracies and complexities, including the Volterra series, polynomial models and the Hammerstein/Wiener models. Through numerical simulations, we then investigated the impact of this kind of LED non-linearity on the performance of DCO-OFDM and CAP-FDE by considering a Hammerstein model. We showed that DCO-OFDM is more sensitive to signal distortion caused by this LED non-linearity than CAP-FDE. However, due to the limitations of the approach we used, we were unable to directly quantifying the penalty arising from the non-linear transfer function, compared to the linear case. A future research direction will be to find a solution to quantify the penalty and also to investigate efficient corresponding techniques to reduce the adverse impact of this non-linearity.

CHAPTER 7

Experimental study of a typical VLC link

7.1 Introduction

In the previous chapter, we have investigated the performance of DCO-OFDM and CAP-FDE by taking into account the non-linear characteristics of the LED via Monte-Carlo simulations. In this chapter, we present some experimental results for a typical VLC link that we carried out in Northumbria University, Newcastle, UK. These studies could be realized thanks to the collaboration between Institut Fresnel and the OCRG laboratory with the support of Opticwise COST Action IC1101 within the framework of a Short Term Scientific Mission (STSM). I benefited much from the facilities in this laboratory and also from the fruitful discussions with the researchers there. Being novice in experimental works, I could never implement the experimental set-up without their help. During my short stay in their laboratory from 4th to 31st May 2015, I carried out a set of experiments to investigate the non-linear characteristics of an LED and to study the performance of DCO-OFDM and CAP-FDE in order to validate my theoretical and simulation-based studies. However, due to time limitation and the constraints of the available optical front-ends, I could conduct only a limited number of experiments. Nevertheless, these experiments let us gain insight into the practical implementation considerations of VLC systems and helped us enrich our theoretical studies.

The rest of this chapter is organized as follows: In Section 7.2, we first present the pre-measurements to investigate the modulation characteristics of the LED that we use for the experiments. Then, we briefly describe the experimental set-up on which we study the DCO-OFDM and CAP-FDE transmission. In Section 7.3, we present the experimental results of these two schemes in terms of the BER performance for different modulation orders and data rates. The influence of non-linearity of the LED is also

investigated by changing the DC-bias current. Lastly, Section 7.4 concludes this chapter.

7.2 Pre-measurement of the LED transmitter

It is important to specify the parameters of the LED that we are going to use in the following test-bed. We use an LED from Luxeon Rebel with a cover of plastic lens. However, very few parameters of this LED are provided in its data sheets. Hence, we have measured the following parameters of the LED prior to building our test-bed:

- Radiation pattern and semi-angle at half power
- Forward current versus output optical power
- Frequency response and 3-dB bandwidth

We also used these measured data to validate the assumptions that we made on the LED transmitter throughout this thesis.

7.2.1 Radiation pattern and semi-angle at half power

As stated in Chapter 3, the LED is assumed to be a Lambertian source whose radiation pattern is characterized by its semi-angle at half power. The set-up to measure the semi-angle of the LED is depicted in Figure 7.1. The LED and a power meter are installed on two parallel tracks (Tracks I and II), respectively. The received power P_{rx} at the power meter can be expressed as according to Equation (3.2):

$$P_{rx} = T(\phi) A_r \cos(\varphi)/r^2 \tag{7.1}$$

where A_r is the receiving area of the power meter, φ is the incident angle ($\varphi = \phi$ in this configuration) and r is the distance between the LED and power meter. In this set-up, we have $r^2 = d^2 + L^2$ where L is the distance of power meter from the origin O in Figure 7.1. We normalize the received power P_{rx} by the power P_0 at $L = 0$, i.e., where the LED and power meter are aligned. Regarding Equations (3.2) and (7.1), the normalized power $\hat{P}_{rx}$ can be expressed as:

$$\hat{P}_{rx} = d^2 \cos^{m+1}(\phi)/r^2, \tag{7.2}$$

where $\cos(\phi) = \sqrt{d^2/r^2}$. Taking the natural logarithm on both sides of (7.2), we obtain

$$\ln(\hat{P}_{rx}\, r^2/d^2) = (m+1)\ln(\cos(\phi)) \tag{7.3}$$

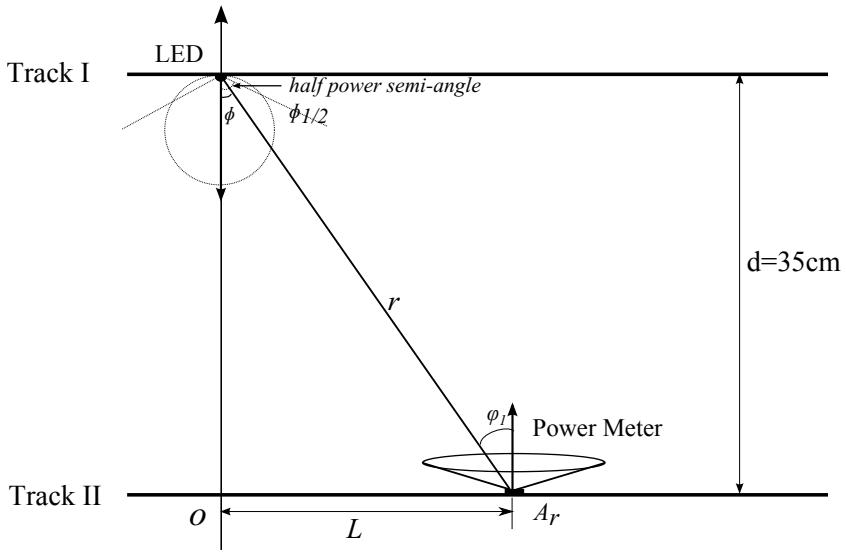

Figure 7.1 — set-up of measuring the semi-angle at half power of the LED

Thus, by varying the position L of the power meter on Track II and measuring the corresponding normalized received power, the Lambertian order m, together with the semi-angle can be calculated. The measured L and the corresponding normalized received power are given in Table 7.1. Also, the plot of the measured data is shown in Figure 7.2.

L(cm)	0	1	2	3	4	5	6
$\hat{P}_{rx}$	1	0.9802	0.9648	0.9429	0.9231	0.8769	0.8352
L(cm)	7	8	9	10	11	12	13
$\hat{P}_{rx}$	0.7846	0.7275	0.6589	0.5956	0.5297	0.4663	0.4064

Table 7.1 — The measured normalized received power and the corresponding L

We can see that the curve is almost linear, meaning that the Lambertian model is an appropriate model for the radiation pattern of the LED we used. The Lambertian order is about $m = 10.6$ and the corresponding semi-angle is about $\phi_{1/2} = 20°$.

7.2.2 Transfer function of the LED

For investigating the effect of the LED non-linearity on the transmission schemes such as DCO-OFDM and CAP-FDE, we should determine the transfer function between the input current and the output optical power of the LED. Since the power meter that we used to measure the LED radiation pattern can only get the output optical power at a

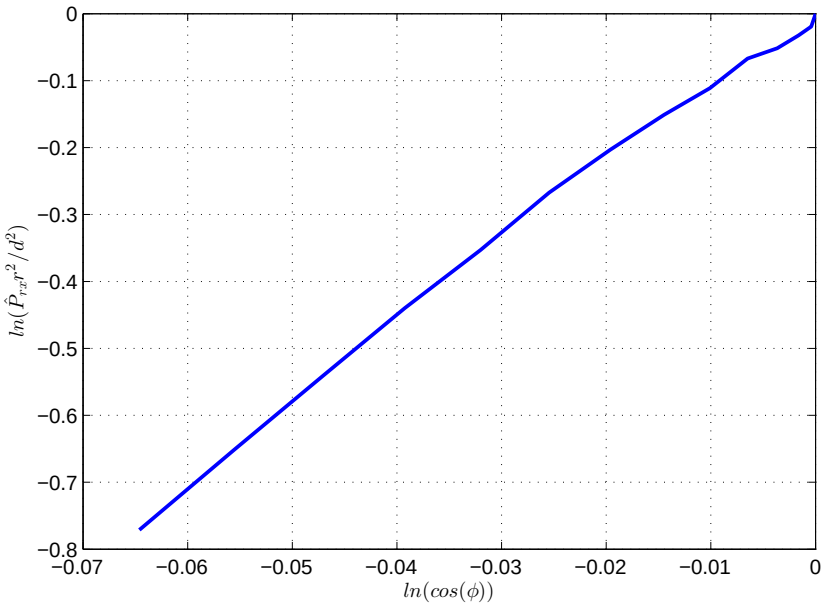

Figure 7.2 — Linear fit of the measured data for semi-angle

typical wavelength (set to 480nm in our set-up), for reference, we also used a lux meter to measure the output illuminance. The results of normalized output optical power and illuminance versus the DC-bias current are shown in Figure 7.3. We can see that the curves of output optical power and the illuminance are almost identical. Moreover, we notice that the relationship between the input current and output optical power is not linear, as we expected.

7.2.3 Frequency response of the LED

Another important characteristics of the LED that we should determine before applying any transmission scheme is its frequency response. In Chapter 2, we assumed that it can be modelled by a first-order low pass filter. Here, we intend to validate this assumption by experiments. Instead of using a complex and expensive network analyzer, we used a simple method with an arbitrary waveform generator (AWG) and an oscilloscope to measure approximately the frequency response of the LED. We first generated a sinusoid using the AWG; then, this signal is fed to the LED after adding a DC bias current using a power supply. The signal input to the LED can be expressed as

$$s(t) = A_s/Z \sin(2\pi f_c t + \varphi) + i_{\text{dc}} \tag{7.4}$$

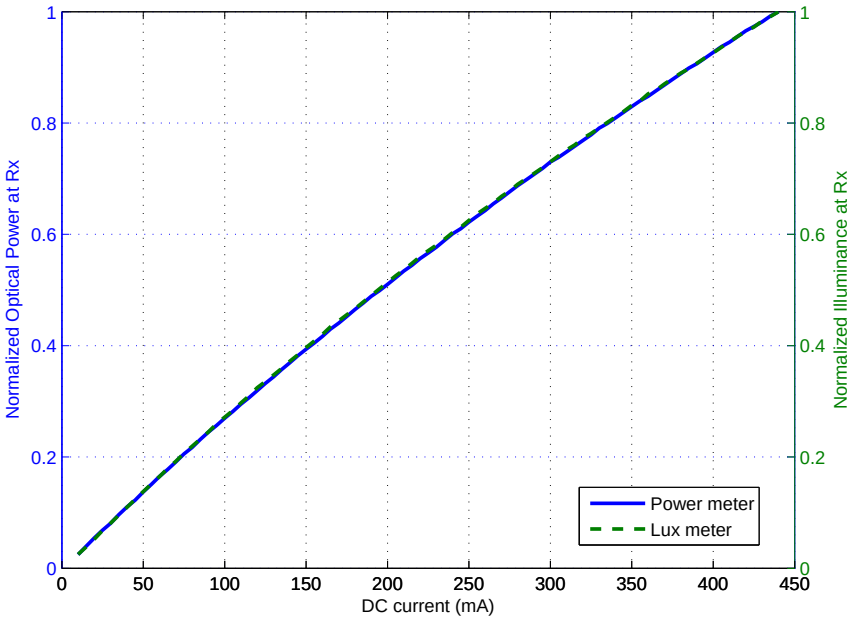

Figure 7.3 — Measured data of DC current versus output optical power and illuminance

where A_s is the amplitude of the input signal that was set to 2 Vpp at the AWG, Z is the impedance of the circuit that we use, f_c is the input frequency, φ is the phase and i_{dc} is the DC bias forward current, which was set to 250 mA in this experiment. At the receiver, a PD is used to capture the received optical signal and to convert it to an electrical signal. Then, we measure the amplitude of the received signal A that was displayed on the screen of the oscilloscope. The results are shown in Table 7.2.

According to the definition of the frequency response, the normalized response at frequency f_c of the LED is A/A_0 where A_0 is amplitude at zero frequency. Note that the zero frequency means a DC signal, which implies that $A_s = 0$; $A = 0$. To obtain information at near DC, we use a very low frequency, *i.e.*, 0.001 MHz to represent the zero frequency in our experiment. The measured normalized frequency response together with the fitted curve by a first-order low pass are plotted in Figure 7.4. We can see that the theoretical model agrees well with the measured data, which validates our assumption on the modulation characteristics of the LED. Moreover, we notice that the LED used in our set-up has a very small modulation bandwidth of only 0.384 MHz. Given this relatively low bandwidth, we limit therefore the data rate in our following experiments to a few Mbps.

Frequency (MHz)	Amplitude (mV)	Frequency (MHz)	Amplitude (mV)
0.001	572	2.6	71.6
0.2	474	2.8	64.7
0.4	402	3.0	58.7
0.6	334	3.2	53.5
0.8	273	3.4	48.2
1.0	227	3.6	43.4
1.2	193	3.8	40.2
1.4	163	4.0	37
1.6	137	4.2	34.6
1.8	119	4.4	31
2.0	104	4.6	29.1
2.2	91	4.8	28.5
2.4	81	5.0	25.5

Table 7.2 — Measured amplitudes of the received signal at different frequencies

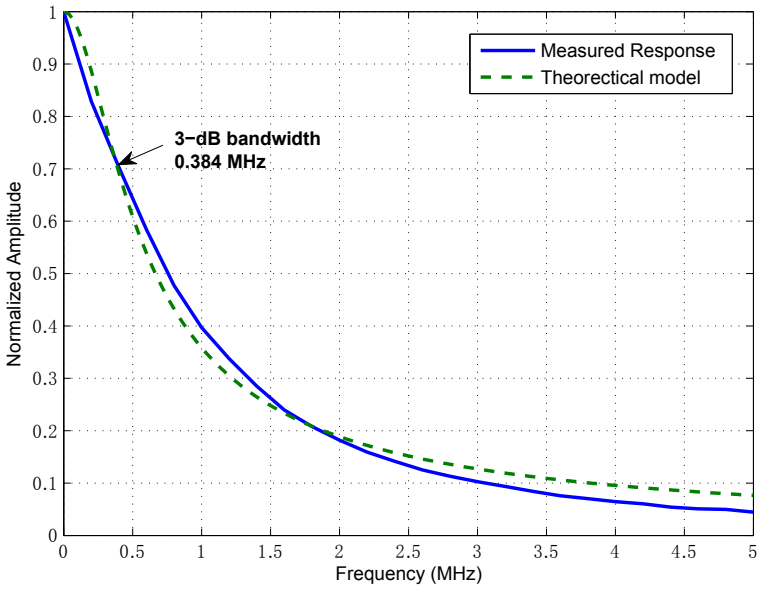

Figure 7.4 — Measured frequency response of the LED and that of the first-order low-pass filter

7.3 BER performance of DCO-OFDM and CAP-FDE

7.3.1 Experimental set-up

Table 7.3 — Main parameters of the experimental set-up

Parameter		Value
LED	Reference	Luxeon Rebel
	3-dB bandwidth	0.384 MHz
	Semi-angle	20°
AWG	Reference	Tektronix AFG3021
	Maximum Frequency	25 MHz
	Samping Rate	250 MS/s
	Resolution	14 bits
Modulation	FFT Size	256
	CP length	12
Pulse shaping filter	Type	Raised Cosine Filter
	Upsampling factor	5
	Filter Span	16
Channel	Transmission distance	30 cm
PD	Type	PIN
	Active area	15 mm^2
	Sensitivity range	430 - 900 nm
Oscillioscope	Reference	InfiniiVision 3000 X-Series
	Sampling Rate	2GS/s
	Bandwidth	100 MHz

The block diagram together with a snapshot of the experiment set-up are shown in Figure 7.5. The generation of the DCO-OFDM and CAP-FDE modulated signals is realized by a Matlab program. Then, this digital modulated signal is converted to an electrical current with the help of an AWG. Next, a DC bias current is added to obtain a unipolar signal prior to feeding the LED. The LED transmitter and the PD receiver are installed on a track and pointed towards each other. At the receiver, the PD detects the light intensity generated by the LED and converts it back to an electrical signal. Then, this electrical signal is low pass filtered and sampled by a digital oscilloscope and

transferred to the computer via a USB cable for later processing. Note that the low filter is not shown in Figure 7.5 because it is built inside the oscilloscope. The demodulation of the DCO-OFDM and CAP-FDE transmission together with the synchronization and equalization are then performed using an off-line Matlab program and finally the BER is calculated. The main parameters of the set-up are summarized in Table 7.3.

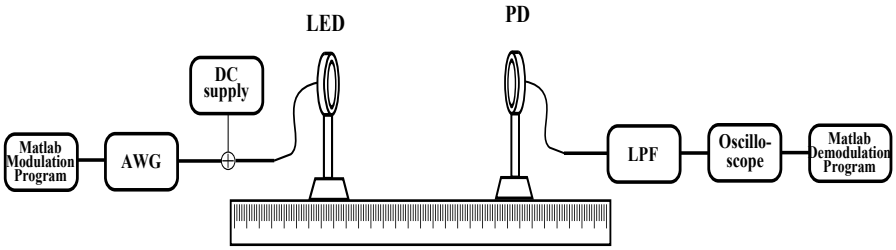

(a)

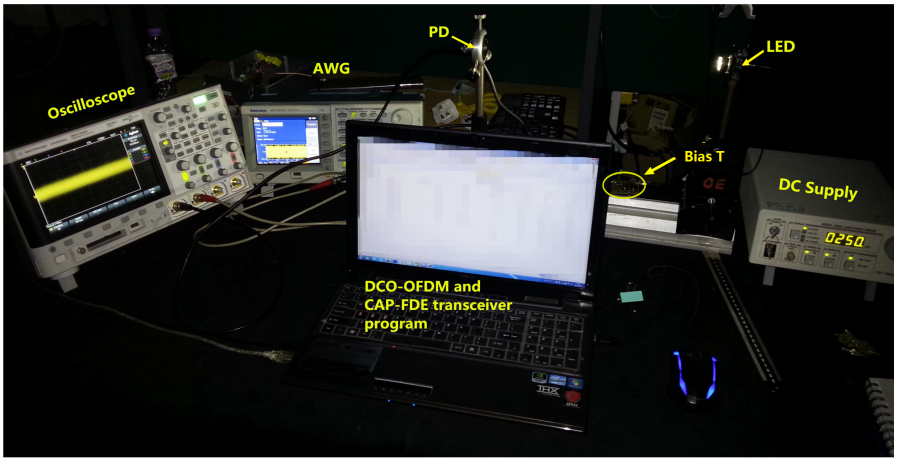

(b)

Figure 7.5 — (a) Block diagram and (b) Snapshot of the set-up in OCRG lab

7.3.2 BER performance of DCO-OFDM and CAP-FDE

The BER performances of DCO-OFDM and CAP-FDE for different constellation sizes and signal bandwidths are depicted in Figure 7.6. The power of the input electrical signal is set to 3 Vpp at the AWG and a DC-bias current of 250 mA is considered. As we can see from the figure, the performance of CAP-FDE is generally better than DCO-OFDM, which validates our theoretical findings. Moreover, the performance gap between these two schemes becomes larger when the modulation orders increases. The reason is that

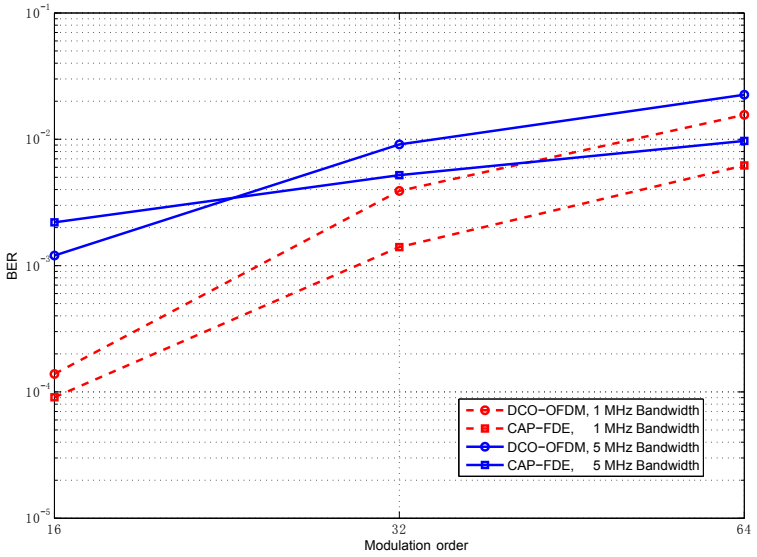

Figure 7.6 — BER performance of DCO-OFDM and CAP-FDE (3Vpp, 250mA DC bias) for different modulation order and signal bandwidth

the distortion caused by the non-linear transfer function become more important as the modulation order increases. Then, the performance of CAP-FDE, which has a smaller PAPR compared to DCO-OFDM for a given constellation size, is less affected by this non-linear distortion.

7.3.3 Impact of the DC-bias current

As stated before, most LEDs have a very limited linear operation range. The signal amplitude beyond this range is clipped before feeding to the LED, resulting a non-linear distortion called clipping noise. Thus, it is important to set an appropriate DC bias to fit the signal to the operation range of the LED. In this experiment, we investigated the effect of DC-bias current on the performance of DCO-OFDM. Results are shown in Figure 7.7. We can see that the BER is first decreased when we increase the amplitude of the input signal (in terms of Vpp at the AWG), then after a certain turning point, the BER starts to increase, resulting a V-shape curve. This is because the signal is clipped when its amplitude is outside the allowed operation range of the LED, thus resulting in more clipping noise. Moreover, we observe than the BER performance of DCO-OFDM at the DC-bias current of 250 mA is generally better than those of 450 mA. The reason

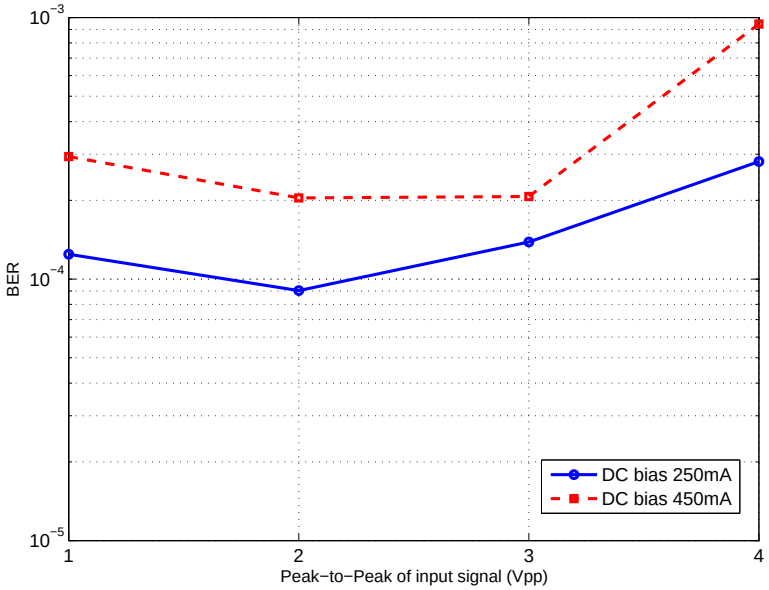

Figure 7.7 — BER performance of DCO-OFDM (16-QAM, 1 MHz bandwidth) for different values of input signal power (in terms of Vpp at the AWG) and DC bias

is that the operation range of the LED is centred around 250 mA, thus we have less distortion arising from clipping noise at 250 mA than that at 450 mA.

7.4 Chapter summary

We implemented a typical VLC link and carried out a set of experiments to study the performance of DCO-OFDM and CAP-FDE transmission schemes. Through the preliminary results that we obtained, we first validated our assumptions on the LED transmitter concerning its radiation pattern and frequency response. Then, we testified that CAP-FDE can outperform DCO-OFDM mainly due to its relatively lower PAPR. We also investigated the impact of the DC-bias on the performance of DCO-OFDM regarding the non-linear transfer function between the input current and output optical power of the LED transmitter. It is worth mentioning that due to limitations on the available optical front-ends (especially the 3-dB bandwidth of the LED that was less than 1 MHz), the data-rate that we managed to achieve was not very high. However, although we could not establish a high data-rate link, the results we obtained validate our main conclusions on the comparison of DCO-OFDM and CAP-FDE based signal transmission.

CHAPTER 8

Conclusions and perspectives

8.1 Conclusions

Visible-light communication is a promising technology for the downlink of the future high data-rate wireless networks. It provides numerous advantages compared to its RF counterparts, including a large unregulated bandwidth, enhanced transmission security, and immunity to electro-magnetic interference. However, as explained in Chapter 2, in terms of achieving high date-rate transmission, we are concerned with two major impairments in VLC systems: the indoor multipath propagation channel and the non-ideal characteristics of the LED. In this thesis, we focused on investigating the potential limitations arising from these two impairments and proposed solutions to address their adverse effects.

For this purpose, we first studied the indoor VLC channel in Chapter 3 by developing an efficient algorithm to simulate its IR, which consists of the LOS and the diffuse parts. Then, based on the IR that we obtained, we characterized the frequency selectivity of the indoor VLC channel for several indoor link scenarios by considering different metrics, including the classical frequency response, channel RMS delay spread and the more appropriate signal-to-ISI ratio. Our study revealed that the channel frequency selectivity arises mainly from the multiple LOS paths rather than multipath reflections. Moreover, we found that when a LOS exists between the transmitter and the receiver, the indoor VLC channel can be considered as practically flat under such conditions. We also studied the effect of receiver filters on the performance of baseband VLC systems and showed the merits of using a Bessel filter rather than the classical matched filter in terms of robustness against multipath dispersion.

Given the limited modulation bandwidth of the LED transmitter, in Chapter 4, we investigated then the suitability of using optical OFDM schemes, including DCO-OFDM, ACO-OFDM and PAM-DMT, to achieve high data-rate in the VLC context. Regarding the high PAPR issue of ACO-OFDM and PAM-DMT, we focused on studying the BER performance of DCO-OFDM by taking into account the clipping effect and the frequency response of the LED. We showed how DCO-OFDM is able to exploit the spectrum far beyond the 3-dB modulation bandwidth of the LED when using a simple ZF equalizer and without adaptive bit-power loading. Through simulation results, we also demonstrated the sensitivity of the optical OFDM schemes to clipping effects due to their relatively high PAPR.

In Chapter 5, we investigated the use of a CAP-FDE transmission scheme to reduce the non-linear distortions caused by high PAPR in the VLC systems. We derived the conditions of zero interference for the CAP modulation and explained how matched filtering and ZF equalization can be done at once in the frequency domain at the receiver to further reduce its computational complexity. Through numerical results, we showed that CAP-FDE is able to achieve high data rate transmission just like DCO-OFDM, while benefiting from less distortion from clipping effect, thanks to its lower PAPR. The impact of the pulse shaping filters' parameters, such as the filter length and the roll-off factor, was also studied in this chapter. Lastly, we compared the BER performance of CAP-FDE and DCO-OFDM schemes for different modulation bandwidths for fixed constellation size and clipping factor. These results demonstrated the merits of CAP-FDE over the commonly used DCO-OFDM scheme.

In Chapter 6, we were interested to model the non-linear transfer function of the LED and to study its impact on the performance of the previous two schemes. To model the non-linear characteristics of the LED, we discussed three approaches with different accuracies and complexities, including Volterra series-based models, polynomial models, and Hammerstein/Wiener models. For investigating the impact of this non-linearity, we simulated the BER performance of the proposed DCO-OFDM and CAP-FDE schemes by considering the Hammerstein model without using any non-linear equalization at the receiver. We showed that CAP-FDE suffers from less signal distortion from the non-linear transfer function of the LED than DCO-OFDM, which again demonstrated the merits of the former scheme.

Finally, we intended to verify our simulation results by experimental works in Chapter 7. Thanks to the support from the Europe FP7 COST Action IC1101 and the OCRG lab, I could realize a test-bed and carry out some experimental measurements. After val-

idating our assumptions on the radiation pattern and the modulation characteristics of the LED, we could test the performance of the DCO-OFDM and CAP-FDE transmission schemes. The post-processing results validated our main conclusions regarding these two signaling schemes specified in Chapters 4, 5 and 6.

8.2 Perspectives

This thesis was devoted to investigating the limitations arising from the indoor VLC channel and the LED transmitter and to proposing efficient signal processing solutions to address their adverse effects. The work presented in this thesis responds to the main part of the objectives presented in Chapter 1. However, due to time limitation, future work should deal with the following directions in depth.

We explained the principles of adaptive bit-power loading for optical OFDM transmission in Appendix D but we did not consider any adaptive loading scheme in the presented simulation results for DCO-OFDM. The reason was due to the difficulty of integrating clipping noise with the existing bit-power loading algorithm, which has been ignored in the current literature [49, 89]. The achievable link data rate in our simulation could be further optimized by employing an appropriate bit-power loading algorithm that takes properly the clipping noise into account. Proposing such suitable adaptive loading algorithms for optical OFDM schemes is an interesting and important research direction for future work.

Concerning the impact of the non-linearity of the LED on the system performance that we investigated in Chapter 6, future research should consider proposing efficient non-linear equalization solutions to mitigate the signal distortion caused by this non-ideal characteristics of the LED. Unfortunately, we could not work on this subject in this thesis due to lack of time. Previous works such as [88] have proposed using hybrid time-frequency domain equalization techniques by considering the Hammerstein model. Concatenated Volterra series-based non-linear equalization was also proposed in [72, 82]. However, these methods usually have a high computational complexity regarding the estimation of the corresponding equalization coefficients, and for this reason, they are of limited interest for practical indoor VLC system implementation. Thus, an interesting point for future research would be to propose efficient non-linear equalization solutions of reasonable computational complexity.

Last but not least, due to the limitation of the available optical front-ends in the OCRG laboratory, we were not able to achieve high data-rates in Chapter 7 for a practical

VLC link and to verify the advantage of using CAP-FDE over DCO-OFDM for high data-rates. Moreover, the signal generation, synchronization and demodulation were processed off-line using a Matlab program. It would be interesting to implement a real-time VLC transmission set-up and to assert the suitability of CAP-FDE transmission under real conditions.

In addition to the above mentioned directions that are closely related to the subjects studied in this thesis, we can also mention some general and long-term considerations for VLC-based network deployment, such as addressing the problem of supporting multiple-users, mobility and dimming control; and investigating appropriate techniques for adapting CAP-FDE to such contexts.

APPENDIX

A Dimming control

Dimming control is a very important consideration in practical VLC systems since they should allow the user to dim arbitrarily the light source while maintaining the communication. Within its dynamic range, the brightness of an LED (*i.e.*, the output light intensity) is approximately proportional to its input current. Thus, a simple and intuitive method to provide dimming control is to adjust the analog DC-bias current continuously. This approach allows arbitrary dimming at the cost of a sophisticated intensity control circuitry. Moreover, large variations of the input current may result in undesired color shift of the LED. [90]. Another approach to achieve dimming control is to use pulse width modulation (PWM) [91–93]. The brightness of the LED can be controlled by varying the average duty cycle of the signal, where the modulated optical signal is only transmitted during the "on" period. This provides with easy adaptation to other pulse modulations with little additional cost, yet at the risk of significant drop of the transmission data rate. For example, the data rate is decreased 10 times when the average duty cycle of the PWM is reduced to 0.1, compared with the normal transmission scheme (*i.e.*, with duty cycle of 1). In the IEEE 802.15.7 standard, the IEEE VLC task group has proposed to use variable OOK (VOOK) and variable PPM (VPPM) schemes, which are variations of OOK and PPM to provide dimming control [7,94]. The dimming functionality of VOOK is achieved by redefining the duty cycle of the "on" and "off" symbols. This gives a constant bit rate as the light dims, but at the cost of reduced BER performance. VPPM is a combination of 2-PPM with PWM, where the pulse width of the each symbol is changed to meet the dimming demands. Similar to VOOK, the BER performance could be affected since the Euclidean distance of different symbols is decreased. Other dimming schemes for PAM and QAM modulation in VLC could be also found in [95,96] with different complexity and performance.

APPENDIX B

Pseudo-code of the iterative site-based method

Input: ε_n, ρ_{ε_n}, S, R, $k_{\max}$, N
Output: Channel impulse response $h(t, S, R)$

Initialization:
$h(t, S, R) \leftarrow h^{(0)}(t, S, R)$
for $n \leftarrow 1, N$ **do**
    Calculate and save the result $h^{(0)}(t, S, \varepsilon_n^r)$, $h^{(0)}(t, \varepsilon_n^s, R)$
end for
for $n \leftarrow 1, N$ **do**
    for $m \leftarrow 1, N$ and $m \neq n$ **do**
        Calculate and save the result $h^{(0)}(t, \varepsilon_m^s, \varepsilon_n^r)$
    end for
end for
Iterative procedure:
for $k \leftarrow 1, k_{\max}$ **do**
    $h^{(k)}(t, S, R) \leftarrow 0$, $h^{(k)}(t, S, \varepsilon_n^r) \leftarrow 0$
    for $n \leftarrow 1, N$ **do**
        $h^{(k)}(t, S, R) \leftarrow h^{(k)}(t, S, R) + h^{(k-1)}(t, S, \varepsilon_n^r) \otimes h^{(0)}(t, \varepsilon_n^s, R)$
        Save the result $h^{(k)}(t, S, R)$
        for $m \leftarrow 1, N$ and $m \neq n$ **do**
            $h^{(k)}(t, S, \varepsilon_n^r) \leftarrow h^{(k)}(t, S, \varepsilon_n^r) + h^{(k-1)}(t, S, \varepsilon_m^r) \otimes h^{(0)}(t, \varepsilon_m^s, \varepsilon_n^r)$
        end for
        Save the result $h^{(k)}(t, S, \varepsilon_n^r)$
    end for
    $h(t, S, R) \leftarrow h(t, S, R) + h^{(k)}(t, S, R)$
end for

APPENDIX C

Hermitian symmetry

The Hermitian symmetry is used to obtain a real-valued time-domain signal after IDFT. Given an OFDM system with N subcarriers, the Hermitian symmetry is defined as follows:

$$\begin{cases} X_0 & = X_{N/2} = 0 \\ X_k & = X^*_{N-k}, 0 < k < N/2 \end{cases} \tag{C.1}$$

where X^*_k is the complex conjugate of X_k. The time-domain signal $x(n)$ after IDFT can be expressed as:

$$\begin{aligned} x(n) &= \frac{1}{N}\sum_{k=0}^{N-1} X_k \exp\left(j2\pi kn/N\right) \\ &= \frac{1}{N}\sum_{k=1}^{N/2-1} X_k \exp\left(j2\pi kn/N\right) + \frac{1}{N}\sum_{N/2+1}^{N-1} X_k \exp\left(j2\pi kn/N\right) \\ &= \frac{1}{N}\sum_{k=1}^{N/2-1} \left(X_k \exp\left(j2\pi kn/N\right) + X^*_k \exp\left(j2\pi(n-k)n/N\right)\right) \\ &= \frac{1}{N}\sum_{k=1}^{N/2-1} \left(X_k \exp\left(j2\pi kn/N\right) + X^*_k \exp\left(-j2\pi kn/N\right)\right) \\ &= \frac{2}{N}\sum_{k=1}^{N/2-1} \left(\mathcal{R}e\left\{X_k\right\} \cos\left(\frac{2\pi kn}{N}\right) - \mathcal{I}m\left\{X_k\right\} \sin\left(\frac{2\pi kn}{N}\right)\right) \end{aligned} \tag{C.2}$$

where $\mathcal{R}e\left\{*\right\}$ and $\mathcal{I}m\left\{*\right\}$ are the real and imaginary part of a complex number, respectively. We can see the signal is real-valued if we impose the Hermitian symmetry constraint.

APPENDIX D

Adaptive loading for optical OFDM

Principles of adaptive loading

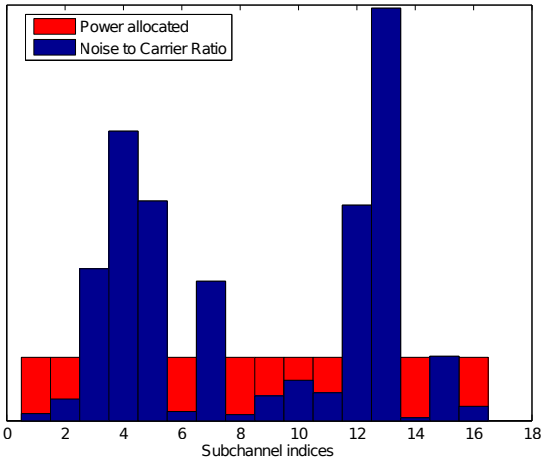

Figure D.1 — An example of power-loading using water-filling algorithm for a OFDM-based scheme with 16 sub-carriers

Adaptive loading can be used to further increase the data rate for OFDM-based schemes. We can adaptively assign different transmit powers (power-loading) or information bits (bit-loading) on different sub-carriers based on their channel condition. In this way, we avoid loading information on certain sub-bands that have a large noise level (*i.e.*, high attenuation), and load more information bits on sub-bands with high SNRs. As a result, the overall system capacity can be maximized compared to the regular OFDM schemes [97].

Let us look at the sub-channel on the k-th sub-carrier of an OFDM signal with a total number of N subcarriers. If N is large enough, the attenuation in the frequency domain

on each sub-carrier can be considered as constant. Then the corresponding received signal can be expressed as:

$$Y_k = H_k \cdot X_k + Z_k, \tag{D.1}$$

where H_k is the attenuation factor of the k-th sub-channel, and Z_k is the AWGN noise of zero mean and variance σ_Z^2. According to the Shannon-Hartley theorem, the channel capacity b_k (in bits) of this sub-channel is

$$b_k = \log_2\left(1 + \frac{H_k^2 P_{Xk}}{\sigma_{Zk}^2}\right) \tag{D.2}$$

where $P_{Xk} = \sigma_X^2$ is the allocated power to the k-th sub-carrier. Then, maximizing the total capacity $C^{(\text{tot})}$ turns to be a constrained optimisation problem as

$$\begin{aligned} C^{(\text{tot})} &= \underset{P_{Xk}}{\text{argmax}} \sum_{k=1}^{N} \log_2\left(1 + \frac{H_k^2 P_{Xk}}{\sigma_{Zk}^2}\right) \\ &\text{subject to} \sum_{k=1}^{N} P_{Xk} = P_X^{(\text{tot})} \end{aligned} \tag{D.3}$$

This problem can be solved by introducing the Lagrange method such that:

$$\begin{aligned} P_{Xk} &= \max\left(\lambda - \frac{\sigma_{Zk}^2}{H_k^2}, 0\right) \\ &\text{with } \lambda \text{ chosen such that} \sum_{k=1}^{N} P_{Xk} = P_X^{(\text{tot})}. \end{aligned} \tag{D.4}$$

Here, $P_X^{(\text{tot})}$ is the total available transmit power. This method is well-known as the water-filling algorithm. Figure D.1 illustrates an example of the water-filling algorithm for an OFDM system with 16 sub-carriers. As we can see and its name indicates, the signal power is *poured* onto the curve of noise-to-carrier ratio (NCR) (*i.e.*, the ratio of the noise power to the squared channel magnitude). We observe that no power is allocated to some of the sub-carrier due to their poor SNR (*i.e.*, high NCR).

By the water-filling algorithm, the obtained channel capacity b_k of each sub-carrier is in general a real number. However, obviously, only discrete rate distribution is realizable in a practical system (Note that some fractional rates are feasible by using channel coding). In addition, design of a coding scheme that reaches the channel capacity is usually a difficult task. Therefore, in practice, instead of maximizing the Shannon capacity in Equation (D.2), we maximize the data-rate b_k per sub-channel for a given symbol error rate SER P_s by introducing a "margin" as

$$b_k = \log_2\left(1 + \frac{1}{\Gamma}\text{SNR}_k\right) \tag{D.5}$$

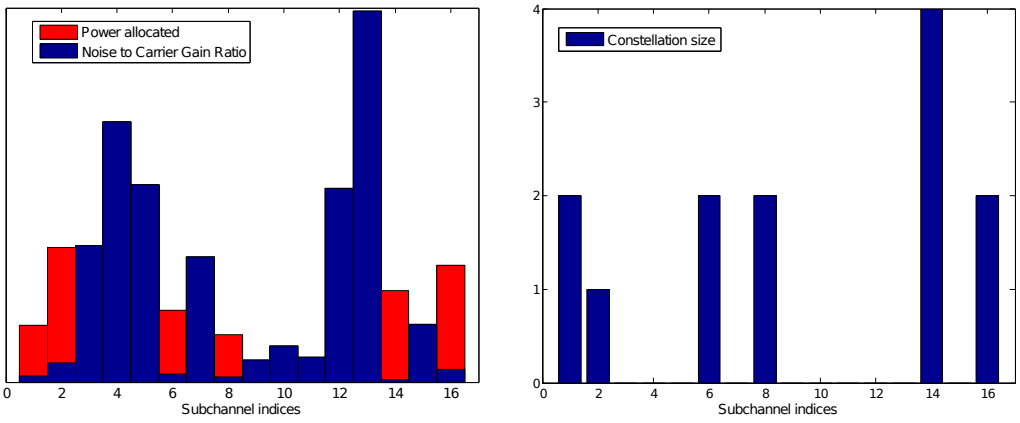

(a) (b)

Figure D.2 — An example of bit-power loading using the Levin-Campello algorithm for an OFDM-based system with 16 sub-carriers (a) power allocation (b) bit allocation

where Γ denotes the "**SNR gap**" and is chosen such as the uncoded transmission achieves the desired SER P_s, and $\mathrm{SNR}_k = H_k^2 P_{Xk}/\sigma_{Zk}^2$ is the SNR on the k-th sub-carrier.

To calculate the SNR gap Γ, let us consider the SER of M-QAM mapped symbols on the k-th sub-carrier, which can be approximately given by [46]:

$$P_s \leq 4\left(1-\frac{1}{\sqrt{M}}\right) Q\left(\sqrt{\frac{3}{M-1}\mathrm{SNR}_k}\right). \tag{D.6}$$

Ignoring the term $1-\frac{1}{\sqrt{M}}$ as it is almost equal to one for $\sqrt{M} \gg 1$, (D.6) can be further reformulated as:

$$b_k \cong \log_2\left(1+\frac{3}{\left(Q^{-1}(P_s/4)\right)^2}\mathrm{SNR}_k\right) \tag{D.7}$$

where $b_k = \log_2(M)$ is data-rate on the k-th sub-carrier. Therefore, the SNR gap Γ in (D.5) is given by

$$\Gamma \doteq \frac{1}{3}\left(Q^{-1}(P_s/4)\right)^2 \tag{D.8}$$

As a result, the optimisation problem in Equation (D.3) becomes

$$\begin{aligned} b^{(\mathrm{opt})} &= \underset{P_{Xk}}{\mathrm{argmax}} \sum_{k=1}^{N} b_k \\ \text{subject to} &\sum_{k=1}^{N} P_{Xk} = P_X^{(\mathrm{tot})} \end{aligned} \tag{D.9}$$

Note that the b_k in Equation (D.9) must be an integer for a practical system. As a result, the optimum solution to this problem may not be unique. One popular approach to this problem is the **Levin-Campello algorithm** whose details can be found in [26]. This algorithm starts by an initial bit distribution and converges fast to an optimal/sub-optimal bit loading scheme without violating the total power and minimal BER constraints. The resulting bit- and power-loading using the Levin-Campello algorithm for the same configuration in Figure D.1 is showed in Figure D.2.

Problem of integrating clipping noise with adaptive loading

For limiting the PAPR of OFDM-based schemes, the common approach is to use clipping as stated in Section 4.3.5. However, this results in difficulty in integrating with adaptive loading. In fact, if we take into account the clipping noise, Equation (D.1) should be rewritten as

$$Y_k = H_k \cdot (\alpha X_k + Z_c) + Z_k \tag{D.10}$$

where α is the attenuation caused by the clipping effect, and Z_c is the clipping noise of variance σ^2_{Zc} in frequency domain as described in Section 4.3.5. Accordingly, Equation (D.5) for bit-power loading becomes

$$b_k = \log_2\left(1 + \frac{1}{\Gamma}\frac{\alpha^2 H_k^2 P_{Xk}}{\sigma^2_{Zk} + \alpha^2\sigma^2_{Zc}}\right). \tag{D.11}$$

Note that the parameters α and σ^2_{Zc} in (D.11) are directly related to the bit or power distribution on each sub-carrier, which means that they are changing accordingly during the optimization process. Moreover, it is impossible to find an analytical expression that can determine α and σ^2_{Zc} for a given bit power distribution scheme. Therefore, we can no longer use the optimization problem described in Equation (D.9) to maximize the system capacity. Note that in the related works in the literatures, the clipping effect has been neglected when using bit-power loading, which is not correct in practice. That is why we didn't consider any bit-power loading scheme for DCO-OFDM in the simulation results in this thesis.

APPENDIX E

Derivation of the condition of zero interference for CAP

Let us expand the auto-correlations and cross-correlations in Equations (5.4) and (5.5) as follows:

$$\begin{aligned} h_{\mathrm{II}}(t) &= g(t)\cos(2\pi f_c t) \otimes f(t)\cos(2\pi f_c t) \\ h_{\mathrm{IQ}}(t) &= g(t)\cos(2\pi f_c t) \otimes f(t)\sin(2\pi f_c t) \\ h_{\mathrm{QI}}(t) &= g(t)\sin(2\pi f_c t) \otimes f(t)\cos(2\pi f_c t) \\ h_{\mathrm{QQ}}(t) &= g(t)\sin(2\pi f_c t) \otimes f(t)\sin(2\pi f_c t) \end{aligned} \tag{E.1}$$

where $f(t)$ and $g(t)$ are the baseband shaping filters, and f_c is the carrier frequency. Obviously, we have $h_{\mathrm{IQ}}(t) = h_{\mathrm{QI}}(t)$.

In fact, take a close look at the $h_{\mathrm{IQ}}(t)$, we can expand the convolution operation and rewrite it as

$$\begin{aligned} h_{\mathrm{IQ}}(t) &= \int_{\infty}^{\infty} g(\tau)\cos(2\pi f_c \tau)\cdot f(t-\tau)\sin\left(2\pi f_c(t-\tau)\right)d\tau \\ &= \frac{1}{2}\sin(2\pi f_c t)\cdot\int_{\infty}^{\infty} g(\tau)f(t-\tau)d\tau + \frac{1}{2}\int_{\infty}^{\infty} g(\tau)f(t-\tau)\sin\left(2\pi f_c(t-2\tau)\right)d\tau \\ &= \underbrace{\frac{1}{2}\sin(2\pi f_c t)\cdot h(t)}_{\text{First term}} + \underbrace{\frac{1}{2}\int_{\infty}^{\infty} g(\tau)f(t-\tau)\sin\left(2\pi f_c(t-2\tau)\right)d\tau}_{\text{Second term}} \end{aligned} \tag{E.2}$$

where $h(t) = g(t) \otimes f(t)$. Using the trigonometric identity, we have:

$$\sin(2\pi f_c(t-2\tau)) = \sin\left(2\pi f_c 2(t-\tau)\right)\cdot\cos(2\pi f_c t) - \cos\left(2\pi f_c 2(t-\tau)\right)\cdot\sin(2\pi f_c t).$$

Then, the second term in Equation (E.2) can be expanded as:

$$\frac{1}{2}\left\{\cos(2\pi f_c t)\cdot g(t)\otimes[f(t)\sin(2\pi 2 f_c t)] - \sin(2\pi f_c t)\cdot g(t)\otimes[f(t)\cos(2\pi 2 f_c t)]\right\}. \tag{E.3}$$

Note that the convolution in (E.3) can be viewed as filtering the signal $f(t)$ modulated around $2f_c$ by a low pass filter $g(t)$. In fact, by looking at Figure E.1, if we have

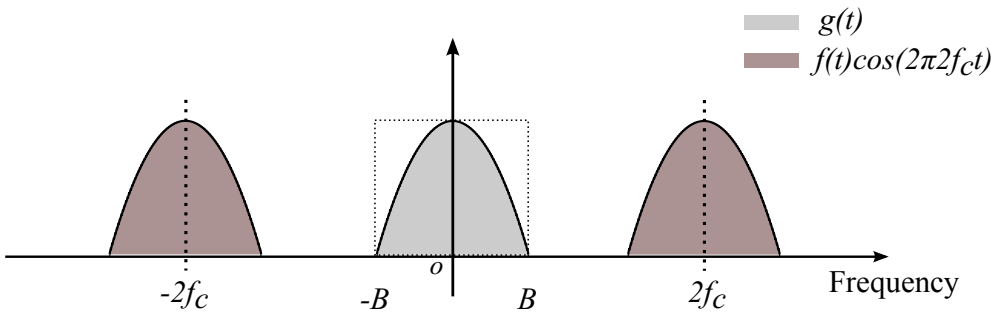

Figure E.1 — Illustration of the product of $g(t)$ and $f(t)\cos(2\pi f_c t)$ in frequency domain

$f_c \geq B$, the spectrum of $g(t)$ and $f(t)\cos(2\pi f_c t)$ (or $f(t)\sin(2\pi f_c t)$) does not intersect and their product becomes zero, which means that $g(t) \otimes [f(t)\cos(2\pi 2 f_c t)] = g(t) \otimes [f(t)\sin(2\pi 2 f_c t)] = 0$. As a result, we have:

$$h_{\mathrm{IQ}}(t) = \frac{1}{2}\sin(2\pi f_c t) \cdot h(t) \tag{E.4}$$

In a same manner, we have:

$$h_{\mathrm{II}}(t) = h_{\mathrm{QQ}}(t) = \cos(2\pi f_c t) \cdot h(t). \tag{E.5}$$

Regarding Equations (E.4) and (E.5), the condition of zero interference for CAP modulation is satisfied if $h(t)$ satisfies the Nyquist criterion and $f_c \geq B$.

APPENDIX F

Multi-CAP signal generation

Let us first remind the mathematical expression of the transmitted signal $x(t)$ for a conventional CAP scheme

$$\begin{aligned} x(t) &= \sum_{n=-\infty}^{\infty} I_n \cdot h_{\mathrm{I}}(t - nT_s) - Q_n \cdot h_{\mathrm{Q}}(t - nT_s) \\ &= \sum_{n=-\infty}^{\infty} I_n g(t - nT_s)\cos(2\pi f_c(t - nT_s)) - Q_n g(t - nT_s)\sin(2\pi f_c(t - nT_s)) \\ &= \sum_{n=-\infty}^{\infty} \mathcal{R}e\{X_n s(t - nT_s)\} \end{aligned} \tag{F.1}$$

where $X_n = I_n + jQ_n$ is the n-th symbol after QAM mapping, $g(t)$ is the baseband pulse shaping filter, T_s is the symbol duration, f_c is the carrier frequency and $s(t) = g(t)e^{j2\pi f_c t}$.

The transmitted signal of the N sub-band multi-CAP transmission scheme can be therefore written as

$$x(t) = \sum_{n=-\infty}^{\infty} \sum_{k=0}^{N-1} \mathcal{R}e\{X_n[k] s_k(t - nT_s)\} \tag{F.2}$$

where $s_k(t) = g(t)e^{j2\pi f_k t}$, f_k is the centre carrier frequency of the k-th sub-band, $X_n[k]$ is the complex symbol on the k-th sub-band at the time instant $t = nT_s$.

If the centre frequency of each sub-band f_k is chosen as

$$f_k = \frac{k}{T_s}, k = 0, \ldots, N-1 \tag{F.3}$$

and we consider an up-sampling factor of N (which means that we have a sampling rate of N/T_s, or a sampling interval of $\Delta t = T_s/N$), then, the m-th samples $x[m] =$

$x(m\Delta t), 0 \leq m \leq N$ can be written as:

$$
\begin{aligned}
x[m] &= \sum_{n=-\infty}^{\infty} \sum_{k=0}^{N-1} \underbrace{\mathcal{R}e\{X_n[k] s_k(m\Delta t - nT_s)\}}_{s(t)=g(t)e^{j2\pi f_k t}} \\
&= \sum_{n=-\infty}^{\infty} g(m\Delta t - nT_s) \sum_{k=0}^{N-1} \underbrace{\mathcal{R}e\{X_n[k] e^{j2\pi f_k (m\Delta t - nT_s)}\}}_{f_k = k/T_s} \\
&= \sum_{n=-\infty}^{\infty} \underbrace{g(m\Delta t - nT_s) \sum_{k=0}^{N-1} \mathcal{R}e\{X_n[k] e^{j2\pi \frac{k}{T_s}(m\Delta t - nT_s)}\}}_{\Delta t = T_s/N} \\
&= \sum_{n=-\infty}^{\infty} \underbrace{g([m-nN]\Delta t)}_{g[m]=g(m\Delta t)} \sum_{k=0}^{N-1} \mathcal{R}e\{\underbrace{X_n[k] e^{j2\pi \frac{km}{N}}}_{\text{Inverse FFT}}\} \\
&= \sum_{n=-\infty}^{\infty} g[m-nN] \cdot \mathcal{R}e\{\text{IFFT}\{X_n\}[m]\} \\
&= \{g[n] \otimes \mathcal{R}e\{\text{IFFT}\{X_n\}\}\}[m].
\end{aligned}
\tag{F.4}
$$

From (F.4), we can see the digitalized multi-CAP signal $x[m]$ can be realized using the convolution of the baseband digital shaping filter $g[n]$ and the real part of the IFFT of the sequence X_n. As a result, this approach could greatly simplify the signal generation for a N sub-band multi-CAP transmission, compared to the way of using $2N$ pulse shaping filters proposed in [73].

List of Figures

List of Tables

Bibliography

[1] CISCO, "Global Mobile Data Traffic Forecast Update 2015-2020," http://www.cisco.com/c/en/us/solutions/collateral/service-provider/visual-networking-index-vni/mobile-white-paper-c11-520862.html, 2015.

[2] W. Shieh and I. Djordjevic, *OFDM for Optical Communication*, Academic Press, Elsevier, 1st edition, 2009.

[3] F. Xu, *Dévelopment des méthodes de transmission pour un système de télécommunication optique aérienne à haut débit*, Ph.D. thesis, Aix-Marseille University, Oct. 2010.

[4] Y. Tanaka, T. Komine, S. Haruyama, and M. Nakagawa, "Indoor visible light data transmission system utilizing white LED lights," *IEICE transactions on communications*, vol. 86, no. 8, pp. 2440–2454, Aug. 2003.

[5] M. Nakagawa, "Visible Light Communications Consortium (VLCC)," retrieved May 2016 from http://www.vlcc.net.

[6] OMEGA, "European Home Gigabit Acess project," retrieved May 2016 from http://www.ict-omega.eu.

[7] Institute of Electrical and Electronics Engineers (IEEE), *IEEE Standard for Local and Metropolitan Area Networks-part 15.7: Short-Range Wireless Optical Communication Using Visible Light*, Sept. 2011.

[8] Fraunhofer Institut, "Visible light communication system up to 1 Gbit/s," retrieved May 2016 from http://www.hhi.fraunhofer.de/departments/photonic-networks-and-systems/products-and-services/vlc-system-1-gbits.html.

[9] pureLiFi, "The fastest, mallest and most secure LiFi system," retrieved May 2016 from http://purelifi.com/lifi-products/lifi-x/.

[10] S. Arnon, *Visible Light Communication*, Cambriage University Press, 1st edition, 2015.

[11] A. Jovicic, J. Li, and T. Richardson, "Visible light communication: Opportunities, challenges and the path to market," *IEEE Communications Magazine*, vol. 51, no. 12, pp. 26–32, Dec. 2013.

[12] H. Burchardt, N. Serafimovski, D. Tsonev, S. Videv, and H. Haas, "VLC: Beyond point-to-point communication," *IEEE Communications Magazine*, vol. 52, no. 7, pp. 98–105, Jul. 2014.

[13] E. F. Schubert, *Light Emitting Diodes*, Cambriage Univ. Press, 2nd edition, 2006.

[14] G. Cossu, A. M. Khalid, P. Choudhury, R. Corsini, and E. Ciaramella, "3.4 Gbit/s visible optical wireless transmission based on RGB LED," *Optics Express*, vol. 20, no. 26, pp. B501–B506, Dec. 2012.

[15] C. Kottke, J. Hilt, K. Habel, J. Vuêić, and K. D. Langer, "1.25 Gbit/s visible light WDM link based on DMT modulation of a single RGB LED luminary," in *European Conference and Exhibition on Optical Communication*, Sept. 2012, Amsterdam, Netherlands.

[16] Y. Wang, Y. Wang, N. Chi, J. Yu, and H. Shang, "Demonstration of 575-Mb/s downlink and 225-Mb/s uplink bi-directional SCM-WDM visible light communication using RGB LED and phosphor-based LED," *Optics express*, vol. 21, no. 1, pp. 1203–1208, 2013.

[17] J. Grubor, S. Randel, K.-D. Langer, and J.W. Walewski, "Broadband information broadcasting using LED-based interior lighting," *Journal of Lightwave Technology*, vol. 26, no. 24, pp. 3883–3892, 2008.

[18] T. Komine and M. Nakagawa, "Fundamental analysis for visible-light communication system using LED lights," *IEEE Transactions on Consumer Electronics*, vol. 50, no. 1, pp. 100–107, 2004.

[19] J. Y. Sung, C. W. Chow, and C. H. Yeh, "Is blue optical filter necessary in high speed phosphor-based white light LED visible light communications?," *Optics Express*, vol. 22, no. 17, pp. 20646–20651, Aug. 2014.

[20] L. Zeng, D. O'Brien, H. Le-Minh, K. Lee, D. Jung, and Y. Oh, "Improvement of date rate by using equalization in an indoor visible light communication system," in *4th IEEE International Conference on Circuits and Systems for Communications*, May 2008, pp. 678–682, Shanghai, China.

[21] H. Le-Minh, D. O'Brien, G. Faulkner, L. Zeng, K. Lee, D. Jung, Y. Oh, and E. T. Won, "100-Mb/s NRZ visible light communications using a postequalized white LED," *IEEE Photonics Technology Letters*, vol. 21, no. 15, pp. 1063–1065, Aug. 2009.

[22] S. Zhang, S. Watson, J. D. McKendry, D. Massoubre, A. Cogman, E. Gu, R.K. Henderson, A.E. Kelly, and M.D. Dawson, "1.5 Gbit/s multi-channel visible light communications using CMOS-controlled GaN-based LEDs," *Journal of Lightwave Technology*, vol. 31, no. 8, pp. 1211–1216, Apr. 2013.

[23] D. Tsonev, H. Chun, S. Rajbhandari, J.J.D McKendryand S. Videv, E. Gu, M. Haji, S. Watson, A.E. Kelly, G. Faulkner, and et al., "A 3-Gb/s single-LED OFDM-based wireless VLC link using a gallium nitride μLED," *IEEE Photonics Technology Letters*, vol. 36, pp. 637–640, Apr. 2014.

[24] P. A. Haigh, Z. Ghassemlooy, S. Rajbhandari, and I. Papakonstantinou, "Visible light communications using organic light emitting diodes," *IEEE Communications Magazine*, vol. 51, no. 8, pp. 148–154, Aug. 2013.

[25] T. Kamalakis, J. W. Walewski, G. Ntogari, and G. Mileounis, "Empirical volterra-series modeling of commercial light-emitting diodes," *Journal of Lightwave Technology*, vol. 29, no. 14, pp. 2146–2155, Jul. 2011.

[26] H. Elgala, *A Study on the Impact of Nonlinear Characteristics of LEDs on Optical OFDM*, Ph.D. thesis, School of Engineering and Science, Jacobs University, Mar. 2010.

[27] S. Dimitrov, S. Sinanovic, and H. Haas, "Clipping noise in OFDM-based optical wireless communication systems," *IEEE Transactions on Communications*, vol. 60, no. 4, pp. 1072–1081, Apr. 2012.

[28] S. Dimitrov and H. Haas, "On the clipping noise in an aco-ofdm optical wireless communication system," in *IEEE Global Telecommunications Conference (GLOBECOM 2010)*, Dec. 2010, pp. 1–5.

[29] J. M. Kahn and J. R. Barry, "Wireless infrared communications," *Proceedings of the IEEE*, vol. 85, no. 2, pp. 265–298, Feb. 1997.

[30] J. Grubor, S. Randel, K. D. Langer, and J. W. Walewski, "Bandwidth-efficient indoor optical wireless communications with white light-emitting diodes," in *6th International Symposium on Communication Systems, Networks and Digital Signal Processing (CNSDSP)*, Jul. 2008, pp. 165–169, Graz, Austria.

[31] S. Hranilovic, *Wireless Optical Communication System*, Springer, 1st edition, 1996.

[32] Z. Ghassemlooy, W. Popoola, and S. Rajbhandari, *Optical Wireless Communications: System and Channel Modelling with* MATLAB, CRC Press, Boca Raton, FL, 1st edition, 2013.

[33] H. Hashemi, G. Yun, M. Kavehrad, and F. Behbahani, "Frequency response measurements of the wireless indoor channel at infrared frequencies," in *IEEE International Conference on Communications (ICC)*, May 1994, pp. 1511–1515, New Orleans, LA.

[34] J. M. Kahn, W. J. Krause, and J. B. Carruthers, "Experimental characterization of non-directed indoor infrared channels," *IEEE Transactions on Communications*, vol. 43, no. 2/3/4, pp. 1613–1623, Feb. 1995.

[35] J. B. Carruthers and J. M. Kahn, "Modeling of non-directed wireless infrared channels," *IEEE Transactions on Communications*, vol. 45, no. 10, pp. 1260–1268, Oct. 1995.

[36] F. J. Lopez-Hernandez, R. Perez-Jimenez, and A. Santamaria, "Ray-tracing algorithms for fast calculation of the channel impulse response on diffuse IR wireless indoor channels," *Optical Engineering*, vol. 39, no. 10, pp. 2775–2780, Oct. 2000.

[37] E. Sarbazi, M. Uysal, M. Abdallah, and K. Qaraqe, "Ray tracing based channel modeling for visible light communications," in *Signal Processing and Communications Applications Conference (SIU)*, Apr. 2014, pp. 702–705, Trabzon, Turkey.

[38] S. P. Rodríguez, R. P. Jiménez, and B. R. Mendoza, "Simulation of impulse response for indoor visible light communications using 3D CAD models," *EURASIP Journal on Wireless Communications and Networking*, vol. 2013, no. 1, pp. 1–10, Jan. 2013.

[39] J. R. Barry, J. M. Kahn, W. J. Krause, E. A. Lee, and D. G. Messerschmitt, "Simulation of multipath impulse response for indoor wireless optical channels," *IEEE*

Journal on Selected Areas in Communications, vol. 11, no. 3, pp. 367–379, Apr. 1993.

[40] D. Mavrakis and S. R. Saunders, "A novel modeling approach for wireless infrared links," in *International symposium wireless personal multimedia communcation (WPCS)*, Nov. 2000, pp. 609–614, Bangkok, Thailand.

[41] J. B. Carruthers and P. Kannan, "Iterative site-based modeling for wireless infrared channels," *IEEE Transactions on Antennas and Propagation*, vol. 50, no. 5, pp. 759–765, May 2002.

[42] T. Komine and M. Nakagawa, "Fundamental analysis for visible-light communication system using LED lightings," *IEEE Transactions on Consumer Electronics*, vol. 50, no. 1, pp. 100–107, Feb. 2004.

[43] S. D. Personick, "Receiver design for optical fiber systems," *Proceedings of the IEEE*, vol. 65, no. 12, pp. 1670–1678, Dec. 1977.

[44] K. Lee, H. Park, and J. R. Barry, "Indoor channel characteristics for visible light communications," *IEEE Communications Letters*, vol. 15, no. 2, pp. 217–219, Feb. 2011.

[45] M. Wolf, L. Grobe, M.R. Rieche, A. Koher, and J. Vucic, "Block transmission with linear frequency domain equalization for dispersive optical channels with direct detection," in *12-th International Conference on Transparent Optical Networks (ICTON)*, Jun. 2010, pp. 1–8, Munich, Germany.

[46] J. G. Proakis and M. Salehi, *Digital Communication*, McGraw-Hill Higher Education, New York, 5th edition, 2007.

[47] I. Kalet, "The multitone channel," *IEEE Transactions on Communications*, vol. 37, no. 2, pp. 119–124, Feb. 1989.

[48] J. A. C. Bingham, "Multicarrier modulation for data transmission: an idea whose time has come," *IEEE Communications Magazine*, vol. 28, no. 5, pp. 5–14, May 1990.

[49] J. Vučić, C. Kottke, S. Nerreter, K. D. Langer, and J. W. Walewski, "513 Mbit/s visible light communications link based on DMT-modulation of a white LED," *Journal of Lightwave Technology*, vol. 28, no. 24, pp. 3512–3518, Dec. 2010.

[50] A. M. Khalid, G. Cossu, R. Corsini, P. Choudhury, and E. Ciaramella, "1-Gb/s transmission over a phosphorescent white LED by using rate-adaptive discrete multitone modulation," *IEEE Photonics Journal*, vol. 4, no. 5, pp. 1465–1473, Oct. 2012.

[51] J. Armstrong and A.J. Lowery, "Power efficient optical OFDM," *Electronics Letters*, vol. 42, no. 6, pp. 370–372, Mar. 2006.

[52] J. Armstrong and B. J. C. Schmidt, "Comparison of asymmetrically clipped optical OFDM and DC-biased optical OFDM in AWGN," *IEEE Communications Letters*, vol. 12, no. 5, pp. 343–345, May 2008.

[53] P. Saengudomlert, "On the benefits of pre-equalization for ACO-OFDM and Flip-OFDM indoor wireless optical transmissions over dispersive channels," *Journal of Lightwave Technology*, vol. 32, no. 1, pp. 70–80, Jan. 2014.

[54] S. C. J. Lee, S. Randel, F. Breyer, et al., "PAM-DMT for intensity-modulated and direct-detection optical communication systems," *IEEE Photonics Technology Letters*, vol. 21, no. 23, pp. 1749–1751, Dec. 2009.

[55] M. S. Islim, D. Tsonev, and H. Haas, "Spectrally enhanced PAM-DMT for IM/DD optical wireless communications," in *IEEE 26th Annual International Symposium on Personal, Indoor, and Mobile Radio Communications (PIMRC)*, Aug. 2015, pp. 877–882, Hong Kong.

[56] D. Dardari, V. Tralli, and A. Vaccari, "A theoretical characterization of nonlinear distortion effects in OFDM systems," *IEEE Transactions on Communications*, vol. 48, no. 10, pp. 1755–1764, Oct. 2000.

[57] J. J. Bussgang, "Cross correlation functions of amplitude-distorted Gaussian signals," Tech. Rep. 216, Research Laboratory of Electronics, Massachusetts Institute of Technology, Cambriage, MA, USA, Mar. 1952.

[58] D. Tsonev, S. Sinanovic, and H. Haas, "Complete modeling of nonlinear distortion in OFDM-based optical wireless communication," *Journal of Lightwave Technology*, vol. 31, no. 18, pp. 3064–3076, Sept. 2013.

[59] I. Neokosmidis, T. Kamalakis, J.W. Walewski, B. Inan, and T. Sphicopoulos, "Impact of nonlinear LED transfer function on discrete multitone modulation: Analytical approach," *Journal of Lightwave Technology*, vol. 27, no. 22, pp. 4970–4978, Nov. 2009.

[60] T. Pollet, M. Van Bladel, and M. Moeneclaey, "Ber sensitivity of ofdm systems to carrier frequency offset and wiener phase noise," *IEEE Transactions on Communications*, vol. 43, no. 2/3/4, pp. 191–193, Feb. 1995.

[61] H. Sari, G. Karam, and I. Jeanclaud, "Frequency-domain equalization of mobile radio and terrestrial broadcast channels," in *IEEE Global Telecommunications Conference (GLOBECOM '94)*, Nov. 1994, vol. 1, pp. 1–5, San Francisco, CA.

[62] H. Sari, G. Karam, and I. Jeanclaud, "Transmission techniques for digital terrestrial tv broadcasting," *IEEE Communications Magazine*, vol. 33, no. 2, pp. 100–109, Feb. 1995.

[63] D. Falconer, S. L. Ariyavisitakul, A. Benyamin-Seeyar, and B. Eidson, "Frequency domain equalization for single-carrier broadband wireless systems," *IEEE Communications Magazine*, vol. 40, no. 4, pp. 58–66, Apr. 2002.

[64] K. Ishihara, T. Kobayashi, R. Kudo, Y. Takatori, A. Sano, E. Yamada, H. Masuda, and Y. Miyamoto, "Frequency-domain equalisation for optical transmission systems," *Electronics Letters*, vol. 44, no. 14, pp. 870–871, Jul. 2008.

[65] K. Acolatse, Y. Bar-Ness, and S.K. Wilson, "Novel techniques of single-carrier frequency-domain equalization for optical wireless communications," *EURASIP Journal on Advances in Signal Processing*, vol. 2011, pp. 1–13, Jan. 2011.

[66] M. Wolf and M. Haardt, "Comparison of OFDM and frequency domain equalization for dispersive optical channels with direct detection," in *14-th International Conference on Transparent optical Networks (ICTON)*, 2012, pp. 1–7, Coventry, UK.

[67] M. Wolf, S. A. Cheema, M. Haardt, and L. Grobe, "On the performance of block transmission schemes in optical channels with a Gaussian profile," in *16-th International Conference on Transparent Optical Networks (ICTON)*, Jul. 2014, pp. 1–8, Graz, Austria.

[68] L. Grobe and K. D. Langer, "Block-based PAM with frequency domain equalization in visible light communications," in *IEEE Globecom Workshops*, Dec. 2013, pp. 1070–1075, Atlanta, GA.

[69] Y. Wang, R. Li, Y. Wang, and Z. Zhang, "3.25-Gbps visible light communication system based on single carrier frequency domain equalization utilizing an RGB LED,"

in *Optical Fiber Communications Conference and Exhibition (OFC)*, Mar. 2014, pp. 1–3, San Francisco, CA.

[70] W. Henkel, T. Kessler, and H.Y. Chung, "Coded 64-CAP ADSL in an impulse-noise environment-modeling of impulse noise and first simulation results," *IEEE Journal on Selected Areas in Communications*, vol. 13, no. 9, pp. 1611–1621, Dec. 1995.

[71] F.M. Wu, C.T. Lin, C.C. Wei, C.W. Chen, Z.Y. Chen, and H.T. Huang, "Performance comparison of OFDM signal and CAP signal over high capacity RGB-LED-based WDM visible light communication," *IEEE Photonics Journal*, vol. 4, no. 4, Aug. 2013.

[72] G. Stepniak, J. Siuzdak, and P. Zwierko, "Compensation of a VLC phosphorescent white LED nonlinearity by means of volterra DFE," *IEEE Photonics Technology Letters*, vol. 25, no. 16, pp. 1597–1600, Aug. 2013.

[73] P. A. Haigh, S. T. Le, S. Zvanovec, and Z. Ghassemlooy *et al.*, "Multi-band carrier-less amplitude and phase modulation for bandlimited visible light communications systems," *IEEE Wireless Communications*, vol. 22, no. 2, pp. 46–53, Apr. 2015.

[74] P. A. Haigh, P. Chvojka, S. Zvanovec, Z. Ghassemlooy, and S. T. Le *et al.*, "Experimental verification of visible light communications based on multi-band CAP modulation," in *Optical Fiber Communication Conference (OFC)*, Mar. 2015.

[75] F.M. Wu, C.T. Lin, C.C. Wei, C.W. Chen, H.T. Huang, and C.H. Ho, "1.1-Gb/s white-LED-based visible light communication employing carrier-less amplitude and phase modulation," *IEEE Photonics Technology Letters*, vol. 24, no. 19, pp. 1730–1732, Oct. 2012.

[76] M. S. Erkilin, Z. Li, S. Pachnicke, H. Griesser, B. C. Thomsen, P. Bayvel, and R. I. Killey, "Spectrally efficient WDM Nyquist Pulse-shaped 16-QAM subcarrier modulation transmission with direct detection," *Journal of Lightwave Technology*, vol. 33, no. 15, pp. 3147–3155, Aug. 2015.

[77] G. H. Im, D. B. Harman, G. Huang, A. V. Mandzik, M. H. Nguyen, and J. J. Werner, "51.84 Mb/s 16-CAP ATM LAN standard," *IEEE Journal on Selected Areas in Communications*, vol. 13, no. 4, pp. 620–632, May 1995.

[78] T. Li, J. Yu, J. Liu, A.P.T. Lau, N. Chi, and C. Lu, "Advanced modulation formats for short reach optical communication systems," *IEEE Network*, vol. 27, no. 6, pp. 6–13, Nov. 2013.

[79] P. A. Haigh, A. Burton, K. Werfli, H. L. Minh, E. Bentley, P. Chvojka, W. O. Popoola, I. Papakonstantinou, and S. Zvanovec, "A multi-CAP visible-light communications system with 4.85-b/s/Hz spectral efficiency," *IEEE Journal on Selected Areas in Communications*, vol. 33, no. 9, pp. 1771–1779, Sept. 2015.

[80] B. Inan, S. C. J. Lee, S. Randel, I. Neokosmidis, A.M. Koonen, and J.W. Walewski, "Impact of LED nonlinearity on discrete multitone modulation," *Journal of Optical Communications and Networking*, vol. 1, no. 5, pp. 439, Oct. 2009.

[81] M. Schetzen, "Nonlinear system modeling based on the wiener theory," *Proceedings of the IEEE*, vol. 69, no. 12, pp. 1557–1573, Dec. 1981.

[82] Y. Wang, T. Li, X. Huang, J. Shi, and N. Chi, "Enhanced performance of a high-speed WDM CAP64 VLC system employing volterra series-based nonlinear equalizer," *IEEE Photonics Journal*, vol. 7, no. 3, pp. 1–7, Jun. 2015.

[83] X. Hong, S. Chen, Y. Gong, and C. J. Harris, "Nonlinear equalization of hammerstein OFDM systems," *IEEE Transactions on Signal Processing*, vol. 62, no. 21, pp. 5629–5639, Nov. 2014.

[84] J. Kim and K. Konstantinou, "Digital predistortion of wideband signals based on power amplifier model with memory," *Electronics Letters*, vol. 37, no. 23, pp. 1417–1418, Nov. 2001.

[85] H. Qian, S. J. Yao, S. Z. Cai, and T. Zhou, "Adaptive postdistortion for nonlinear leds in visible light communications," *Photonics Journal, IEEE*, vol. 6, no. 4, pp. 1–8, Aug. 2014.

[86] L. Peng, S. Haese, and M. Helard, "Frequency domain LED compensation for nonlinearity mitigation in DMT systems," *Photonics Technology Letters, IEEE*, vol. 25, no. 20, pp. 2022–2025, Oct. 2013.

[87] R. Mesleh, H. Elgala, and H. Haas, "LED nonlinearity mitigation techniques in optical wireless OFDM communication systems," *Journal of Optical Communications and Networking*, vol. 4, no. 11, pp. 865–875, Nov. 2012.

[88] J. Li, Z. Huang, X. Liu, and Y. Ji, "Hybrid time-frequency domain equalization for LED nonlinearity mitigation in OFDM-based VLC systems," *Optics Express*, vol. 23, no. 1, pp. 611–619, Jan. 2015.

[89] D. Bykhovsky and S. Arnon, "An experimental comparison of different bit-and-power-allocation algorithms for DCO-OFDM," *Journal of Lightwave Technology*, vol. 32, no. 8, pp. 1559–1564, Apr. 2014.

[90] K. Lee and P. Hyuncheol, "Modulations for visible light communications with dimming control," *IEEE Photonics Technology Letters*, vol. 23, no. 16, pp. 1136–1138, 2011.

[91] J. h. Choi, E. b. Cho, T. G. Kang, and C. G. Lee, "Pulse width modulation based signal format for visible light communications," in *OECC 2010 Technical Digest*, Jul. 2010, pp. 276–277.

[92] H.J. Jang, J. H. Choi, Z. Ghassemlooy, and C. G. Lee, "PWM-based PPM format for dimming control in visible light communication system," in *8th International Symposium on Communication Systems, Networks Digital Signal Processing (CSNDSP)*, Jul. 2012, pp. 1–5, Poznan, Poland.

[93] Z. Wang, W. D. Zhong, C. Yu, J. Chen, C. Francois, S. Po, and W. Chen, "Performance of dimming control scheme in visible light communication system," *Optics express*, vol. 20, no. 17, pp. 18861–18868, 2012.

[94] S. Rajagopal, R. D. Roberts, and S.K. Lim, "IEEE 802.15.7 visible light communication: modulation schemes and dimming support," *IEEE Communications Magazine*, vol. 50, no. 3, pp. 72–82, Mar. 2012.

[95] S. H. Lee, K. I Ahn, and J. K. Kwon, "Multilevel transmission in dimmable visible light communication systems," *Journal of Lightwave Technology*, vol. 31, no. 20, pp. 3267–3276, Oct. 2013.

[96] J. Y. Sung, C. W. Chow, and C. H. Yeh, "Dimming-discrete-multi-tone (DMT) for simultaneous color control and high speed visible light communication," *Optics Express*, vol. 22, no. 7, pp. 7538–7544, Apr. 2014.

[97] S. B. Weinstein, "The history of orthogonal frequency-division multiplexing," *IEEE Communications Magazine*, vol. 47, no. 11, pp. 26–35, Nov. 2009.